Electronic Thesis and Dissertation Repository

6-12-2020 4:00 PM

Identification of Aerodynamic Damping for Flexible Structures using Wind-induced Response

Shea Laventure, *The University of Western Ontario*

Supervisor: Sadhu, Ayan, *The University of Western Ontario*
Co-Supervisor: Bitsuamlak, Girma T., *The University of Western Ontario*
A thesis submitted in partial fulfillment of the requirements for the Master of Engineering
Science degree in Civil and Environmental Engineering
© Shea Laventure 2020

Follow this and additional works at: https://ir.lib.uwo.ca/etd

Part of the Structural Engineering Commons

Abstract

Damping estimation is a critical task to perform during the design of slender structures, or for existing structures. This is to ensure the response of the structure is within allowable limits and to determine if additional damping is necessary from auxiliary devices. If a slender structure is experiencing wind loading, a phenomenon known as aerodynamic damping arises, which has the potential to reduce the damping of the structure. The most efficient method to estimate aerodynamic damping is to use a system identification technique, which requires only the input forces and output response of the structure. This thesis describes how to estimate aerodynamic damping ratios of concrete chimneys using a sophisticated output-only system identification technique known as Second-Order Blind Identification. Wind fields generated using drag and lift coefficients and computational fluid dynamics (CFD) are applied to a finite-element concrete chimney model in both along-wind and across-wind directions. The time-series of the wind field is simulated using the power law for the mean wind speed and the von Karman spectrum for the turbulence. Total damping estimates are acquired at various wind speeds and modes in both directions, which are compared to the theoretical values. Aerodynamic damping is acquired by subtracting the structural damping, found using a free vibration test, from the total damping estimate. The aerodynamic damping estimates using drag and lift coefficients are compared with the CFD estimates. It is found that aerodynamic damping in the along-wind direction is always larger compared to the across-wind direction. Also, damping estimates using CFD often exhibit higher values than the wind field simulated using drag and lift coefficients. A general discussion on the results, research contributions, and future work for further research is provided.

Keywords

Summary for Lay Audience

Structures are affected by natural wind, especially when the wind takes on more chaotic forms such as storms, tornados, and hurricanes. Tall and slender structures are more vulnerable to wind as they exhibit higher deflections and less resistance to motion. The resistance to motion is a critical component when designing a slender structure or when analyzing the performance of an existing structure. Structural parameters such as mass and stiffness determine the resistance of motion, which is easily implemented during the design of a structure. However, this is not usually the case for existing structures, where mass and stiffness may not be known. Therefore, the statistics of a structure's motion during wind loading can be used to build a mathematical model of its vibration patterns. These vibration patterns contain information about the structure such as the rate at which its motion decreases. A state-of-the-art statistical method is explored in this thesis to analyze the vibration patterns of a slender chimney model and determine the rate at which its motion decreases. The chimney model is subjected to different types of wind loading to examine the effects of wind actions on structures and demonstrate the robustness of the proposed statistical method. The statistical method is efficient at identifying the motion of the chimney model, meaning there is confidence in implementing the method with structural design and monitoring of existing structures.

Acknowledgements

I would first like to express my sincere gratitude to my supervisors, Dr. Ayan Sadhu and Dr. Girma Bitsuamlak. I first met Dr. Sadhu while I was taking my undergraduate studies at Lakehead University and it was his professionalism, knowledge, and patience that led me to pursue a graduate degree under his supervision. His advice guided me to become a better student and I am confident this will help me achieve the next step in my career. I am also very pleased that I decided to collaborate my research efforts with Dr. Bitsuamlak. Before I started at Western University, I knew very little about wind engineering, and yet he helped me understand the many details related to my research. I could not be more impressed with Dr. Bitsuamlak's knowledge and patience while I was working with him and I will remain forever grateful.

I would also like to thank my fellow students and friends for helping me through this journey. To my office mates Sandeep, Premjeet, Kyle, and Mohamed, your presence was a welcomed sight in the office and I appreciate the occasional advice you gave me. I would like to send a special thank you to my fellow student and friend Kenny for his invaluable expertise and help related to the wind engineering aspects of my research.

I would like to show my sincere appreciation and gratitude for my family who has supported me and helped me achieve my goals. Thank you to my parents Larry and Brenda, and my sister Kelsey, for the endless support, phone calls, and occasional visits to London. None of my past, current, or future success is possible without your encouragement and I remain forever indebted.

Finally, I would like to thank the great and legendary Rick McGhie for providing me the highlight of the week every Wednesday night.

Table of Contents

List of Figures

List of Tables

Nomenclature

$\mathbf{A}$	Mixing matrix
$\overline{\mathbf{A}}$	State matrix
$\overline{\mathbf{B}}$	Input influence matrix
b	Width of building [m]
$\mathbf{C}$	Damping matrix [N s m^{-1}]
C_D	Drag coefficient
C_{Fx}	Force coefficient in along-wind direction
C_{Fy}	Force coefficient in across-wind direction
C_L	Lift coefficient
$C_{y,z}$	Decay coefficients
$\overline{\mathbf{C}}$	Observation matrix
$\mathbf{D}$	Eigenvalue matrix
d	Depth of building [m]
df	Frequency range increment
F_x	Force in the along-wind direction [N]
F_y	Force in the across-wind direction [N]
f	Frequency [Hz]
f_c	Coherence function
H	Complex conjugate transpose of matrix
h	Height of building [m]
$\mathbf{I}$	Identity matrix
$\mathbf{K}$	Stiffness matrix [N/m]

L_u	Turbulent length scale in along-wind direction
L_v	Turbulent length scale in across-wind direction
$\mathbf{M}$	Mass matrix [kg]
$\boldsymbol{n}(t)$	Noise vector
$q(t)$	Modal response
$\mathbf{R}_x(t)$	Covariance matrix
$R_x(\tau)$	Autocorrelation function
$\mathbf{S}$	Spectral matrix
S_u	Turbulence spectrum in along-wind direction
S_v	Turbulence spectrum in across-wind direction
$s(t)$	Source signal
t	Time [s]
$\mathbf{U}$	Unitary transformation matrix
$\overline{U}$	Mean wind speed [m/s]
U_{ref}	Reference wind speed for power law [m/s]
U_H^*	Reduced wind velocity
$\boldsymbol{u}$	State-space model input
u'	Wind fluctuation in along-wind direction
$\mathbf{V}$	Eigenvector matrix
v'	Wind fluctuation in across-wind direction
$\mathbf{W}$	Whitening matrix
$\boldsymbol{x}(t)$	Mixed signal with noise
$\boldsymbol{y}(t)$	Mixed signal
z	Height above ground [m]
z_{ref}	Reference height for power law [m]

α	Power-law exponent
$\boldsymbol{\Phi}$	Mode shape matrix
ϕ	Phase angle
τ	Time lag [s]
ζ_A	Aerodynamic damping ratio
ζ_D	Damping ratio from additional damping devices
ζ_S	Structural damping ratio
ζ_T	Total damping ratio
ω_d	Damped natural frequency
$*$	Transpose

Abbreviations

BSS	Blind Source Separation
CFD	Computational Fluid Dynamics
DOF	Degree-of-freedom
FE	Finite-element
LES	Large-eddy Simulation
RDT	Random Decrement Technique
SOBI	Second-order Blind Identification
SSI	Stochastic Subspace Identification
WF	Wind-field

1. Introduction

Natural wind is one of the most common dynamic loads experienced by structures and can range from a gentle breeze to chaotic forms such as gales, tornados, and hurricanes. These wind loads are especially important during the design of tall and slender structures as they exhibit higher deflections and aeroelastic effects. Aerodynamics are also critical for slender structures, as they are especially vulnerable to motion that is perpendicular to the flow of the wind. The design and health monitoring of structures include the detection of modal parameters, such as damping ratios, which indicates a structure's ability to resist motion. The estimation of damping is important for both the design of slender structures, as well as existing structures to ensure they are performing safely and that no additional damping devices are required.

Accurate damping estimation is important for the design of newer slender structures, and the assessment of existing structures, as damping reduces the overall response of the structure. All structures have some form of inherent damping, known as *structural damping* that is dependent on the materials used to build the structure. However, when a slender structure (e.g., tall building and tower, long-span bridge, chimney, transmission tower, antenna, etc.) is exposed to wind loading, a phenomenon known as *aerodynamic damping* arises, which causes the total damping in the structure to be different than the structural damping. Aerodynamic damping is an important parameter of the slender structures, as it can often exhibit a negative value, especially in the across-wind direction. Under such a situation, the aerodynamic damping amplifies the wind-induced vibration response of the structures that may lead to severe structural damage or catastrophic failure.

1.1 Aerodynamic Damping

The total damping ratio is shown in the following:

$$\zeta_T = \zeta_S + \zeta_A + \zeta_D \tag{1.1}$$

where ζ_T is the total damping ratio, ζ_S is the structural damping ratio, ζ_A is the aerodynamic damping ratio, and ζ_D is the damping ratio from additional damping devices. For this research, no additional damping devices are investigated, meaning $\zeta_D = 0$. Therefore, the ultimate goal of this research, ζ_A, is acquired using the following expression:

$$\zeta_A = \zeta_T - \zeta_S \tag{1.2}$$

Statistical methods can determine ζ_T by autocorrelating the modal responses of the forced vibration of a dynamic system; however, the free decay of the response is required to estimate ζ_S. Therefore, a free vibration test is performed to determine ζ_S, which is often not the same value as ζ_T, especially for structures excited by a wind field.

The wind-induced response of structures is influenced by the incoming turbulence of the wind, vortex shedding, and lock-in from motion-induced force (Davenport, 1968). Turbulence is the chaotic change in wind velocity and is accompanied by vortices that exhibit many different sizes. Vortex shedding occurs when the wind wraps around a structure, creating vortices at the sides that apply a force that is perpendicular to the flow of the wind. The along-wind direction is parallel to the flow of the wind, while the across-wind direction is perpendicular to the flow, as shown in figure 1.1.
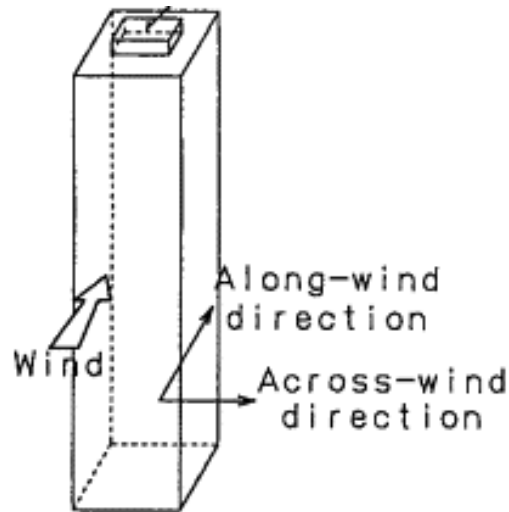
Figure 1.1: Along-wind and across-wind directions relative to a typical rectangular building, (Tsukagoshi *et al.* 1993).

While the along-wind response is characterized by the turbulence and quasi-steady theory, the across-wind response is determined by the vortex shedding, meaning the quasi-steady theory cannot be used. Vortex shedding may create a phenomenon called *lock-in*, meaning the wake flow's frequency matches the natural frequency of the structure, which generates a larger response and the potential for negative aerodynamic damping. Figure 1.2 shows an example of vortex shedding around a cylindrical structure, and figure 1.3 shows the lock-in phenomena.
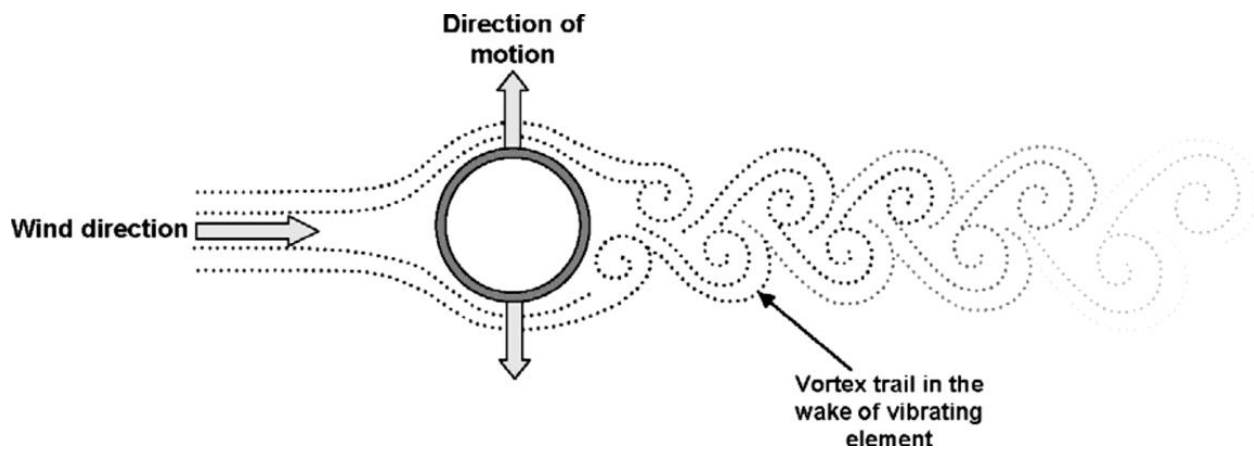
Figure 1.2: Vortex shedding affecting a cylindrical structure (Rice *et al*. 2008).
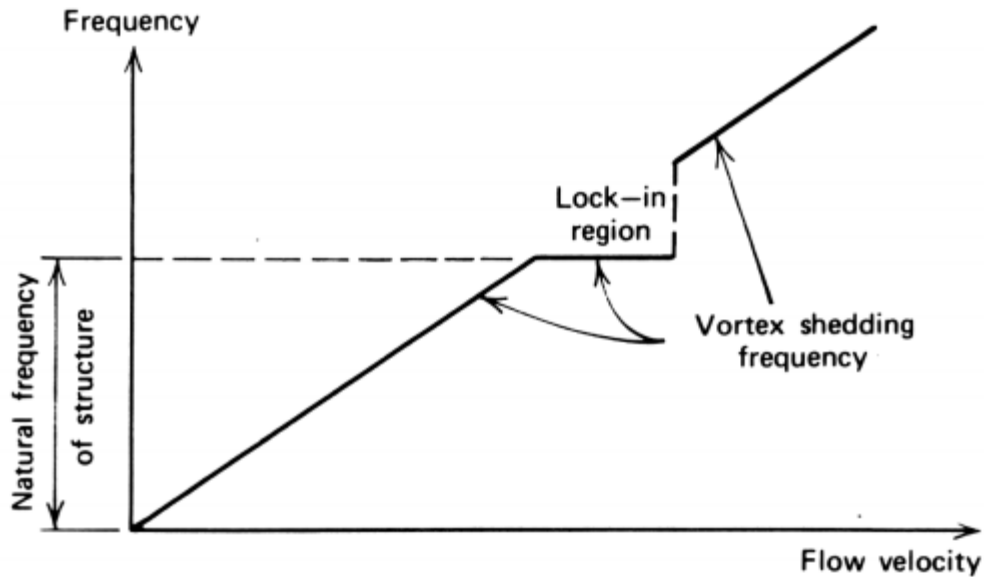
Figure 1.3: Lock-in phenomena (Simiu and Scanlan 1996).

Negative damping often indicates the need for additional damping devices to reduce the response of the structure. The estimation of aerodynamic damping requires the need for a robust and accurate system identification, where the unknown modal parameters (i.e., natural frequencies, damping and mode shapes) are estimated from the measured vibration data of the structures.

Since the last few decades, various researchers have actively investigated the estimation of aerodynamic damping of slender structures using both wind tunnel and full-scale data. Davenport (1971) performed turbulent wind experiments on six different tall building models with varying cross-sections and structural properties. Each model exhibited low damping; therefore the measured responses were narrowband, meaning the responses were Gaussian in nature and were restricted around the resonance of the building. The peak responses of the models were analyzed using a type 1 extreme distribution and a Rayleigh distribution for wind speed. The circular cross-section building showed the lowest values of peak deflection, while rectangular and triangle-shaped models demonstrated the highest responses. Davenport (1984) also estimated the along-

wind and across-wind response of the slender chimneys. The along-wind response was used to derive a theoretical equation to calculate the aerodynamic damping ratio in the along-wind direction. Across-wind response incorporated wake excitation and vortex shedding and was used to estimate the largest negative aerodynamic damping ratio in the across-wind direction. These formulations were demonstrated on a 200 m tall chimney and a wind profile that followed the power law. Marukawa *et al.* (1996) examined aerodynamic damping of tall building models using wind tunnel test data of various building models with varying size and aspect ratios. The random decrement technique (RDT) was used to find the total damping ratio from the time series of the response. The structural damping ratio, found using free vibration tests, was then subtracted from the total damping ratio to find the aerodynamic damping ratio. It was found that the aerodynamic damping ratio exhibited positive values in the along-wind direction and negative values in the across-wind direction.

Cao *et al.* (2012) performed wind-tunnel experiments on aero-elastic models with different values of roughness exposure, structural damping, stiffness, and taper ratio to determine the along-wind aerodynamic damping ratios using the random decrement technique. Experiments showed that the aerodynamic damping hardly increases depending on the roughness exposure, while the structural damping was found to have a large influence on the aerodynamic damping. Aerodynamic damping also increased as the taper ratio increased; slotted corners and chamfers with smaller ratios were found to decrease the aerodynamic damping. Venanzi and Materazzi (2012) investigated the across-wind aero-elastic response of tall buildings with square cross-sections. The aerodynamic damping ratio was then calculated from the responses using the Newton-Raphson technique. In the range of positive aerodynamic damping, the ratios calculated using the proposed method agreed with the ratios found from the wind tunnel tests. Chen (2014) analyzed the nonlinear

negative aerodynamic damping effect of tall buildings subjected to crosswind loading. The analysis used time-domain response simulations of a square building undergoing forced vibration in a wind tunnel, with the aerodynamic damping modeled as a nonlinear function of the building's displacement. The author developed a corresponding model as a function of the root-mean-square response; this was necessary to perform a frequency domain spectral analysis. The accuracy of the analysis was improved further by including non-Gaussian response characteristics by using the method of equivalent nonlinear equation, which approximated an equation for the damping that could be solved exactly.

Gu *et al.* (2014) conducted experiments on aero-elastic square building models to determine the across-wind aerodynamic damping ratio, using the random decrement technique. They observed that the aerodynamic damping decreases with the decrease in the chamfer ratio. In addition to the chamfer ratio, slot ratios between 5% and 10% and a taper ratio of 1% are most effective at restraining aero-elastic responses. Kim *et al.* (2016) conducted experiments on super tall building models with square and helical cross-sections to identify aerodynamic damping ratios, using the random decrement technique. Results showed that when the models were under along-wind direction loads, both the square and helical models displayed a similar trend for aerodynamic damping ratio, gradually increasing with reduced wind velocity and remaining positive. However, under across-wind direction loads, the aerodynamic damping ratio of the helical model was negative for lower reduced wind velocity and gradually increased to be positive, while the square model showed a reversed trend. Experimental studies (Kim *et al.* (2018)) were conducted to determine the aerodynamic damping and aero-elastic instability of a supertall helical building using along-wind and across-wind responses. Using the random decrement technique, results showed a decrease in displacement compared to square model tests, in both x and y directions.

The aerodynamic damping was found to be approximately zero in all wind directions, contrasted with square building models that sometimes have negative damping ratios. It has been observed that with increasing wind speed, the aerodynamic damping in the along-wind direction increases, while the damping in the across-wind direction tends to decrease. Figures 1.4 and 1.5 show the aerodynamic damping trend of a square building in the along-wind and across-wind directions, respectively.
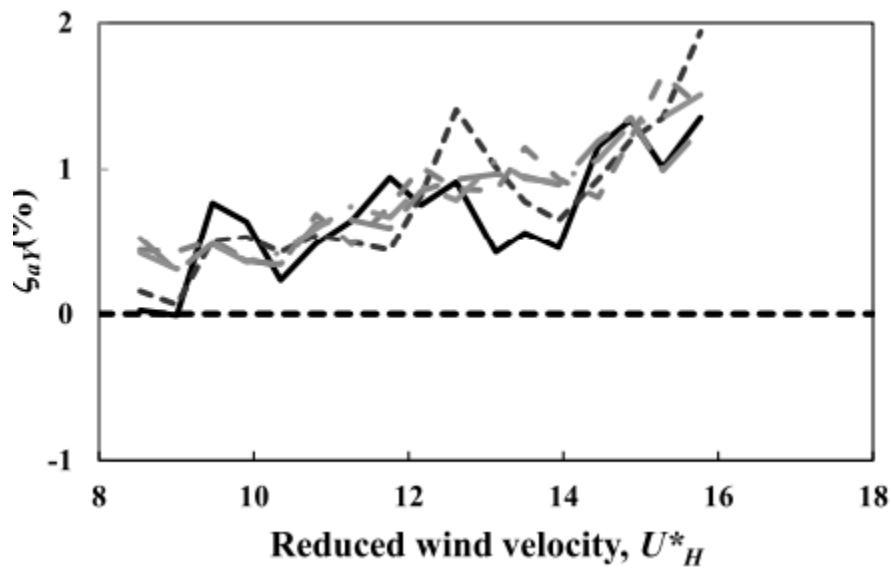
Figure 1.4: Wind velocity effect on aerodynamic damping of a square building, along-wind direction (Kim 2018).
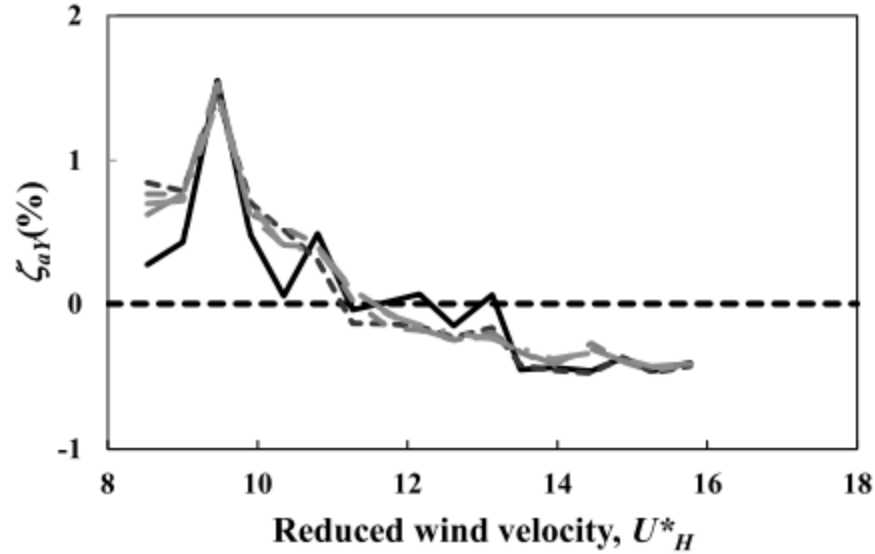
Figure 1.5: Wind velocity effect on aerodynamic damping of a square building, across-wind direction (Kim 2018).

The determination of the aerodynamic damping ratio for a structure is of great importance since it can exhibit a negative value, thus lowering the overall damping of the system. The estimate of aerodynamic damping requires a robust system identification technique to determine the modal parameters of a structure.

1.2   System Identification for Wind-induced Responses

System identification is a field of methods that use the statistical data of inputs and outputs to build mathematical models of a structure (Barbosh *et al.* 2018). These methods include deriving frequency-response functions if working in the frequency domain, and impulse-response functions if working in the time domain (Maia and Silva (2001)). The structure is treated like a black box where the parameters such as mass, damping, and stiffness are unknown, but the loads and responses are known. A variant of system identification, known as blind identification, uses only the output response of the structure to determine the modal parameters such as the mode shapes,

8

natural frequencies, and damping ratios. Various blind identification techniques (Sadhu 2013) have been used in the past to determine the modal parameters of slender structures under wind loading, including stochastic subspace identification (SSI) and RDT. SSI has been used extensively in the literature on civil structures undergoing traffic and wind loading. Recent studies involving SSI is covariance driven, involving the assembly of block Hankel matrices and stabilization diagrams. However, SSI requires a model order selection that needs a stabilization diagram, as detailed by Magalhaes *et al.* (2009). The stabilization diagram ensures accurate identification of modal parameters and adequate modal assurance criteria, however, it involves significant user intervention. Figures 1.6 and 1.7 show an example of a stabilization diagram and identified natural frequencies, respectively.
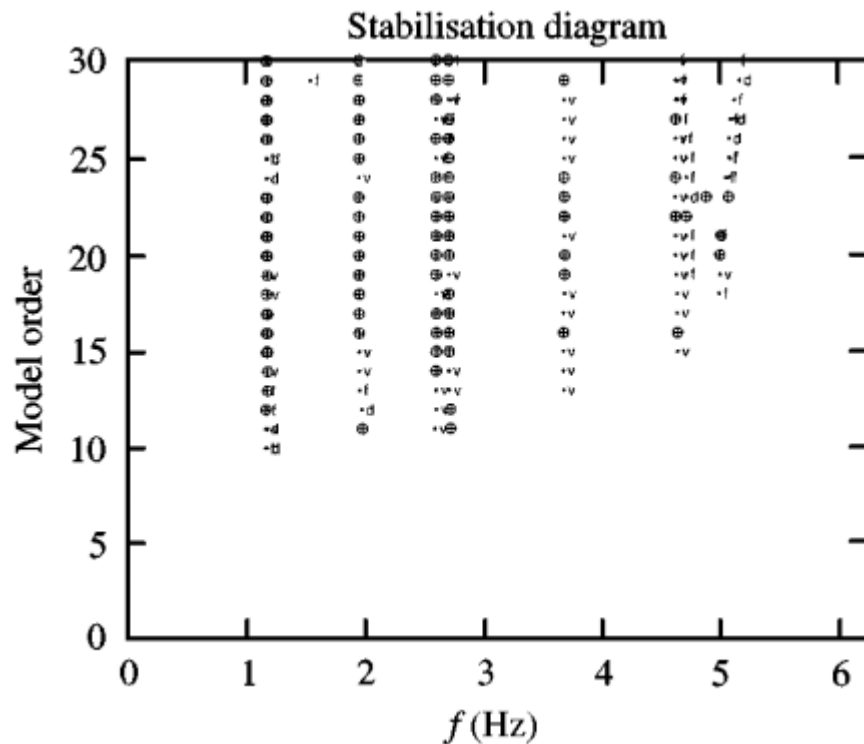
Figure 1.6: Stability diagram showing model order (Peeters and De Roeck 1999).
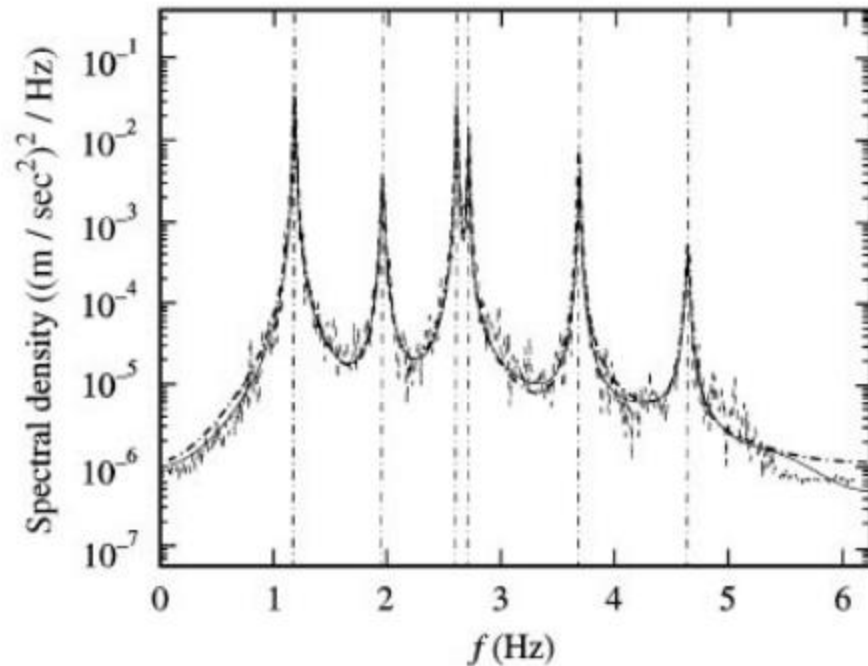
Figure 1.7: Identified natural frequencies using SSI (Peeters and De Roeck 1999).

Peeters and De Roeck (1999) used the SSI approach for modal analysis using only output data and incorporating Kalman filters. The method was applied on a steel mast exited by wind loads, using a grid of sensors to capture the acceleration response. It was determined that the accuracy of the estimated frequency and damping ratio was relatively low when compared to other system identification methods. Peeeters and De Roeck (2000) used the same SSI approach on a Monte Carlo simulation and a pre-stressed concrete bridge. The Monte Carlo simulation was performed on a finite-element simply supported beam with a white noise signal being applied to the beam. The concrete bridge was outfitted with accelerometers which captured response caused by traffic and wind loads. Similarly, it was found that the obtained modal parameters were similar to values acquired from the traditional system identification methods. Yu and Ren (2005) combined SSI with empirical mode decomposition for structural health monitoring. The traffic-induced acceleration response of a steel tubular arch bridge was captured; only the output was considered

for this method. The proposed system identification method successfully decomposed the output into a set of intrinsic mode functions. Reynders and Roeck (2008) introduced a combined deterministic SSI technique to estimate the modal parameters of a bridge. The deterministic method proved to more efficient at identifying modes compared to older stochastic subspace identification techniques. Reynders *et al.* (2008) also analyzed the uncertainty of using a covariance-driven SSI algorithm on simulated and measured data. The test setup was performed on a finite-element beam with an applied white noise signal, and vibration data obtained from a steel antennae mast. It was found that the damping ratios varied too greatly from other system identification methods, confirming that the accuracy of the proposed technique remained uncertain. Loh *et al.* (2011) used recursive SSI for near real-time structural damage diagnosis. Similar to the conventional methods, the experimental setup utilized only the output response of the structure; the structure was a bridge pier model built in a laboratory. The technique incorporated Kalman filters, and successfully identified dynamic parameters through continuous monitoring. Wu *et al.* (2016) obtained modal properties of structures with closely spaced modes using an upgraded SSI method. The civil structures that were analyzed include the cables and deck of a cable-stayed bridge and a 13-story steel frame office building. The proposed algorithm was successful in identifying the modes of both structures with reasonable accuracy and was more efficient when compared to traditional methods.

RDT is another system identification method that has been used extensively in the past. According to Rodrigues and Brincker (2005), RDT operates by taking the responses of a structure and transforming them into random decrement functions. Figure 1.8 shows different trigger points to estimate the random decrement functions.
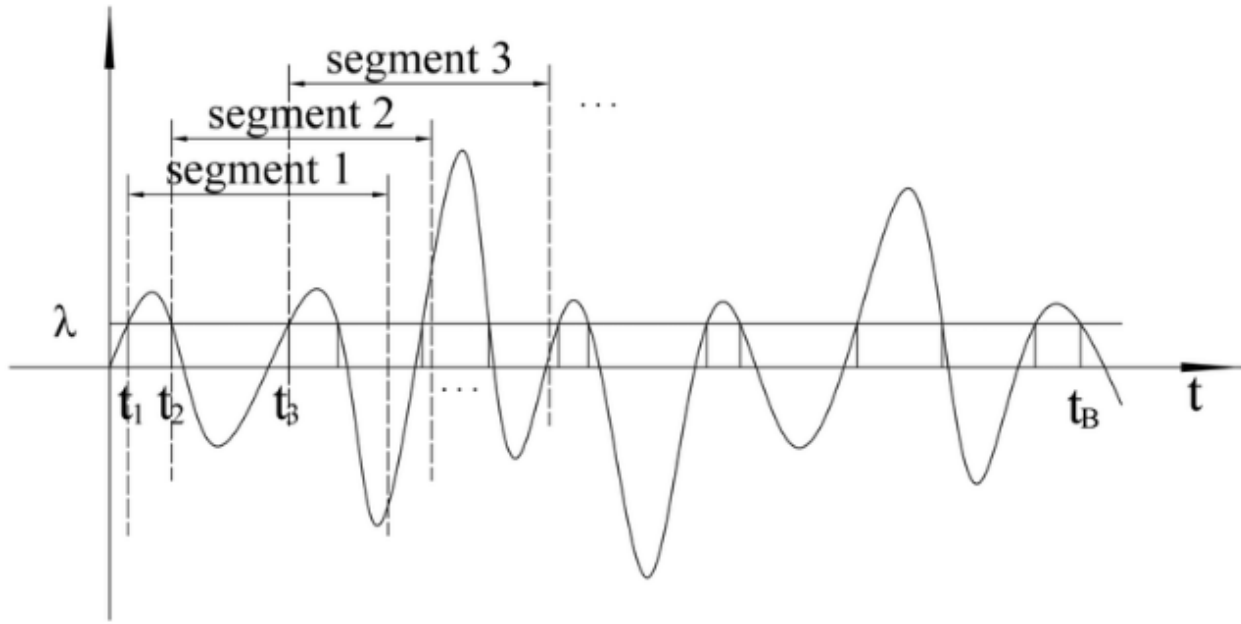
Figure 0.8: Tigger points to estimate random decrement functions (Feng *et al*. 2017).

Yang *et al.* (1984) performed an RDT analysis of civil structures to estimate structural damping ratios. The test setup included scaled laboratory models of an existing steel offshore platform and a multi-degree-of-freedom finite-element model. Structural damping ratio estimates proved to be accurate, as long as the input into the system was random. A mathematical basis for RDT was formulated by Vandiver *et al.* (1982) incorporating the autocorrelation of response data. Vibration data from an offshore platform was analyzed using the proposed mathematical formulation and was compared to results obtained from the autocorrelation function. By using the averages of a large number of segments of the response, it was shown that RDT can approximate the autocorrelation function. Asmussen (1997) performed RDT to find the modal parameters of two existing bridges and a laboratory bridge model. It was shown that the accuracy of the damping ratio estimation needs to be improved, and requires more trigger points. Natural frequency detection was possible for the second bridge, but acquiring the mode shapes for all modes was not possible. The bridge model was loaded with white noise and showed high damping ratio estimation

accuracy. Rodrigues *et al.* (2004) used RDT to improve upon the traditional frequency-domain modal identification methods. The process was applied to the acceleration output of a scaled four-story laboratory model; Fourier analysis was used on the random decrement technique results. The spectral densities showed low amounts of noise, and modal parameters were very similar when compared to the results using earlier methods. RDT with empirical mode decomposition was combined by He *et al.* (2011) to examine nonstationary output data. The proposed method was used on response data obtained from the finite-element bridge model and an existing steel truss bridge. The combined method agreed well with a traditional identification technique, known as peak picking. Wen *et al.* (2018) combined RDT with analytical mode decomposition to determine modal parameters of structures with closely spaced modes. The method was demonstrated on a four degree of freedom mass-spring-damper system and an existing curved cable-stayed bridge. The modal properties agreed with values estimated using the traditional random decrement technique and stochastic subspace identification. Huang and Gu (2016) identified nonlinear damping ratios of tall buildings using an envelope RDT approach. The technique was used on the response from numerical simulations and a supertall building outfitted with an accelerometer at the top. The damping ratio estimates and errors were compared with the estimates obtained from earlier methods.

1.3 Gap Areas

The previous system identification techniques have proven to be useful in certain vibration analysis applications; however, many of these methods are tedious and often fail to identify closely spaced modes of slender structures. For example, RDT is often used to determine the parameters of single-degree-of-freedom systems, such as stick models in wind tunnels, and is not explored for

estimation of aerodynamic properties of slender structures with multiple modes. SSI has had many recent advances including covariance-driven methods and has been used for structures undergoing wind excitation. However, SSI requires sophisticated knowledge related to block Hankel matrices and the determination of the model order for the stabilization diagram. Traditional system identification methods usually assume that modal responses are stationary and do not contain mixed-modal responses. Also, if there is any unwanted noise contained within a signal, the traditional system identification methods may not be able to separate it from the measured signal. Without proper modal identification and noise separation in slender structures, there is limited confidence in the estimation of aerodynamic damping.

1.4   Research Objectives

A state-of-the-art system identification method, known as Second-order Blind Identification (SOBI), is implemented in this paper to determine the modal responses and aerodynamic damping of slender structures, under the assumption the structure contains mixed-modal responses.

The SOBI technique is performed on a finite-element chimney model subjected to two different simulated wind fields, one simulation using pre-determined aerodynamic coefficients, and the other simulation using computational fluid dynamics (CFD). The aerodynamic damping ratios acquired from these two simulations are compared to each other to determine if there are any trends in damping estimates depending on the simulation method used. The damping estimates acquired using SOBI is known as the total damping ratio, which is the summation of the structural damping, aerodynamic damping, and damping from devices such as tuned mass dampers. The first step toward acquiring ζ_A is to have an understanding of SOBI and how it can estimate ζ_T, which is detailed in **chapter 2**. After formulating SOBI, three different load cases are tested on simulated

14

models to demonstrate the efficiency and robustness of the method. **Chapter 3** details the wind field simulations using both pre-determined aerodynamic coefficients and CFD. **Chapter 4** highlights the finite-element modeling of a chimney, how the two different wind fields are applied to the model and the output response that will be used for SOBI. Finally, **chapter 5** showcases the modal analysis results of the chimney model using SOBI and concludes with the estimation of aerodynamic damping for the first four modes. The key conclusions and future work of the current thesis are presented in **chapter 6**.

1.5   References

Asmussen, J. C. (1997). "Modal analysis based on the random decrement technique: application to civil engineering structures" [Doctor of Philosophy Thesis]. *Aalborg University.*

Barbosh, M., Sadhu, A., and Vogrig, M. (2018), "Multi-sensor based hybrid empirical empirical mode decomposition method towards system identification of structures", *Structural Control and Health Monitoring*, 25(5), e2147.

Cao, H., Quan, Y., Gu, M., and Wu, D. (2012). "Along-wind aerodynamic damping of high-rise buildings". *The Seventh International Colloquium on Bluff Body Aerodynamics and Applications, Shanghai, China, September 2-6,* 813-824.

Chen, X. (2014). "Analysis of crosswind fatigue of wind-excited structures with nonlinear aerodynamic damping". *Engineering Structures,* 74, 145-156.

Cheng, C. M., Lu, P. C., and Tsai, M. S. (2002). "Acrosswind aerodynamic damping of isolated square-shaped buildings". *Journal of Wind Engineering and Industrial Aerodynamics,* 90, 1743-1756.

Cheynet, E. (2020). Operational modal analysis with automated SSI-COV algorithm (https://www.github.com/ECheynet/SSICOV), GitHub. Retrieved April 19, 2020.

Davenport, A.G. (1968). "Response of structures to turbulent wind". *The Journal of the Acoustical Society of America,* 44, 364.

Davenport, A. G. (1971). "The response of six building shapes to turbulent wind". *Philosophical Transactions of the Royal Society A,* 269, 385-394.

Davenport, A.G. (1984). "The response of chimneys to wind". *Proceedings of the 5th International Chimney Congress, Essen, West Germany, October 3-5*, 77-84.

Feng, Z., Shen, W., and Chen, Z. (2017). "Consistent level RDT-ERA for output-only ambient modal identification of structures". *International Journal of Structural Stability and Dynamics,* 01, 1750106.

Gu, M., Cao, H. L., and Quan, Y. (2014). "Experimental study of across-wind aerodynamic damping of super high-rise buildings with aerodynamically modified square cross-sections". *The Structural Design of Tall and Special Buildings,* 23, 1225-1245.

He, X. H., Hua, X. G., Chen, Z. Q., and Huang, F. L. (2011). "EMD-based random decrement technique for modal parameter identification of an existing railway bridge". *Engineering Structures,* 33, 1348-1356.

Huang, Z. and Gu, M. (2016). "Envelope random decrement technique for identification of nonlinear damping of tall buildings". *Journal of Structural Engineering,* 142, 04016101.

Kim, W., Yi, J. H., Tamura, Y., Ohtake, K., and Yoshida, A. (2016). "Aerodynamic damping of helical shaped super tall building". *Advances in Civil, Environmental, and Materials Research, Jeju Island, Korea, August 28-September 1,* 1-11.

Kim, W., Yoshida, A., Tamura, Y., and Yi, J. H. (2018). "Experimental study of aerodynamic damping of a twisted supertall building". *Journal of Wind Engineering and Industrial Aerodynamics,* 176, 1-12.

Loh, C. H., Weng, J. H., Liu, Y. C., Lin, P. Y., and Huang, S. K. (2011). "Structural damage diagnosis based on on-line recursive stochastic subspace identification". *Smart Materials and Structures,* 20, 055004.

Magalhaes, F., Cunha, A., and Caetano, E. (2009. "Online automatic identification of the modal parameters of a long span arch bridge". *Mechanical Systems and Signal Processing,* 23, 316-329.

Maia, N. M. M. and Silva, J. M. M. (2001). "Modal analysis identification techniques". *Philosophical Transactions of the Royal Society A,* 359, 29-40.

Marukawa, H., Kato, N., Fujii, K., and Tamura, T. (1996). "Experimental evaluation of aerodynamic damping of tall buildings". *Journal of Wind Engineering and Industrial Aerodynamics,* 59, 177-190.

Morgenthal, G. (2000). "Fluid-structure interaction in bluff-body aerodynamics and long-span bridge design: phenomena and methods". *Technical Report No. CUED/D-Struct/TR.187,* University of Cambridge, Department of Engineering.

Peeters, B. and De Roeck, G. (1999). "Reference-based stochastic subspace identification for output-only modal analysis". *Mechanical Systems and Signal Processing,* 13, 855-878.

Peeters, B. and De Roeck, G. (2000). "Reference-based stochastic subspace identification in civil engineering". *Inverse Problems in Engineering,* 8, 47-74.

Reynders, E. and De Roeck, G. (2008). "Reference-based combined deterministic-stochastic subspace identification for experimental and operational modal analysis". *Mechanical Systems and Signal Processing,* 22, 617-637.

Reynders, E., Pintelon, R., and De Roeck, G. (2008). "Uncertainty bounds on modal parameters obtained from stochastic subspace identification". *Mechanical Systems and Signal Processing,* 22, 948-969.

Rice, J. A., LaFave, J. M., and Mehuys, C. H. (2008). "End connection effects on vortex shedding susceptibility of welded aluminum truss tubular web members". *Journal of Performance of Constructed Facilities,* 22, 297-304.

Rodrigues, J., Brincker, R., and Andersen, P. (2004). "Scaling the mode shapes of a building model by mass changes". *www.semanticscholar.org.*

Rodrigues, J. and Brincker, R. (2005). "Application of the random decrement technique in operational modal analysis". *www.researchgate.net.*

Sadhu, A. "Decentralized ambient system identification of structures." *PhD Thesis*, *Department of Civil and Environmental Engineering*, University of Waterloo, 2013.

Simiu E, Scalan R. Wind Effects on Structures. John Wiley and Sons Inc., 1996.

Tsukagoshi, H., Tamura, Y., Sasaki, A., and Kanai, H. (1993). "Response analysis on along-wind and across-wind vibrations of tall buildings in time domain". *Computational Wind Engineering 1*, 497-506.

Vandiver, J. K., Dunwoody, A. B., Campbell, R. B., and Cook, M. F. (1982). "A mathematical basis for the random decrement vibration signature analysis technique". *Journal of Mechanical Design,* 104, 307-313.

Venanzi, I. and Materazzi, A. L. (2012). "Acrosswind aeroelastic response of square tall buildings: a semi-analytical approach based of wind tunnel tests on rigid models". *Wind and Structures*, 15, 1-14.

Wen, Q., Hua, X. G., Chen, Z, Q., Niu, H. W., and Wang, X. Y. (2018). "AMD-based random decrement technique for modal identification of structures with close modes". *Journal of Aerospace Engineering,* 31, 04018057.

Wu, W. H., Wang, S. W., Chen, C. C., and Lai, G. (2016). "Application of stochastic subspace identification for stay cables with an alternative stabilization diagram and hierarchical sifting process". *Structural Control and Health Monitoring,* 23, 1194-1213.

Yang, J. C. S., Chen, J., and Dagalakis, N. G. (1984). "Damage detection in offshore structures by the random decrement technique". *Journal of Energy Resources and Technology,* 106, 38-42.

Yu, D. J. and Ren, W. X. (2005). "EMD-based stochastic subspace identification of structures from operational vibration measurements". *Engineering Structures,* 27, 1741-1751.

2 Second-order Blind Identification

Second-order Blind Identification (SOBI) has shown significant promises over other traditional system identification methods as it requires only output (i.e., measurement data) to estimate modal parameters instead of using both input and output information. Due to its dependence only on the measured data, SOBI is especially suitable for large-scale civil structures where the input (i.e., wind data) may not be known at all locations. SOBI (Belouchrani *et al.* (1997)) is based on second-order statistics, such as auto-correlation, and separates the hidden sources from their noisy mixtures. In this chapter, the modal identification formulation of SOBI will be demonstrated. Three examples are then used to demonstrate the SOBI method: a mixture of four sine signals, a 10 degree-of-freedom (DOF) model undergoing a base excitation, and the Gaussian random floor excitations. In the subsequent chapters, it will be illustrated how SOBI can be used to estimate the aerodynamic damping of a slender structure from its wind-induced vibration.

2.1 Formulation

SOBI, a variant of Blind source separation (BSS) (Sadhu *et al.* 2017), assumes that a signal is a mixture of the unknown source signals and measurement noise. A classical analogy for BSS is a cocktail party problem, where multiple people in a room may be speaking at once. In this case, BSS would provide an excellent solution to separate the speech from each person recorded by the microphones. This mixture is represented in the following matrix form:

$$\boldsymbol{x}(t) = \boldsymbol{y}(t) + \boldsymbol{n(t)} = \mathbf{A}\boldsymbol{s}(t) + \boldsymbol{n}(t) \tag{2.1}$$

where $\boldsymbol{x}(t)$ is the mixed signal, $\mathbf{A}$ is the mixing matrix, $\boldsymbol{s}(t)$ is the source signal, and $\boldsymbol{n}(t)$ is the measurement noise. The main goal of BSS is to determine the unknown mixing matrix, which can be used to find the unknown source signals. According to the literature (Jutten and Herault, 1991; Hyvarinen and Oja, 2000), the most popular BSS method is Independent Component Analysis (ICA); however, ICA is computationally expensive as it requires higher-order statistics of the signal, such as the approximate form of the probability distribution function of the unknown sources. On the other hand, SOBI relies only on second-order statistics, as it aims to simultaneously diagonalize a set of time-lagged covariance matrices. SOBI assumes that the source signals are uncorrelated; therefore, the covariance matrix at zero lag is as follows (Belouchrani $et\ al.$ (1997)):

$$\mathbf{R}_x(0) = E[\boldsymbol{x}(t)\boldsymbol{x}^*(t)] = \mathbf{A}\mathbf{A}^H + E[\boldsymbol{n}(t)\boldsymbol{n}^*(t)] = \mathbf{A}\mathbf{A}^H + \boldsymbol{n}^2\mathbf{I} \qquad (2.2)$$

where * denotes the transpose of the matrix, H is the complex conjugate transpose of the matrix, and $\mathbf{I}$ is an identity matrix. Once the covariance matrix is formed, SOBI is performed using a two-step process: (a) whitening and (b) unitary transformation. The purpose of whitening the measured signal is to remove the unwanted noise, which is accomplished by a linear transformation of $\boldsymbol{y}(t)$:

$$E[\mathbf{W}\boldsymbol{y}(t)\boldsymbol{y}^*(t)\mathbf{W}^H] = \mathbf{W}\mathbf{A}\mathbf{A}^H\mathbf{W}^H \qquad (2.3)$$

where $\mathbf{W}$ is the whitening matrix and is represented in the following form:

$$\mathbf{W} = \mathbf{D}^{-\frac{1}{2}}\mathbf{V}^H \qquad (2.4)$$

where $\mathbf{D}$ is the diagonal matrix of eigenvalues and $\mathbf{V}$ is the eigenvector matrix of $\mathbf{R}_x(0)$. It can also be shown that a unitary matrix exists for every whitening matrix (Belouchrani $et\ al.$ (1997)):

$$\mathbf{W}\mathbf{A}\mathbf{A}^H\mathbf{W}^H = \mathbf{U}\mathbf{U}^H = \mathbf{I} \qquad (2.5)$$

21

where $\mathbf{U} = \mathbf{WA}$. Since it is assumed that noise is present, this means $x(t) \neq y(t)$ and that the whitening process will conclude in the following form:

$$E[z(t)z^*(t)] = E[\mathbf{W}x(t)x^*(t)\mathbf{W}^H] \tag{2.6}$$

$$= \mathbf{WAA}^H\mathbf{W}^H + \mathbf{W}n^2\mathbf{W}^H$$

$$= \mathbf{W}(\mathbf{R}_x(0) - n^2 I)\mathbf{W}^H + \mathbf{W}n^2\mathbf{W}^H$$

$$= \mathbf{WR}_x(0)\mathbf{W}^H \tag{2.7}$$

where $z(t) = \mathbf{W}x(t)$. After the removal of the noise, the next step is unitary transformation, which involves diagonalizing the whitened covariance matrix to determine the unitary matrix. The unitary matrix is found as follows (Belouchrani *et al.* (1997)):

$$\mathbf{R}^W(\tau) = \mathbf{UR}_s(\tau)\mathbf{U}^H \tag{2.8}$$

where $\mathbf{R}_s(\tau) = E[s(t+\tau)s^*(t)]$ and $\mathbf{R}_s(\tau)$ is the time-lagged covariance matrix. Cardoso and Souloumiac (1996) showed that simultaneously diagonalizing many (say, *p*) time-lagged covariance matrices improves the robustness of SOBI. Now that $\mathbf{U}$ is known, the mixing matrix $\mathbf{A}$ is found using:

$$\mathbf{A} = \mathbf{UW}^{-1} \tag{2.9}$$

With the known mixing matrix, the source signals are solved using:

$$s(t) = \mathbf{A}^{-1}x(t) \tag{2.10}$$

2.2 Equivalence of SOBI with Modal Identification

The equation of motion for a multi-degree-of-freedom damped system is as follows:

$$\mathbf{M}\ddot{x}(t) + \mathbf{C}\dot{x}(t) + \mathbf{K}x(t) = f(t) \tag{2.11}$$

where $\mathbf{M}$, $\mathbf{C}$, and $\mathbf{K}$ are the mass, damping, and stiffness matrices, respectively, $f(t)$ is the force vector, and $x(t)$ is the system response. Knowing that the response of a system is the superposition of its modal responses, the following equation becomes analogous to the BSS equation:

$$x(t) = \mathbf{\Phi}q(t) \tag{2.12}$$

where $q(t)$ is the modal response and $\mathbf{\Phi}$ is the mode shape matrix. In the realm of structural dynamics and considering the analogy of this equation with the BSS equation, the formulation of determining $s(t)$ is similar to the classical modal superposition where $s(t)$ is the modal response and $\mathbf{A}$ is the mode shape matrix. Therefore, SOBI can perform modal identification to determine the mode shapes and the modal responses of a dynamic system. If it is assumed that the virtual sources used during BSS are the same as the coordinates of the system responses and vibration modes (Poncelet *et al.* 2017), then the mixing matrix $\mathbf{A}$ is identical to the mode shape matrix of the system.

SOBI excels at determining modal parameters (Musafere *et al.* 2015, Yuan *et al.* 2017), such as damping ratios, when compared to other BSS methods including ICA. However, SOBI has not yet been explored in estimating the aerodynamic responses of slender structures, which is invaluable information for monitoring and retrofitting of slender structures and forms the primary objective

of this thesis. Once SOBI has acquired the modal responses, the autocorrelation function on the modal response is used to estimate the damping ratios.

2.3 Autocorrelation of Modal Responses

Autocorrelation uses the basic ideas of determining the correlation of a data set and is estimated as the ensemble average of the product the signal with its delayed component (i.e., correlation of the data at a certain time lag to the data from a previous time). Once the modal responses are obtained from SOBI, autocorrelation is performed using the following formulation:

$$R_s(\tau) = \int_{-\infty}^{\infty} s(t)\overline{s(t-\tau)}dt \qquad (2.13)$$

where $s(t)$ is the modal response, $\overline{s(t)}$ is the complex conjugate of $s(t)$, and τ is the time lag.

The autocorrelation function shows that the further into the time-series the data is, the less correlated it will be compared to the data at zero time-lag. This means the function will produce a decaying periodical wave, where the decayed envelope may be used to find the damping ratio of the signal (i.e., the modal response). Figure 2.1 shows an example of a signal of a dynamic system, while figure 2.2 shows its corresponding autocorrelation function, as well as the fitted exponentially decayed envelope that is used to find the total damping ratio.
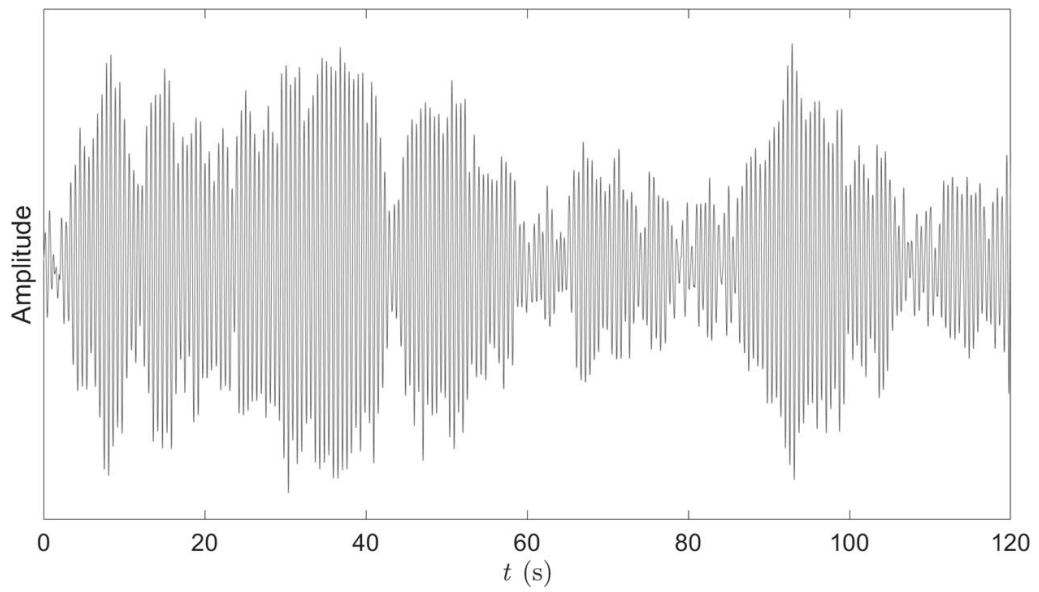
Figure 2.1: Example of a typical modal response of a typical dynamic system.
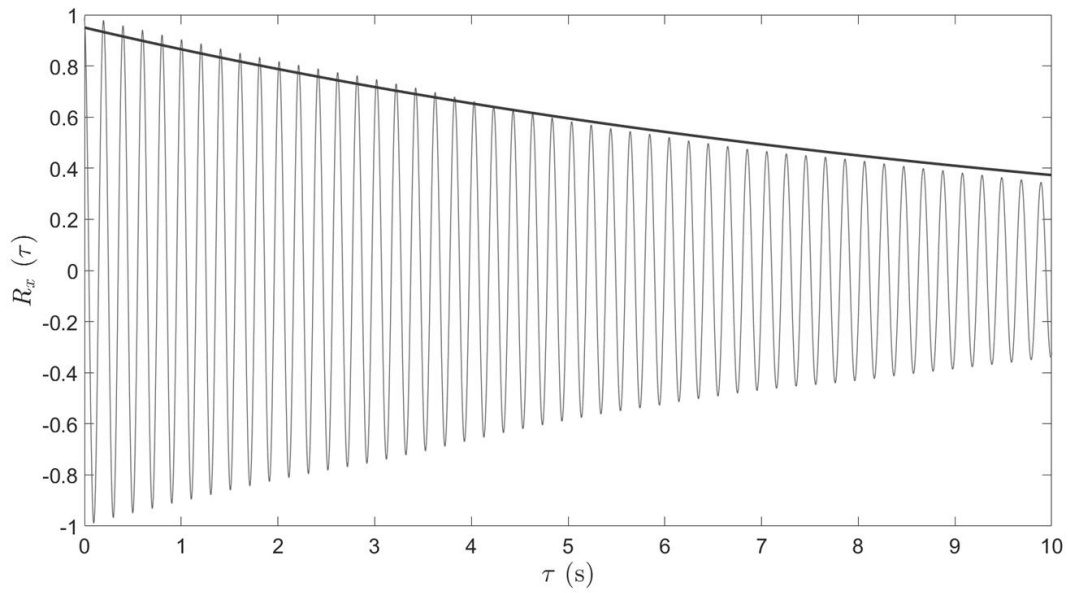
Figure 2.2: Autocorrelation function applied to the time history of the signal with a decaying curve.

2.4 Numerical Studies

In this sub-section, three examples including a mixture of sine signals and a 10 DOF model with base and floor excitation are used to illustrate the SOBI method.

2.4.1 Mixture of Sine Waves

SOBI is applied to a signal with four mixtures with each mixture containing a unique combination of sine wave functions of individual frequencies of 1, 2, 3 and 4 Hz, respectively. The mixtures are also accompanied by an additional white Gaussian noise to obscure the signal and test the robustness of SOBI under measurement noise. The signal has a total duration of 1200 s and a sampling rate of 20 Hz. Table 2.1 shows the sine wave functions associated with each source. The next step is to mix the four sine waves to check if SOBI is capable of separating the individual signals from their mixtures. Table 2.1 shows the details of the simulated mixed signals.

Table 2.1: Mixtures of four sine wave functions.

Mixture #	Mixed Signals
1	$3\sin(2\pi * 1 * t) + 2\sin(2\pi * 2 * t) + \sin(2\pi * 3 * t) + 4\sin(2\pi * 4 * t)$
2	$2\sin(2\pi * 1 * t) + 3\sin(2\pi * 2 * t) + 2\sin(2\pi * 3 * t) + 3\sin(2\pi * 4 * t)$
3	$4\sin(2\pi * 1 * t) + 2\sin(2\pi * 2 * t) + 3\sin(2\pi * 3 * t) + \sin(2\pi * 4 * t)$
4	$\sin(2\pi * 1 * t) + \sin(2\pi * 2 * t) + 3\sin(2\pi * 3 * t) + 2\sin(2\pi * 4 * t)$

Figures 2.3 and 2.4 show the mixtures of four sine wave responses added with white Gaussian noise and the separated signals as obtained from SOBI, respectively.
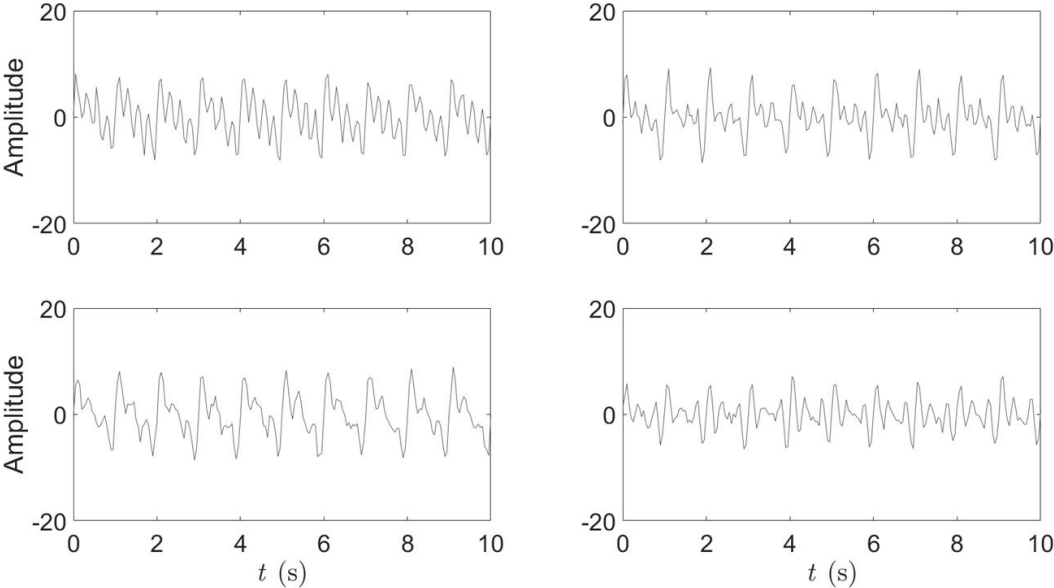
Figure 2.3: Mixture of sine wave functions with additional white Gaussian noise.
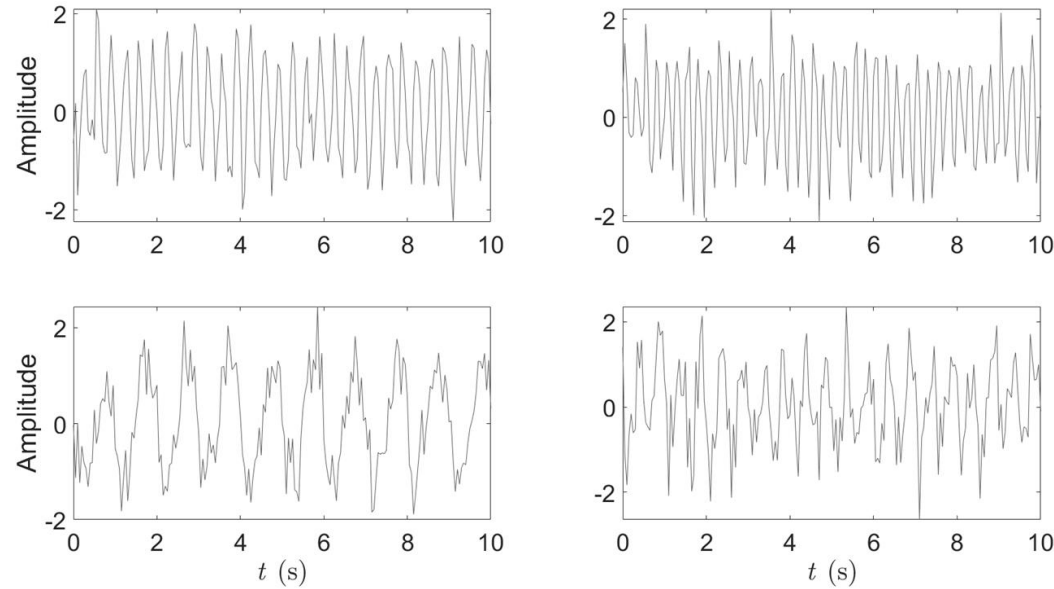
Figure 2.4: Individual sine signals extracted from their mixtures using SOBI.

SOBI is now applied to the responses of the sine wave mixture. Figure 2.5 shows the Fourier spectra of the individual signals, showing the natural frequencies of the source signals separated from the noise. Each plot clearly shows the frequency of the signals.
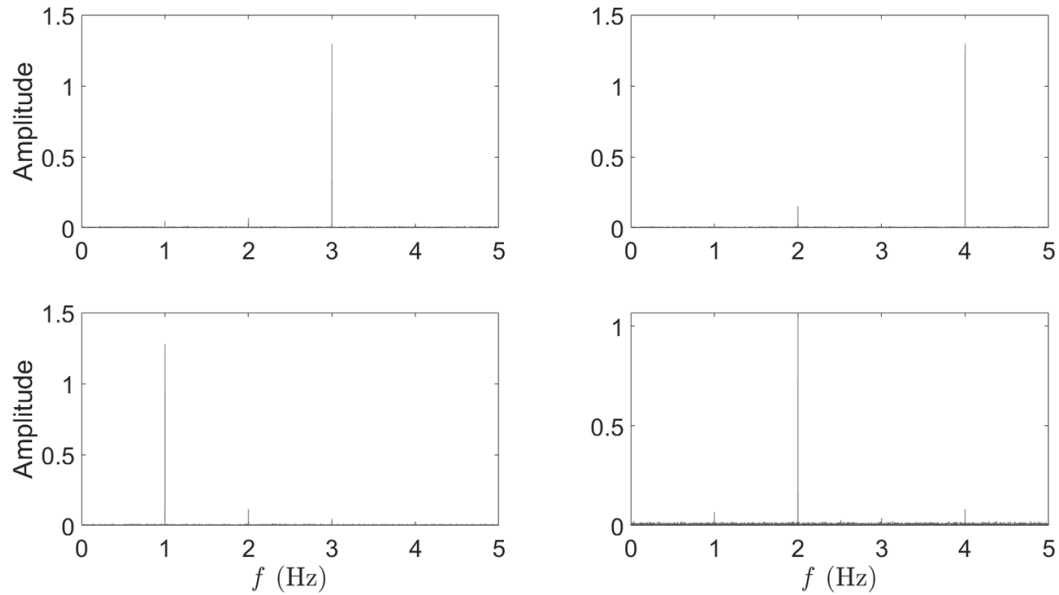
Figure 2.5: Fourier spectra of the extracted sine signals from their mixed signals.

2.4.2   10 Degree-of-freedom Model with a Base Excitation

SOBI is now applied to a 10 DOF state-space model, visualized as a 10-floor building subjected to base excitation. The state-space model is formulated as follows (Musafere *et al.* (2016)):

$$\dot{x} = \bar{\mathbf{A}}x + \bar{\mathbf{B}}u \qquad (2.14)$$

$$y = \bar{\mathbf{C}}x \qquad (2.15)$$

where x is the state vector, $\bar{A}$ is the state matrix, $\bar{B}$ is the input influence matrix, u is the ground acceleration, $\bar{C}$ is the observation matrix, and y is the response. $\bar{A}$ is dependent on the mass, damping, and stiffness of the model, as shown in the following:

$$\bar{A} = \begin{bmatrix} 0_{10x10} & I_{10x10} \\ -M^{-1}K & -M^{-1}C \end{bmatrix} \tag{2.16}$$

The mass matrix M is generically set to a diagonal matrix with 1 kg for all degrees-of-freedom, while for the damping matrix C, all modal damping ratios are set to 2%. For the stiffness matrix K, the first floor is set to 1750 kN/m, and stiffness at each subsequent floor decreases by 10% from the first-floor stiffness. The input influence matrix $\bar{B}$ and the observation matrix $\bar{C}$ are defined as follows:

$$\bar{B} = \begin{bmatrix} 0_{10x1} \\ -1_{10x1} \end{bmatrix} \tag{2.17}$$

$$\bar{C} = [-M^{-1}K \quad -M^{-1}C] \tag{2.18}$$

 Table 2.2 shows the natural frequencies of the model.

Table 2.2: Natural frequencies (f) of the 10 DOF model.

Mode #	1	2	3	4	5	6	7	8	9	10
f (Hz)	0.78	1.80	2.83	3.88	4.96	6.08	7.25	8.49	9.87	11.52

To simulate the response of the model, Imperial Valley earthquake data with a peak ground acceleration of 0.05g is used as the base excitation that has a total duration of 53.76s and a sampling rate of 50 Hz. The simulated response of each floor is shown in figure 2.6.
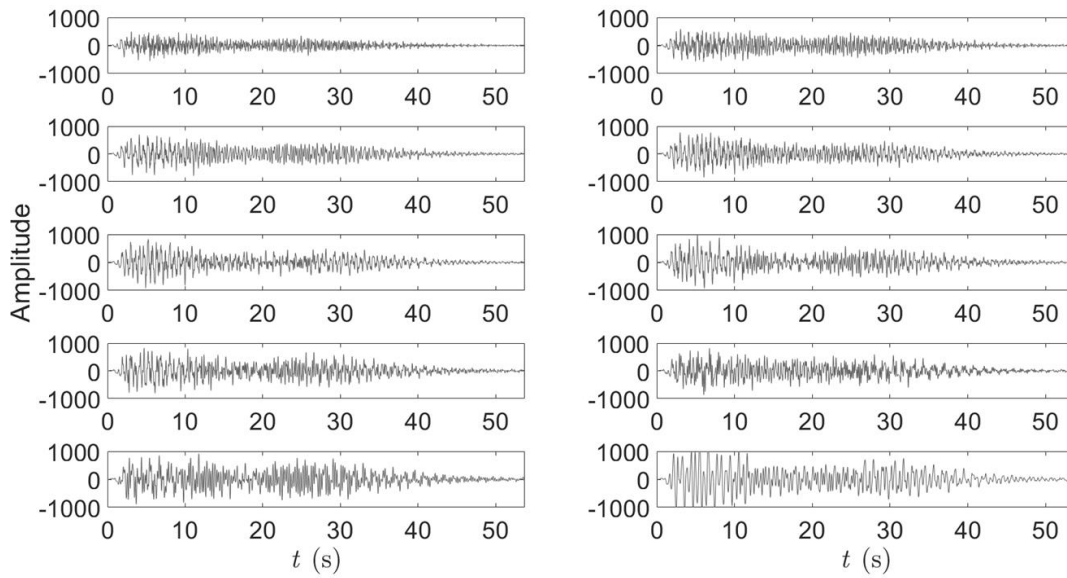
Figure 2.6: Simulated response of each floor for the 10 DOF model using the base excitation.

SOBI allows the input of a certain amount of time-lagged covariance matrices to be diagonalized simultaneously. To examine the effect of the number (p) of covariance matrices, three different values of p (1, 10, and 100) are used. Figures 2.7 and 2.8 show the modal response and the Fourier spectra of the modal response, respectively, after applying SOBI to the response, using $p=1$.
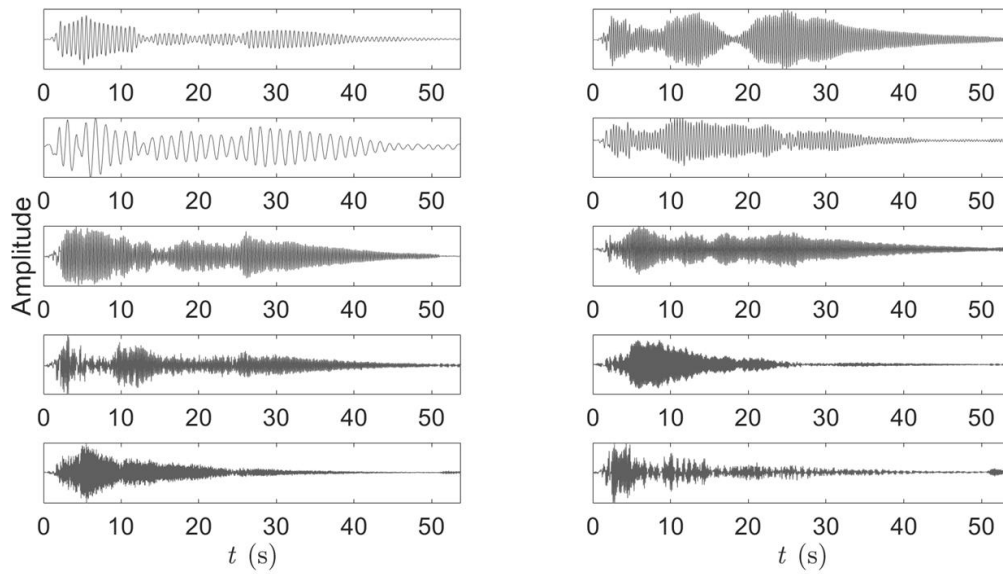
Figure 2.7: Modal responses of the 10 DOF model obtained from the responses of the base excitation using SOBI with *p* = 1.
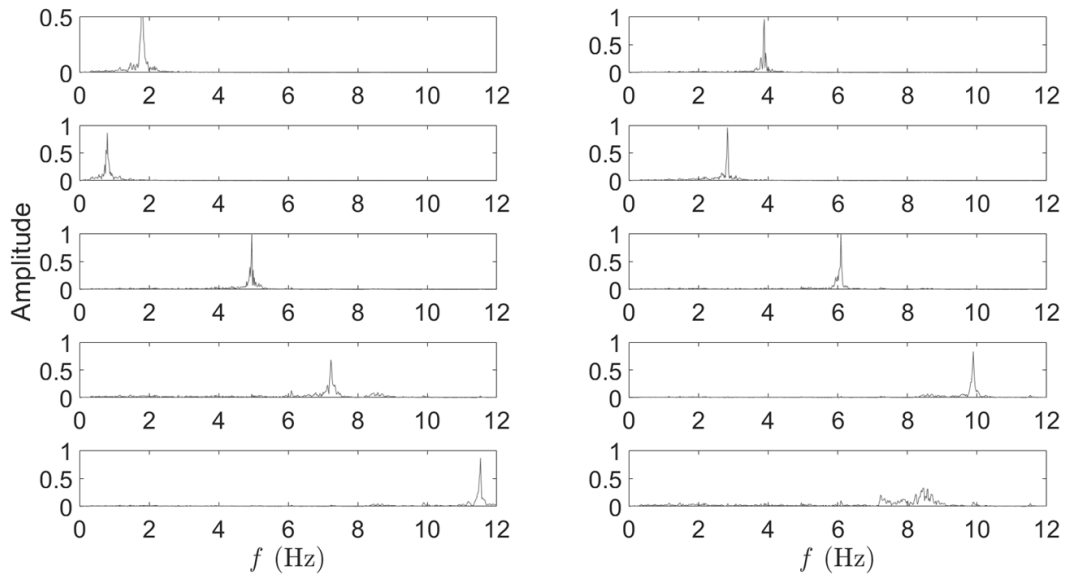
Figure 2.8: Fourier spectra of modal responses of the 10 DOF model (subjected to the base excitation) obtained from SOBI using *p* = 1.

Figures 2.9 and 2.10 show the modal response and Fourier spectra of the modal responses, respectively, using p=10.
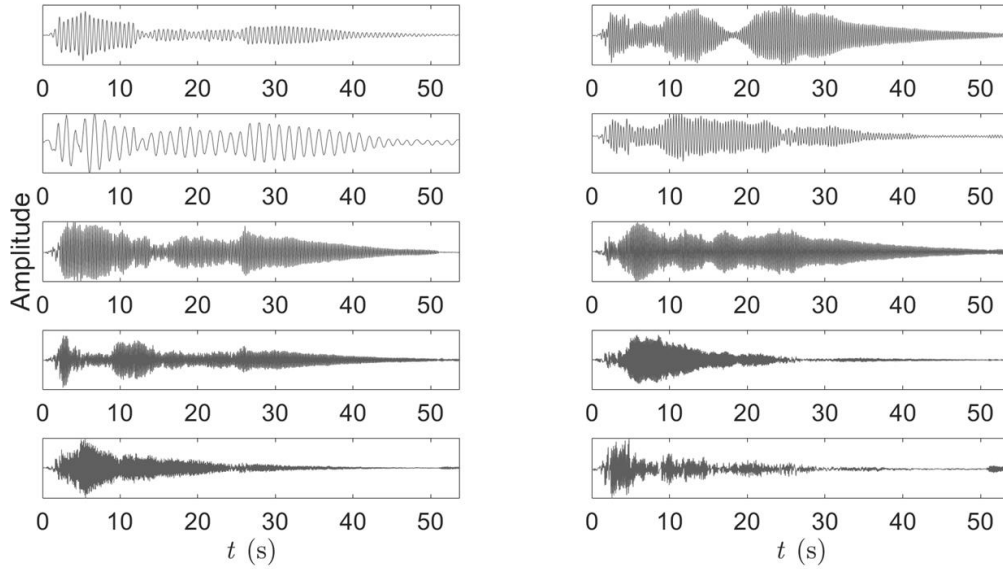
Figure 2.9: Modal response for the 10 DOF model forced by base excitation using $p = 10$.
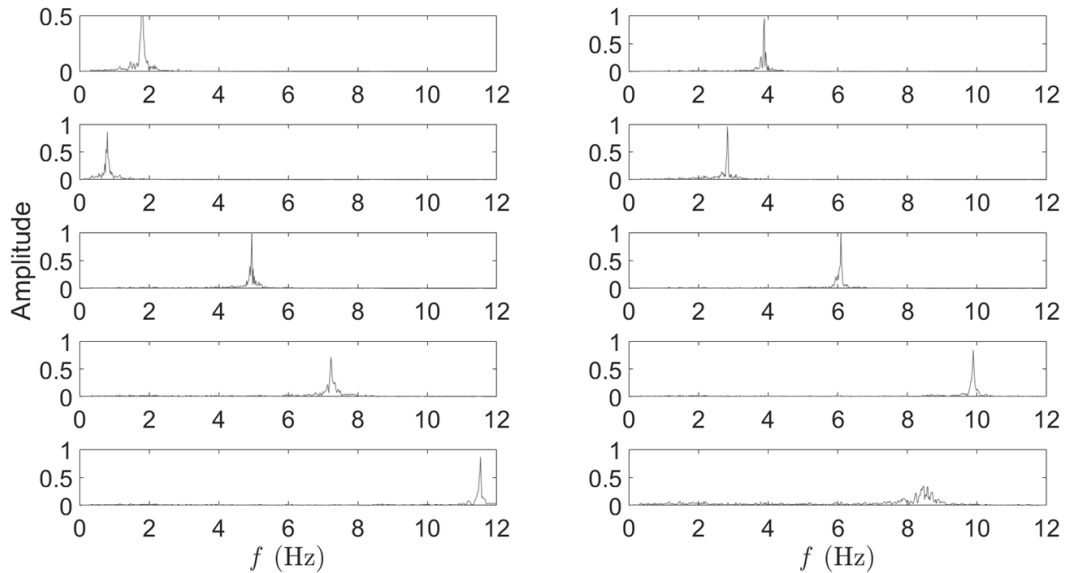
Figure 2.10: Fourier spectra of modal responses of the 10 DOF model (subjected to the base excitation) obtained from SOBI using $p = 10$.

Figures 2.11 and 2.12 show the modal response and Fourier spectra of the modal responses, respectively, using $p=100$.
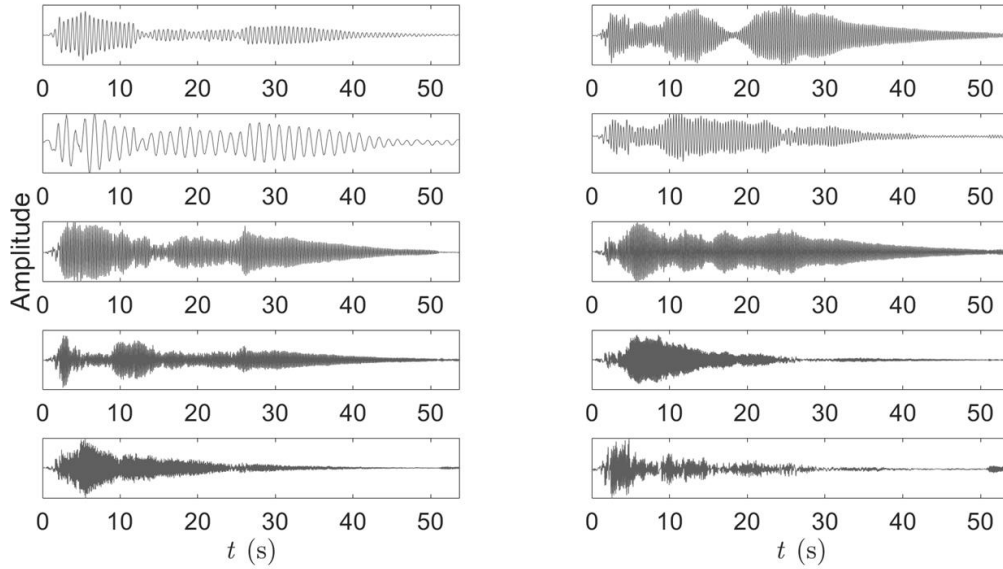
Figure 2.11: Modal response for the 10 DOF model forced by base excitation using $p = 100$.
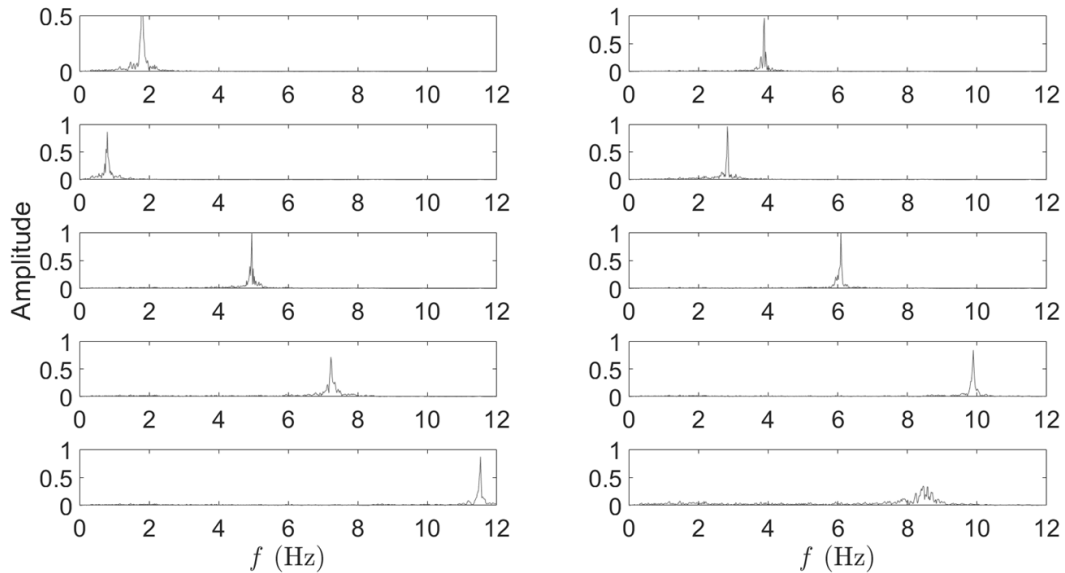
Figure 2.12: Fourier spectra of modal responses of the 10 DOF model (subjected to the base excitation) obtained from SOBI using $p = 100$.

The natural frequencies from most of the modal responses are separated from any other response, showing the efficiency and robustness of the SOBI method. The weakest response is that of eighth mode 8 (8.49 Hz), which contains some noise when using only one time-lagged covariance matrix. However, when using $p>10$ covariance matrices, the response of the eighth mode is nearly free from any visible noise. Autocorrelation of the modal responses is now performed to estimate the total damping ratio for each mode. Using the modal responses from applying one time-lagged covariance matrix, figure 2.13 shows the autocorrelation functions $R_x(\tau)$ and fitted curves for each mode.
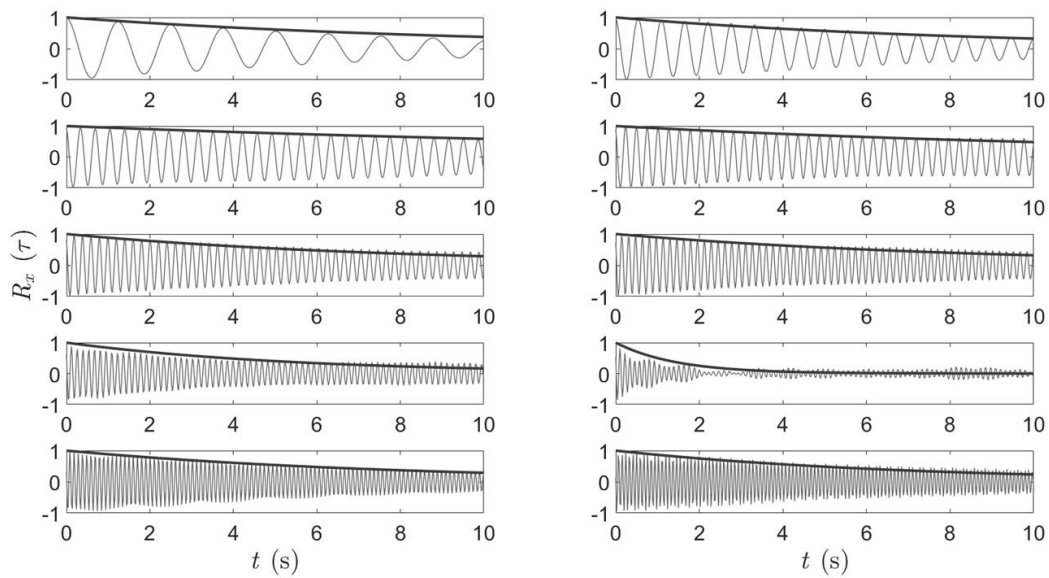
Figure 2.13: $R_x(\tau)$ **and the fitted decayed curves of all 10 modal responses obtained from SOBI using** $p = 1.$

Autocorrelation is again applied to the modal responses with 10 covariance matrices as shown in figure 2.14.
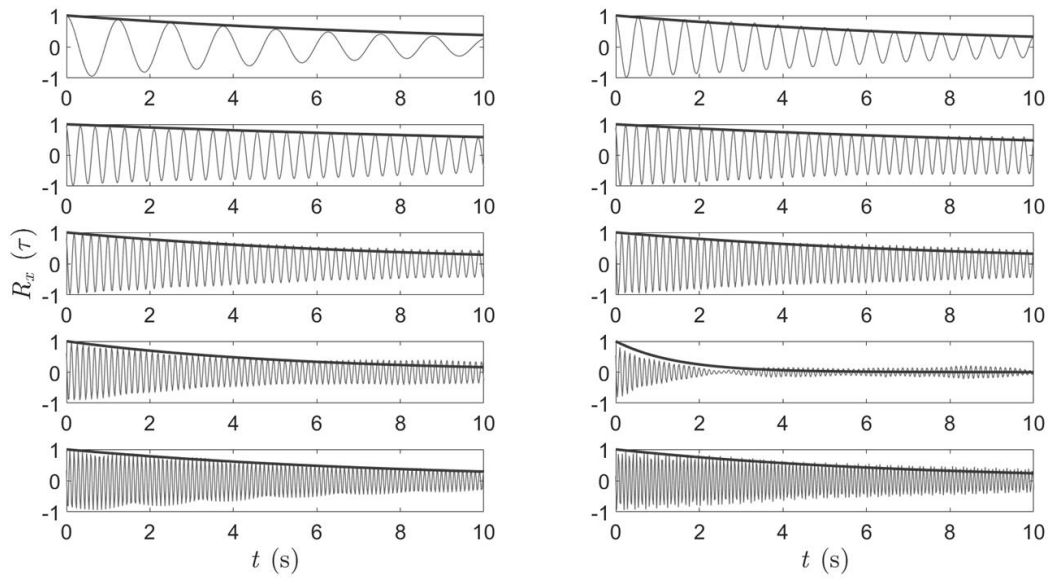
Figure 2.14: $R_x(\tau)$ **and fitted decayed curves for all 10 modal responses obtained from SOBI using** $p = 10$**.**

Mode 8 is noticeably less noisy, which also helps to estimate the damping more accurately. Autocorrelation is performed a final time on the modal responses using 100 time-lagged covariance matrices, shown in figure 2.15.
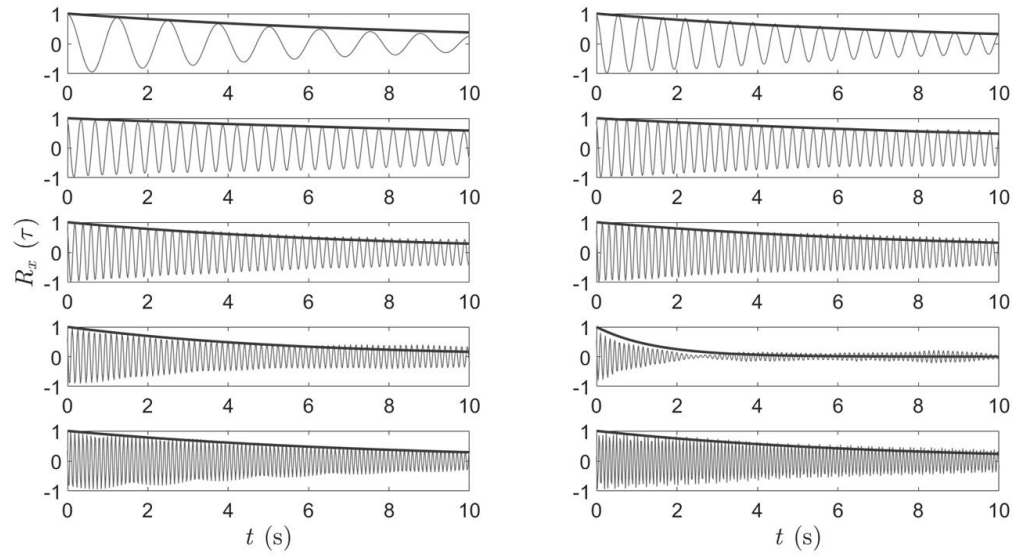
Figure 2.15: $R_x(\tau)$ **and fitted decayed curves for all 10 modal responses obtained from SOBI using** $p = 100$.

As expected, after analyzing the Fourier spectra of the modal responses, $R_x(\tau)$ using either 10 or 100 time-lagged covariance matrices is nearly identical. Table 2.3 shows the total damping ratio values, ζ_T, for each mode when using one, 10, or 100 of the covariance matrices.

Table 2.3: ζ_T **for all 10 modes, base excitation case.**

	ζ_T (%)		
Mode #	$p = 1$	$p = 10$	$p = 100$
1	2.0	2.0	2.0
2	1.0	1.0	1.0
3	0.3	0.3	0.3

4	0.3	0.3	0.3
5	0.4	0.4	0.4
6	0.3	0.3	0.3
7	0.4	0.4	0.4
8	1.2	1.3	1.3
9	0.2	0.2	0.2
10	0.2	0.2	0.2

The damping estimates from the modal responses are nearly identical, with the only difference being that of the eighth mode. The difference is most likely caused by the noise, meaning the amount of time-lagged covariance matrices have some influence on the damping estimates.

2.4.3   10 DOF Model with Random Excitation

The same 10 degree-of-freedom model will be used to apply a Gaussian random excitation at each degree of freedom to act as natural wind loads, instead of the base excitation. The wind force is generated as a Gaussian random sequence at each node, meaning the input influence matrix $\bar{\mathbf{B}}$ must be changed to accommodate the ten different inputs:

$$\bar{\mathbf{B}} = \begin{bmatrix} 0_{10x10} \\ \mathbf{M}^{-1} \end{bmatrix} \tag{2.19}$$

where M is the mass matrix. The simulated force has a total duration of 120 s and a sampling rate of 200 Hz. Figure 2.16 shows the responses of the model at each floor.
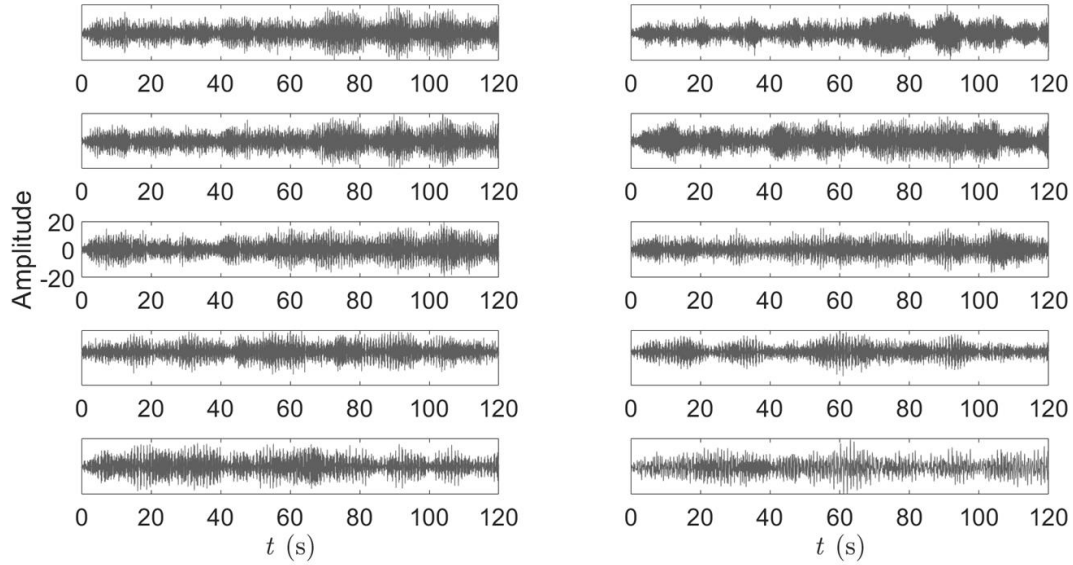
Figure 2.16: **Response of each floor for the 10 DOF model using Gaussian random excitation.**

SOBI is now applied to the response of the system, again using one, 10, and 100 time-lagged covariance matrices to determine if there are any differences in the modal responses. Figures 2.17 and 2.18 show the modal response and Fourier spectra of the modal responses, respectively, using one time-lagged covariance matrix.
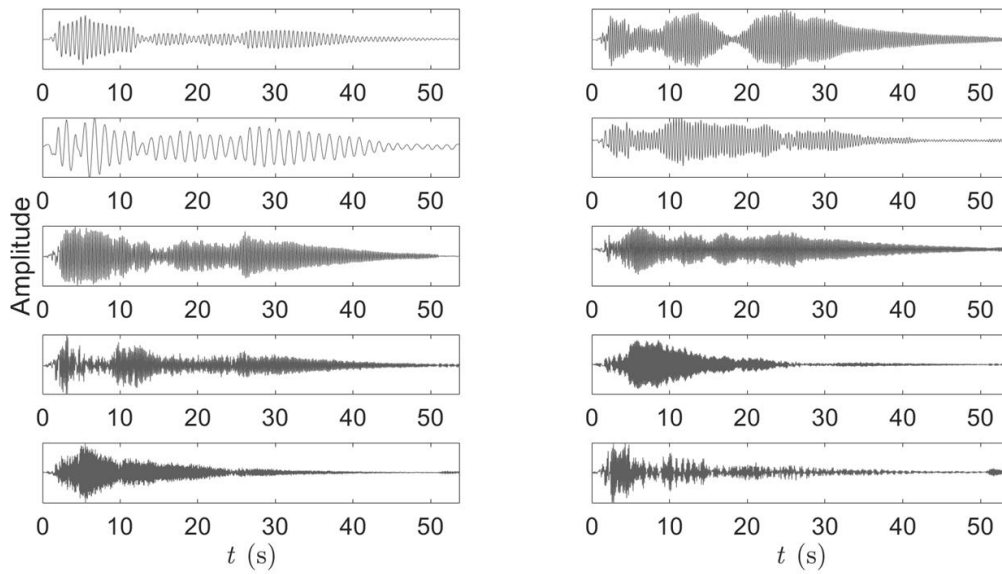
Figure 2.17: Modal response for the 10 DOF model forced by random excitation using p = 1.
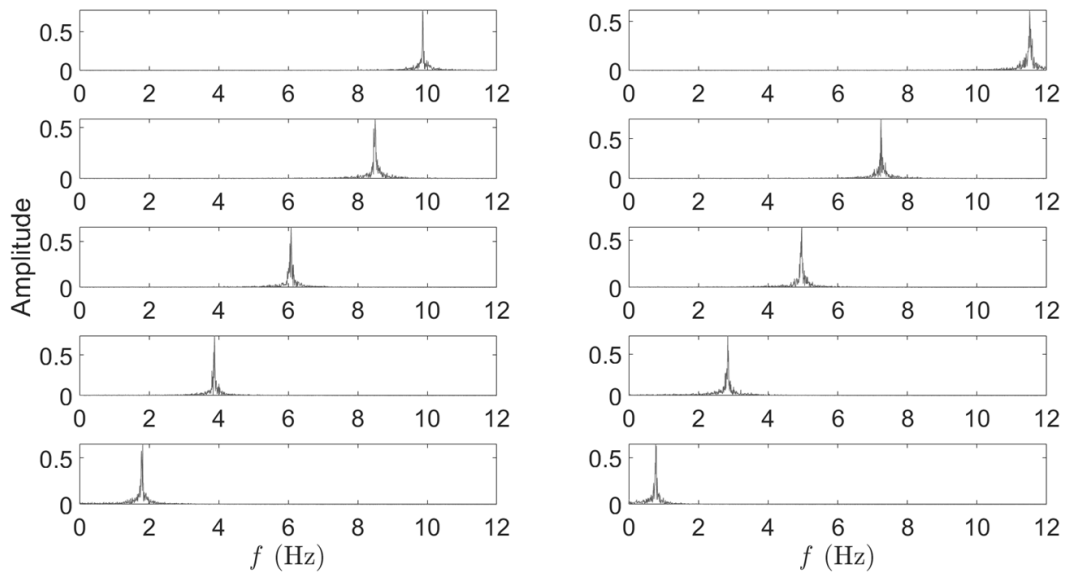
Figure 2.18: Fourier spectra of modal responses of the 10 DOF model (subjected to the random excitation) obtained from SOBI using p = 1.

Figures 2.19 and 2.20 show the modal response and Fourier spectra of the modal responses, respectively, using 10 time-lagged covariance matrices.
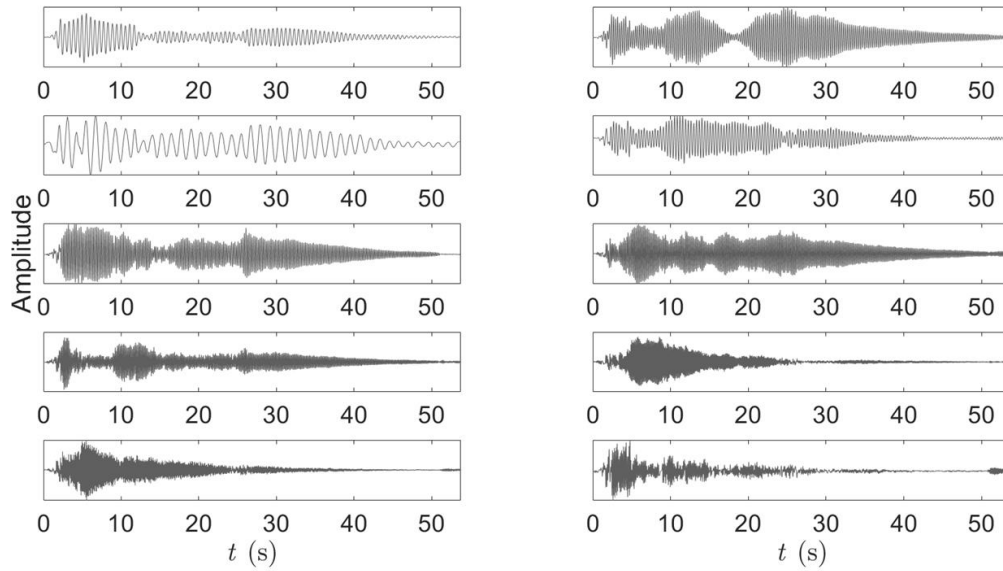
Figure 2.19: Modal response for the 10 DOF model forced by random excitation using $p = 10$.
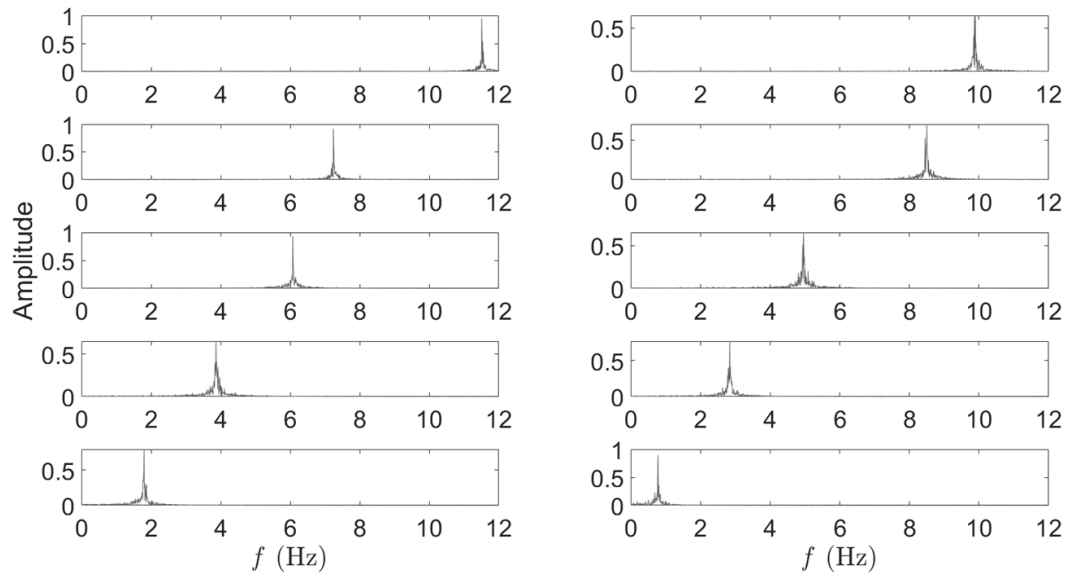
Figure 2.20: Fourier spectra of modal responses of the 10 DOF model (subjected to the random excitation) obtained from SOBI using $p = 10$.

Figures 2.21 and 2.22 show the modal response and Fourier spectra of the modal responses, respectively, using 100 time-lagged covariance matrices.
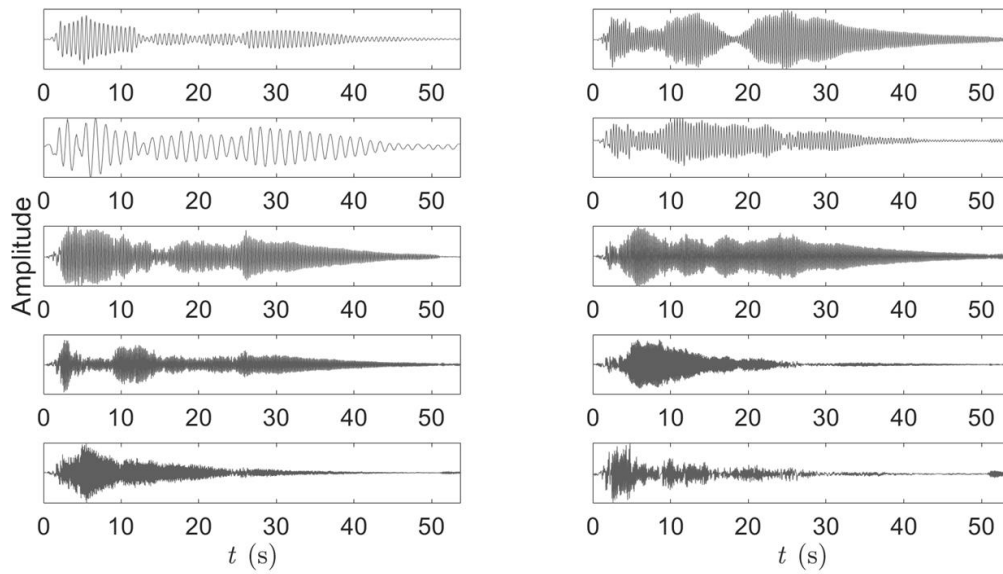
Figure 2.21: Modal response for the 10 DOF model forced by random excitation using $p =$ **100.**
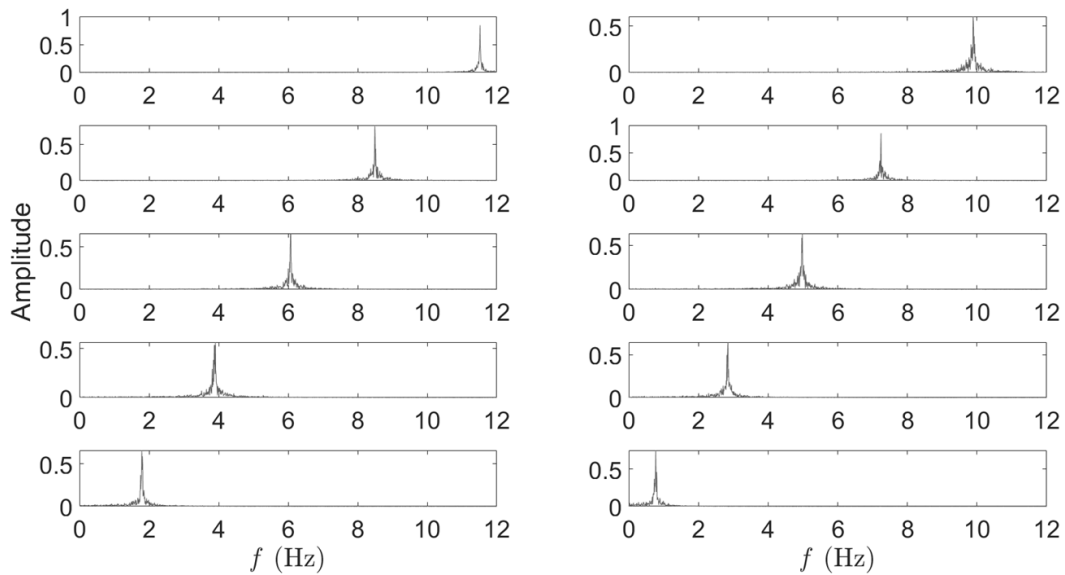
Figure 2.22: Fourier spectra of modal responses of the 10 DOF model (subjected to the base excitation) obtained from SOBI using $p = 100$.

Using either one, 10, or 100 time-lagged covariance matrices, SOBI is capable of separating the natural frequencies from any noise, as shown in the Fourier spectra plots. Unlike the base excitation example, all modes, including the eighth mode, show distinct peaks. Autocorrelation of the modal responses is now performed to estimate the total damping ratio for each mode. Using the modal responses from applying one time-lagged covariance matrix, figure 2.23 shows the autocorrelation functions $R_x(\tau)$ and fitted curves for each mode.
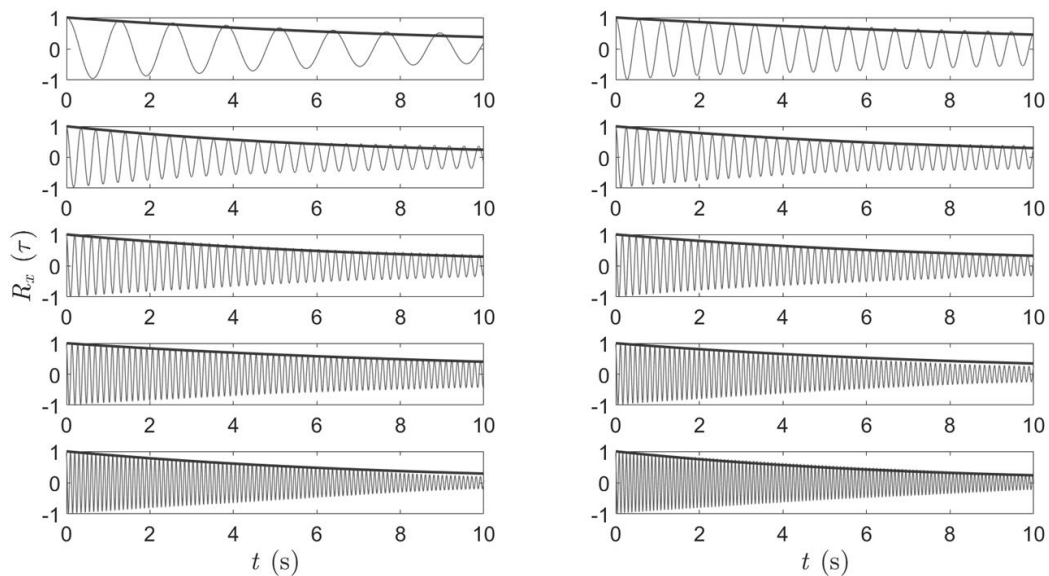
Figure 2.23: $R_x(\tau)$ and fitted decayed curves for all 10 modes, random excitation case, $p =$ 1.

Autocorrelation is again applied to the modal responses, this time when 10 time-lagged covariance matrices are used, as shown in figure 2.24.
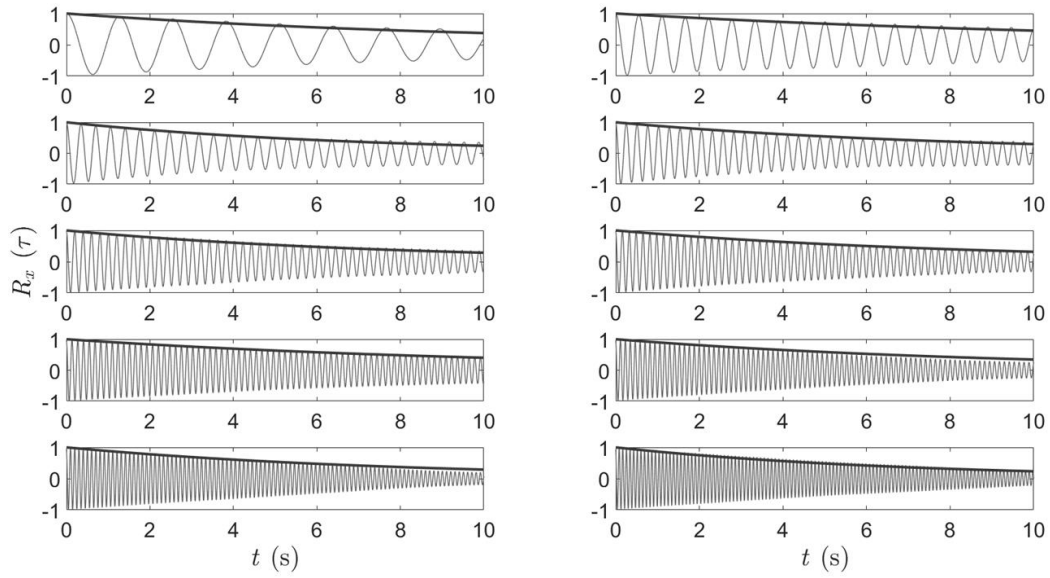
Figure 2.24: $R_x(\tau)$ **and fitted decayed curves for all 10 modes, random excitation case,** $p =$ **10.**

Autocorrelation is now applied to the modal responses, this time when 100 time-lagged covariance matrices are used, as shown in figure 2.25.
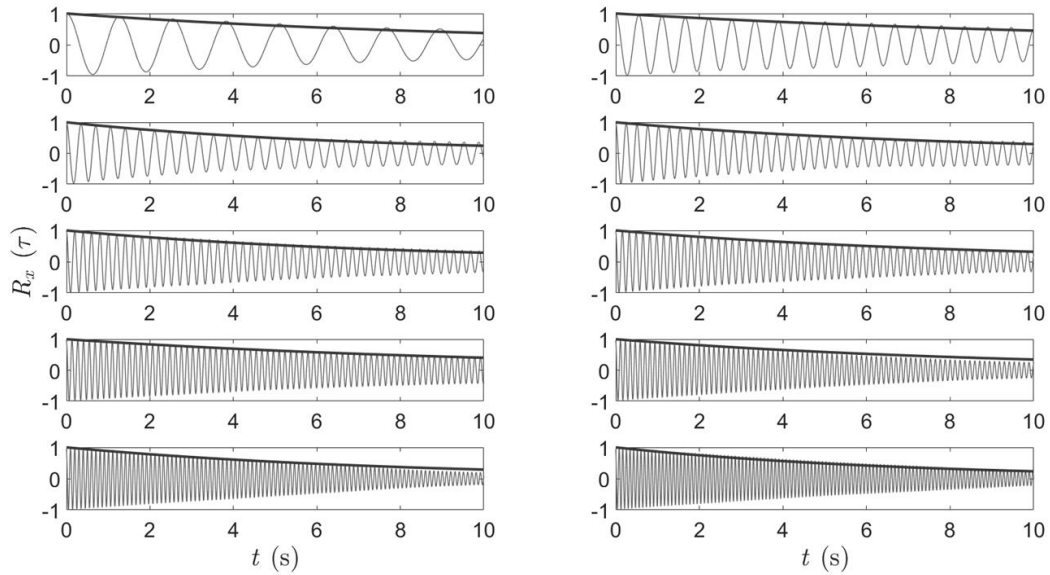
Figure 2.25: $R_x(\tau)$ **and fitted curves for all 10 modes, random excitation case,** $p = 100.$

Unlike the base excitation case, all total damping ratios are the same, no matter how many time-lagged covariance matrices are used for SOBI. Table 2.4 shows the total damping ratios estimated for each mode.

Table 2.4: ζ_T for all 10 modes for the random excitation case.

Mode #	1	2	3	4	5	6	7	8	9	10
ζ_T (%)	2.0	0.7	0.8	0.5	0.4	0.3	0.2	0.2	0.2	0.2

The ζ_T values for the Gaussian random excitation case are similar to the base excitation case; both cases have the highest damping in the first mode, and higher modes have low damping. The only difference is mode 8 in the base excitation case, where the damping was much larger than its random excitation counterpart, due to the noisy nature of the signal.

2.5 Summary

With its formulation complete, SOBI was used to determine the modal responses of three different scenarios. The first being a mixture of four sine waves obscured by white Gaussian noise, which SOBI was able to separate efficiently. The second example was a 10 DOF state-space model forced by a base excitation with the input being an earthquake time history load. This example showed the importance of selecting the appropriate *p*-value, as one mode in particular contained more noise than the other modes. The final example used the same 10 DOF model, forced by a Gaussian random load at each floor which acted as the natural wind. Autocorrelation was applied

to the modal responses for all three cases, and the damping ratio estimates seemed reasonable. Now that SOBI has been defined and tested, figure 2.26 shows a flowchart that shows the complete process of using SOBI on wind-induced response to estimate the damping.
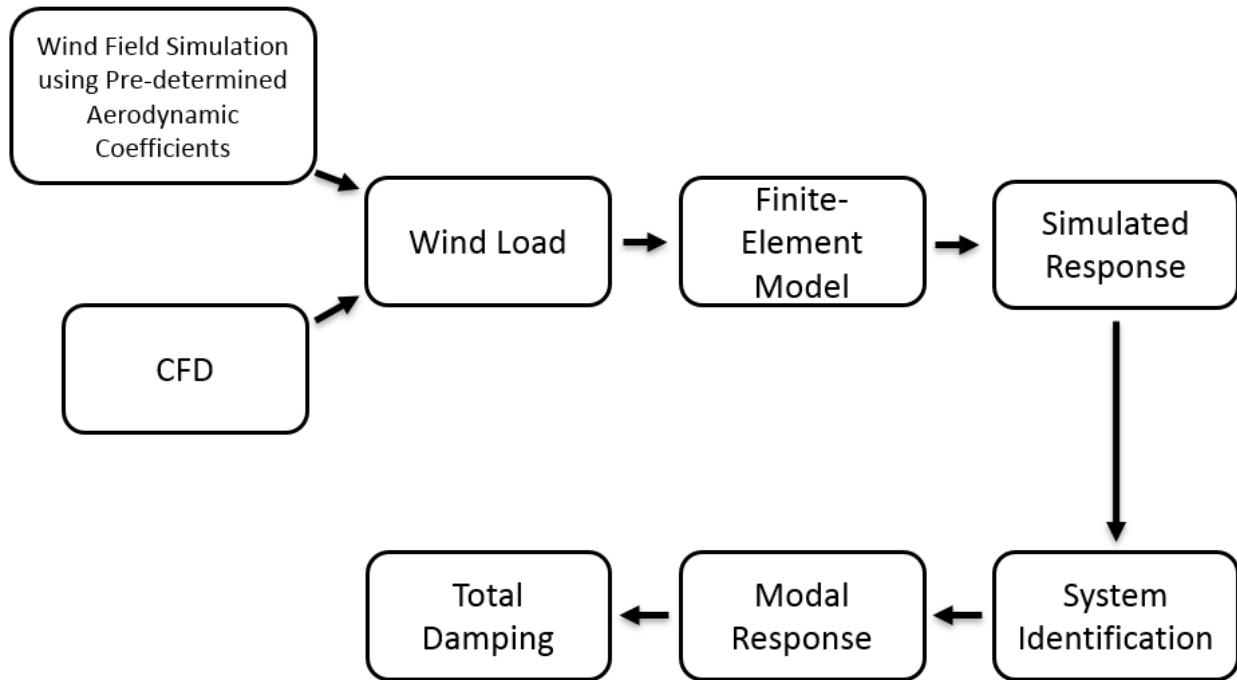
Figure 2.26: Flowchart showing the system identification process to estimate damping.

2.6   References

Belouchrani, A., Abed-Meraim, K., Cardoso, J., and Moulines, E. (1997). "A blind source separation technique using second-order statistics". *IEEE Transactions on Signal Processing,* 45, 434-444.

Cardoso, J.F. and Souloumiac, A. (1996). "Jacobi angles for simultaneous diagonalization". *SIAM Journal on Matrix Analysis and Applications,* 17, 1-3.

Hyvarinen, A. and Oja, E. (2000). "Independent component analysis: algorithms and applications", *Neural Networks,* 13, 411-430.

Jutten, C. and Herault, J. (1991). "Blind separation of sources, part I: an adaptive algorithm based on neuromimetic architecture". *Signal Processing,* 24, 1-10.

Musafere, F., Sadhu, A., and Liu, K. (2016). "Towards damage detection using blind source separation integrated with time-varying auto-regressive modeling". *Smart Materials and Structures,* 25, 015013.

Poncelet, F., Kerschen, G., Golinval, J.C., and Verhelst, D. (2007). "Output-only modal analysis using blind source separation techniques". *Mechanical Systems and Signal Processing,* 21, 2335-2358.

Sadhu, A., Narasimhan, S., and Antoni, J. (2017). "A review of output-only structural mode identification literature employing blind source separation". *Mechanical Systems and Signal Processing,* 94, 415-431.

Yuan, M., Sadhu, A., and Liu, K. (2017). "Condition assessment of structures with tuned mass dampers using empirical wavelet transform". *Journal of Vibration and Control,* 24(20), 4850-4867.

3 Simulation of Wind Forces

Estimation of aerodynamic damping of slender structures requires simulation of wind-induced response. In general, there are two popular wind force simulation techniques available in the literature: (a) Wind-field (WF) simulation with predefined pressure coefficients and (b) Computational Fluid Dynamics (CFD). The WF simulation characterizes a wind load with mean wind speed, increasing with height and with an additional fluctuating component that is acquired using a turbulence model associated with the predetermined pressure coefficients. The CFD simulation takes advantage of more accurate aerodynamics and Large Eddy Simulation (LES) to filter out smaller turbulent length scales. The wind forces from the WF simulation are obtained using the equations associated with predetermined drag and lift coefficients, while the forces from the CFD simulation are computed using the actual pressure coefficients.

3.1   Wind Field Simulation with Pre-defined Force Coefficients

To simulate the wind field, it is important to understand the behavior of wind itself and also how it interacts with structures. On the earth's surface, the wind is the movement of air and can be broken down into two main components: the mean velocity and the fluctuation. The mean wind velocity is often visualized as increasing exponentially with height (Singer, 1960; Wieringa, 1992), and is influenced by the roughness near the ground. Fluctuation is the second component that is fit overtop the mean velocity profile and is modeled as a spectrum, often using von Karman's wind turbulence model, outlined by Solari and Piccardo (2001). Wind may approach a structure from many different angles, but for this research, it is assumed the wind is perpendicular to the face of

the structure, known as "*along-wind*" direction. Once the wind strikes the face of the structure, it wraps around and applies a force at the sides; this is known as "*across-wind*" direction. By knowing the wind speed, the wind force may be calculated using a drag coefficient in the along-wind direction and a lift coefficient in the across-wind direction. The wind field is simulated using both along-wind and across-wind directions, while the wind force is determined using estimates for the drag and lift coefficients; it is these forces that are applied to the finite-element model.

In this thesis, the wind field is simulated as per Cheynet (2020). The wind simulation begins by selecting a total time series duration and sampling frequency, which are 1200 seconds and 20 Hz, respectively. The range of frequencies used in the von Karman spectrum begins at 1/1200 Hz, with the final frequency being the Nyquist frequency, taken as 10 Hz; the frequency range increases at increments of 1/1200 Hz. Next is the input of the mean wind data, which includes the standard deviations, turbulent length scales, and power-law information. The power law is as follows,

$$\bar{U} = U_{ref}\left(\frac{z}{z_{ref}}\right)^{\alpha} \tag{3.1}$$

where $\bar{U}$ is the mean wind speed in m/s, U_{ref} is the wind speed at reference height in m/s, z is the height in m, z_{ref} is the reference height in m, and α is the power-law coefficient. The power law is computed for U_{ref} values of 10, 20, and 30 m/s at a z_{ref} of 10 m and α of 0.15; it is assumed the mean wind speed in the across-wind direction is 0 m/s.

The generated wind field is three-dimensional, composed of a two-dimensional grid, as shown in figure 3.1, with the third dimension being time. The grid is generated by inputting the number of nodes along the Y and Z axes, as well as the minimum and maximum longitude and altitude. The chimney (the example structure used in this thesis as detailed in Chapter 4) is treated as a line-like

structure, with one node in the Y-axis and ten nodes in the Z-axis. The power law wind profile is applied at each node in the Z-axis.
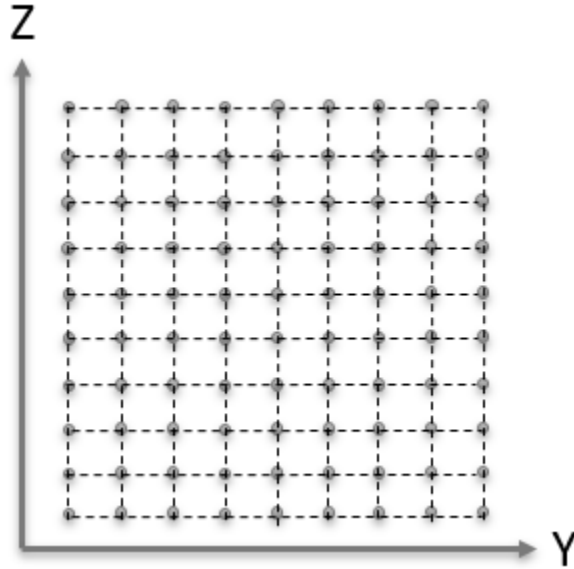
Figure 3.1: Simulated wind speed grid showing Y and Z axes.

The generation of the wind field is completed by using the von Karman mathematical model for the turbulence spectrum (Simiu and Scanlan, 1996):

$$S_u(z,f) = \sigma_u^2 \frac{4\frac{L_u}{\overline{U}}}{\left(1 + 70.7\left(f\frac{L_u}{\overline{U}}\right)^2\right)^{5/6}} \tag{3.2}$$

$$S_v(z,f) = \sigma_v^2 \frac{4\frac{L_v}{\overline{U}}\left(1 + 754\left(f\frac{L_v}{\overline{U}}\right)^2\right)}{\left(1 + 283\left(f\frac{L_v}{\overline{U}}\right)^2\right)^{11/6}} \tag{3.3}$$

where $\sigma_{u,v}^2$ is the variance of the wind speed, z is the height in m, U is the mean wind speed in m/s, f is the frequency in Hz, and $L_{u,v}$ is the turbulent length scale in m. The variance and turbulent

length scales are taken from the CFD simulation. Figures 3.2 and 3.3 show the simulated along-wind and across-wind spectra, respectively, compared to the theoretical mathematical model to demonstrate accuracy.
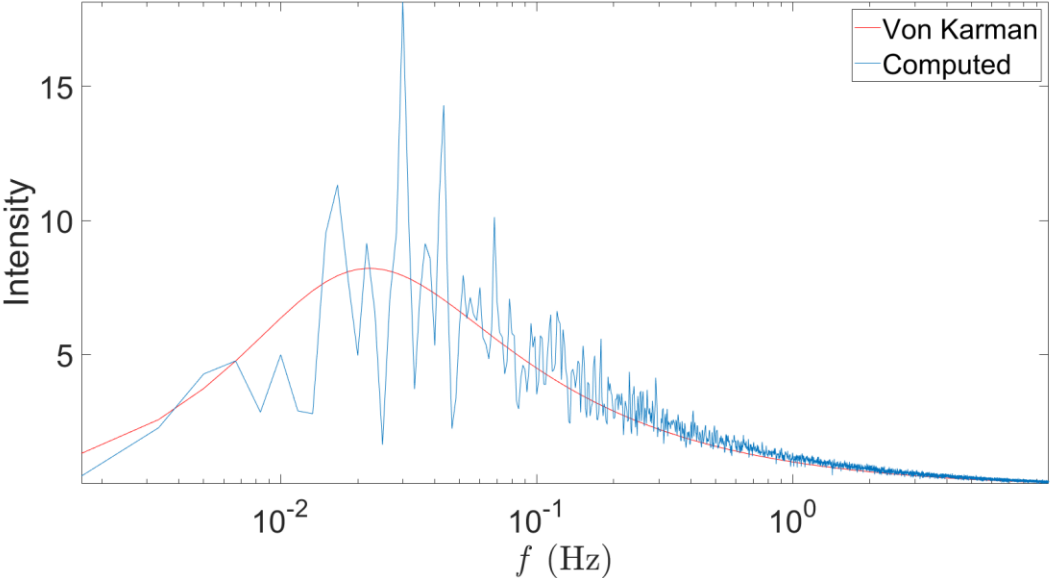
Figure 3.2: Simulated and theoretical spectrum, $\bar{U}$ = 30 m/s (along-wind).
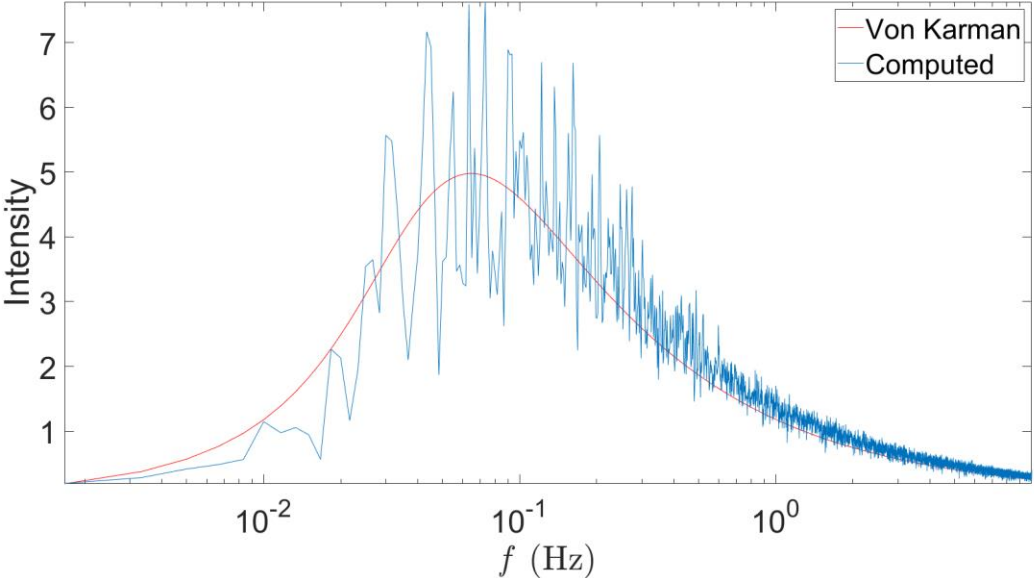
Figure 3.3: Simulated and theoretical spectrum, $\bar{U}$ = 30 m/s (across-wind).

Due to the existence of aerodynamic admittance, the von Karman spectrum is used to determine the cross-spectra at two points along the height of the chimney:

$$S_{u_1 u_2}(r, f) = \sqrt{S(z_1, f) S(z_2, f)} \, e^{-f_c} \tag{3.4}$$

where $S(z_1, f)$ and $S(z_2, f)$ are the von Karman spectra at two points, r is the distance between the two points, n is the frequency in Hz, and f_c is the coherence function. The coherence function is computed using,

$$f_c = \frac{2f \sqrt{C_z^2 (z_1 - z_2)^2 + C_y^2 (y_1 - y_2)^2}}{U(z_1) + U(z_2)} \tag{3.5}$$

where n is the frequency in Hz, $C_{y,z}$ are the decay coefficients, z_1, z_2, y_1, y_2 are the coordinates of points one and two, and $U(z_1)$ and $U(z_2)$ are the mean wind speeds at points one and two, respectively. The cross-spectra values are then arranged in a matrix which is decomposed using Cholesky factorization. Finally, the time series of the wind field is generated using a Monte Carlo simulation of φ, proposed by (Shinozuka, 1972),

$$u' = \sqrt{2 * df} \, |\mathbf{S}| \cos(2\pi f t + \phi) \tag{3.6}$$

where df is the frequency range increment, $\mathbf{S}$ is the factorized spectral matrix, f is the frequency in Hz, and ϕ is the phase angle. Figures 3.4 and 3.5 show the time series for the along-wind and across-wind directions for a mean wind speed of 30 m/s at the reference height (100 m), respectively.
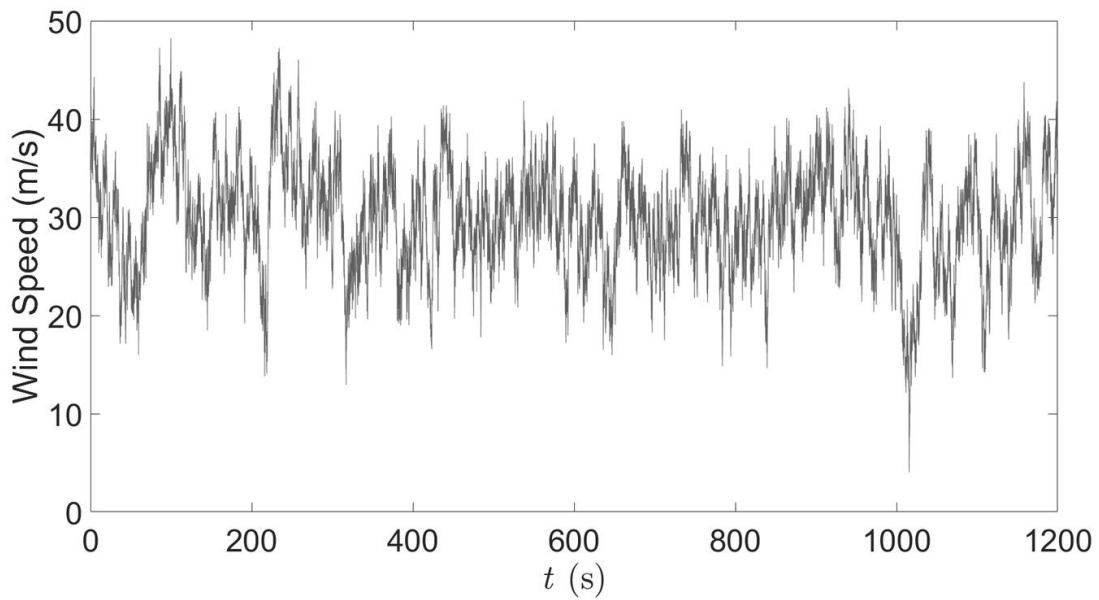
Figure 3.4: Along-wind time series for $\overline{U}$ = 30 m/s at 100 m height using pre-determined aerodynamic coefficients.
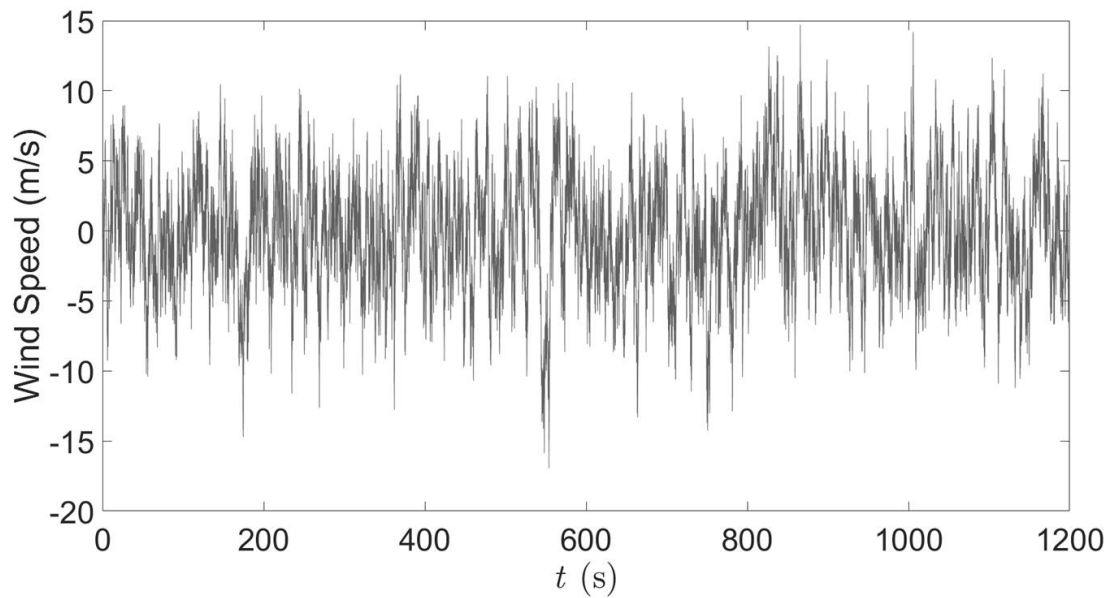
Figure 3.5: Across-wind time series for $\overline{U}$ = 0 m/s at 100 m height using pre-determined aerodynamic coefficients.

The time series of the wind speed is converted into a force using the drag equation:

$$F_x = \frac{1}{2}\rho C_D A[\bar{U}(z)^2 + 2\bar{U}u'(z,t)] \tag{3.7}$$

$$F_y = \rho C_L A\bar{U}(z)v'(z,t) \tag{3.8}$$

where F_x is the along-wind force in N, F_y is the across-wind force in N, ρ is the air density in kg/m³, C_D is the drag coefficient, C_L is the lift coefficient, A is the area in m³, $\bar{U}(z)$ is the mean wind speed in m/s, $u'(z,t)$ is the along-wind fluctuation in m/s, and $v'(z,t)$ is the across-wind fluctuation in m/s.

3.2 Computational Fluid Dynamics Model

Computational fluid dynamics (CFD) uses numerical analysis to solve problems involving the flow of wind around a structure. Unlike the simplistic WF model, a CFD model may be used to determine wind pressure on the study structure (Dagnew and Bitsuamlak 2013). CFD models are located within a domain determined by the user, which encompasses the wind field. The domain must be large enough to ensure adequate space for any aerodynamic effects, including vortex shedding of the wake downstream of the model (Dagnew and Bitsuamlak 2013, Aboshosha *et al.* 2015). To achieve the desired accuracy, it is important to select an optimum mesh size for the discretization despite its trade-off with the computational time. If the mesh is too large, it will not accurately capture the aerodynamic effects, while a small mesh will require extreme computational time. Typically, the mesh closest to the structure will be finer, with the mesh size gradually increasing away from the structure. This ensures the observed aerodynamic effects and pressure

distributions are accurate while reducing the computation time. Figure 3.6 shows an example of a domain subdivided into zones that user may input different mesh sizes. Figure 3.7 shows the wind flow in a CFD model in both profile and top-down view.
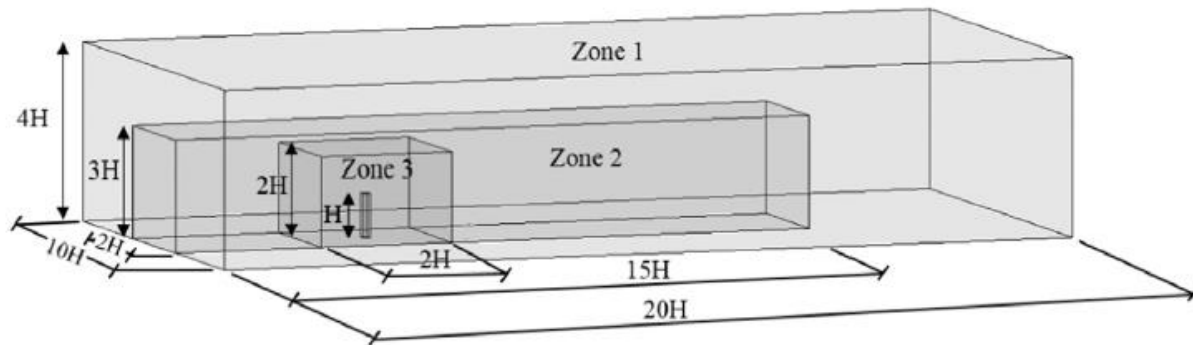
Figure 3.6: Domain with different mesh zone (Aboshosha *et al.* (2015)).
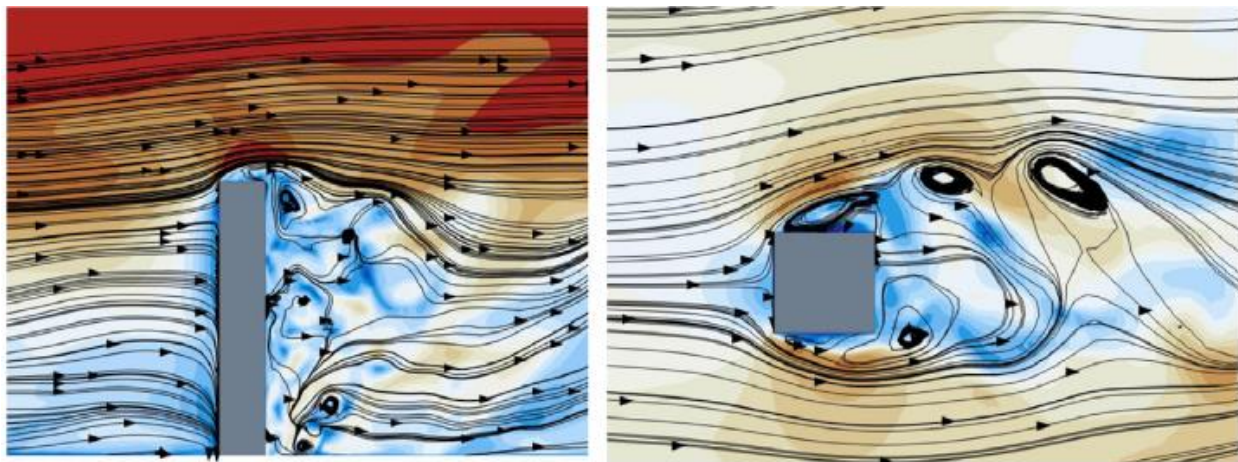
Figure 3.7: Wind field within the CFD model showing profile and top-down views of a square cross-section structure (Aboshosha *et al.* 2015).

The pressure distribution on the surface of a structure is a common output from a CFD model. Montazeri and Blocken (2013) used a CFD model to determine the pressure coefficients on buildings with and without balconies. Their methods involved a Reynolds-Averaged Navier-

Stokes simulation, which resulted in low measurement error when compared to the pressure coefficients determined from wind-tunnel measurements. Jiang *et al*. (2003) used CFD, combined with LES, to determine the pressures along surfaces during natural ventilation. Using three different ventilation cases, it was determined that using large-eddy simulation resulted in good agreement with the experimental data. Tominaga *et al*. (2008) analyzed pedestrian wind environments around buildings using CFD models. Seven experiments were performed to determine the differences between CFD, wind tunnel, and field measurements. The research performed was following guidelines outlined by the Working Group of the Architectural Institute of Japan. *Lim et al*. (2009) used a CFD model to investigate the flow around a cube within a turbulent wind field. Using large-eddy simulation methods, the researchers were able to determine the mean and fluctuating pressures on the surface of the cube, with similar uncertainty when compared to wind-tunnel experiments. Daniels *et al*. (2013) used an innovative inflow generation technique using CFD to determine fluctuating pressures on tall buildings. The researchers were able to analyze the pressure coefficients using different turbulence intensities and integral length scales. Tamura (2008) reviewed CFD and large-eddy simulation methods for several different wind engineering studies, including wind-resistant building design, turbulence structures, and aerodynamics in urban areas. Due to the complexity of wind in a real-life setting, Tamura (2008) stressed the importance of comparing CFD results to full-scale measurements to determine the accuracy of the CFD model.

CFD is a technique to analyze the aerodynamics of wind when it interacts with a structure. CFD is also used to find the pressures acting on the structure which can be used to find the wind loading in along-wind and across-wind directions. LES is a method used in CFD to reduce the computational time by filtering out the eddies associated with smaller turbulent length scales.

56

Dagnew and Bitsuamlak (2012) provided a review of state-of-the-art CFD methods combined with LES. Small-scale turbulence lengths are determined and filtered using Navier-Stokes equations and a sub-grid-scale model. The paper also describes the appropriate dimensions of the CFD domain to ensure appropriate room for vortex shedding and the wake. Merrick and Bitsuamlak (2008) combined wind tunnel testing with an LES model to determine the wind flow around cylinders with rough surfaces. The CFD domain was modeled after the boundary-layer wind tunnel used for the experiments, and with varying sub-critical and super-critical Reynolds numbers. It was concluded that the roughness elements were capable of producing super-critical flow parameters at sub-critical Reynolds numbers. Huang *et al.* (2010) developed a turbulence generator based on the random flow generation technique to be used with LES. The technique was able to generate a turbulent flow which satisfied any given spectrum and was also compared to Smirnov's random flow generation technique. The generator also agreed well with wind tunnel tests and satisfied the divergence-free condition. Aboshosha *et al.* (2015) introduced a turbulent inflow generator to be used as an inflow boundary condition for LES of tall buildings. The generator is compared with other flow conditions found in the previous literature and existing wind tunnel test data of tall buildings. The proposed LES method showed a good agreement with wind tunnel tests by comparing the acceleration responses. Aboshosha *et al.* (2015) also used LES to determine the atmospheric boundary layer flow with rough terrains modeled by fractal surfaces. Three different rough surfaces were generated for the LES model, which were countryside, suburban, and urban terrain. The mean and fluctuating velocity profiles were compared with engineering design guides, which showed excellent agreement. Elshaer *et al.* (2016) used LES to determine the aerodynamic response of tall buildings in both isolated and surrounded configurations. The particular LES method used for the study was the consistent discrete random

flow generation technique, which has accurately determined turbulence spectra in the past. In both isolated and surrounded configurations, LES was able to accurately determine the pressures on the structure; the pressures were compared to wind tunnel tests, showing a small amount of error. For this research, the main objective of the CFD model is to find the forces acting on a structure using different wind fields. The output of the CFD model typically provides force coefficients on the surface of the structure, in both along-wind and across-wind directions.

A computational fluid dynamics (CFD) model of a slender structure (e.g., a chimney), matching the finite-element model used in the next chapter, is built to generate force coefficients and generate the wind force. Figure 3.8 shows the chimney within the domain and figure 3.9 shows an unobstructed view of the chimney without the domain.
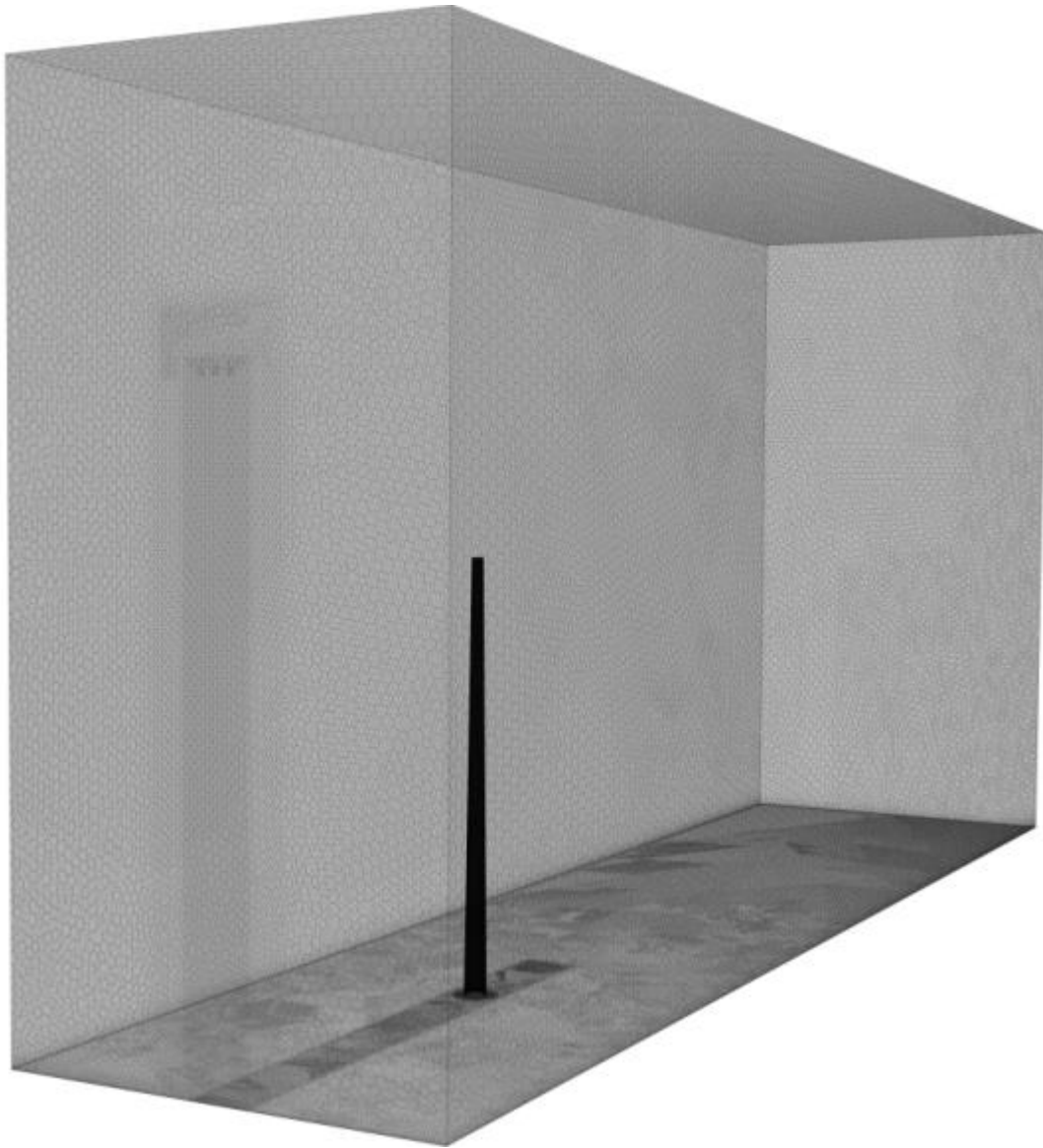
Figure 3.8: CFD chimney model within the domain.
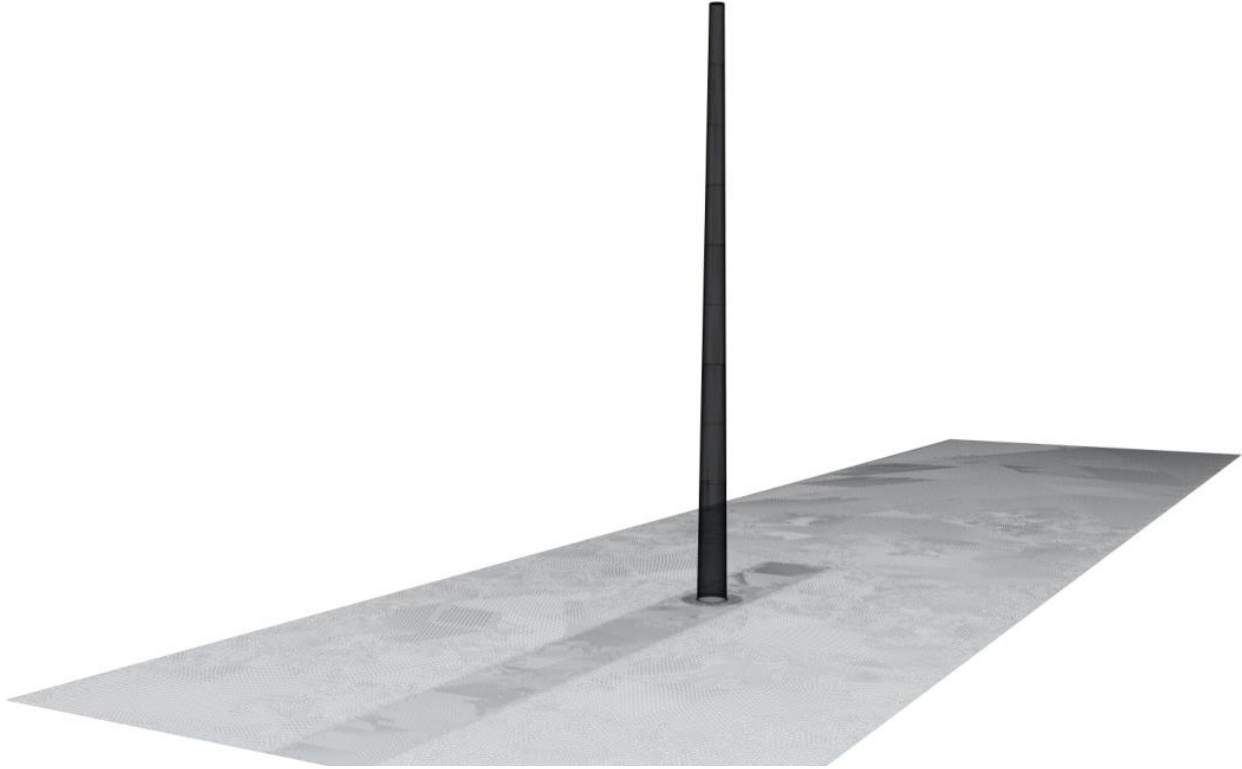
Figure 3.9: CFD chimney model outside of the domain.

The domain is broken down into three different meshing zones; figure 3.10 shows the three meshing zones relative to the chimney model, and table 3.1 lists the dimensions of the meshing zones as well as the mesh size.
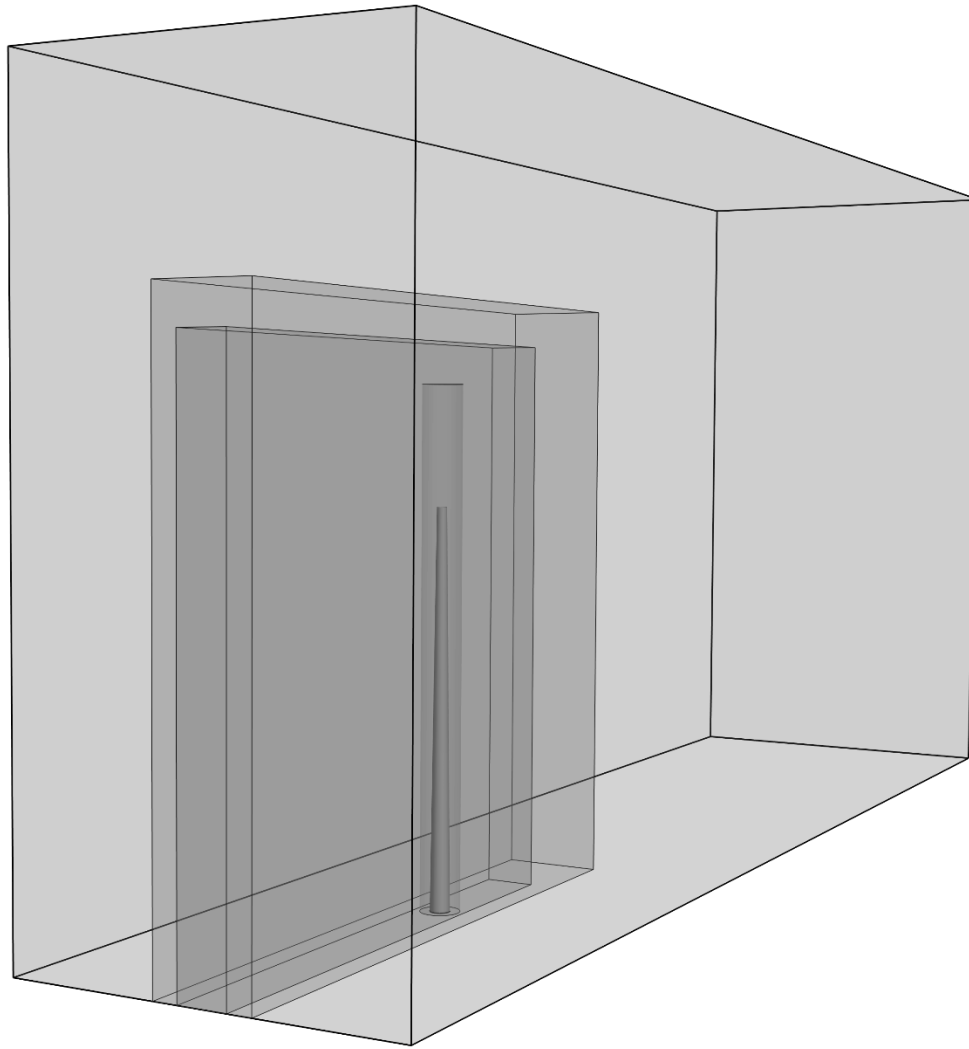
Figure 3.10: CFD chimney model with three meshing zones.

Table 3.1: CFD meshing zone dimensions.

Zone	Length (m)	Width (m)	Height (m)	Mesh Size (m³)
1	137.5	12.5	130	0.156

2	162.5	25	140	0.313
3	400	100	150	0.625

Similar to the WF simulation, $\bar{U}$ of 10, 20, and 30 m/s are used at the chimney height of 100 m, with turbulence added on using a von Karman spectrum. Each wind speed case uses a different sampling frequency; higher sampling rates are used for more turbulent wind cases to ensure the turbulence is accurately captured. However, since the amount of output force coefficients do not change, this means the duration of the wind simulation will change for each mean wind speed case. Table 3.2 shows the corresponding sampling rate and total simulation time for each mean wind speed case.

Table 3.2: CFD sampling rates and simulation times for different values of $\bar{U}$.

$\bar{U}$ (m/s)	Sampling Rate (Hz)	Total Simulation Time (s)
10	66.67	120
20	133.33	60
30	200	40

Figure 3.11 shows a profile view of the chimney and the wake in the along-wind direction, while figure 3.12 shows a top-down view of the wake.

Velocity: Magnitude (m/s)

0.00   8.00   16.0   24.0   32.0   40.0
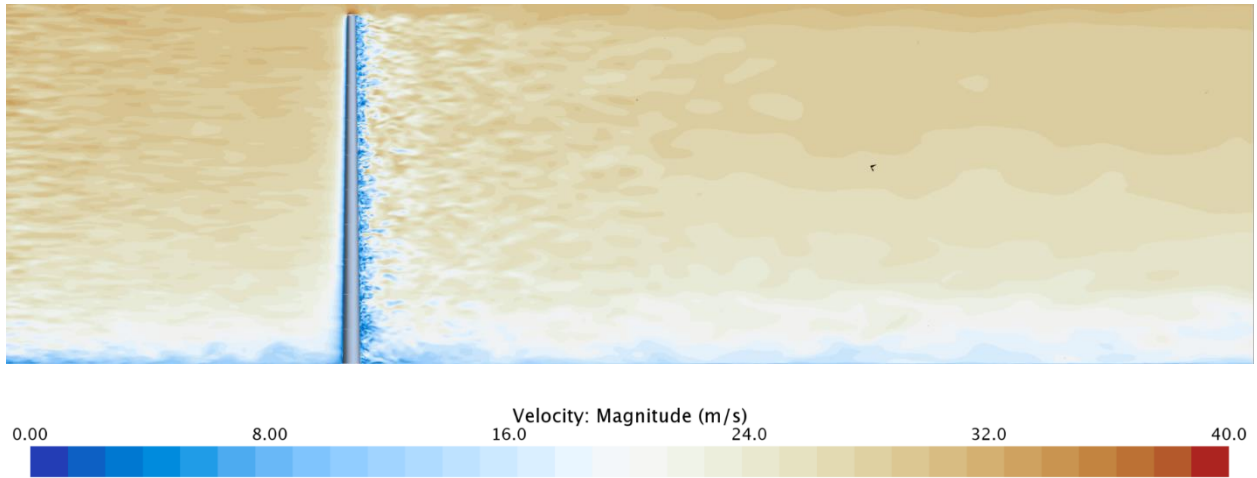
Figure 3.11: Profile view of the CFD chimney model and wake in along-wind direction.

Velocity: Magnitude (m/s)

0.00   8.00   16.0   24.0   32.0   40.0
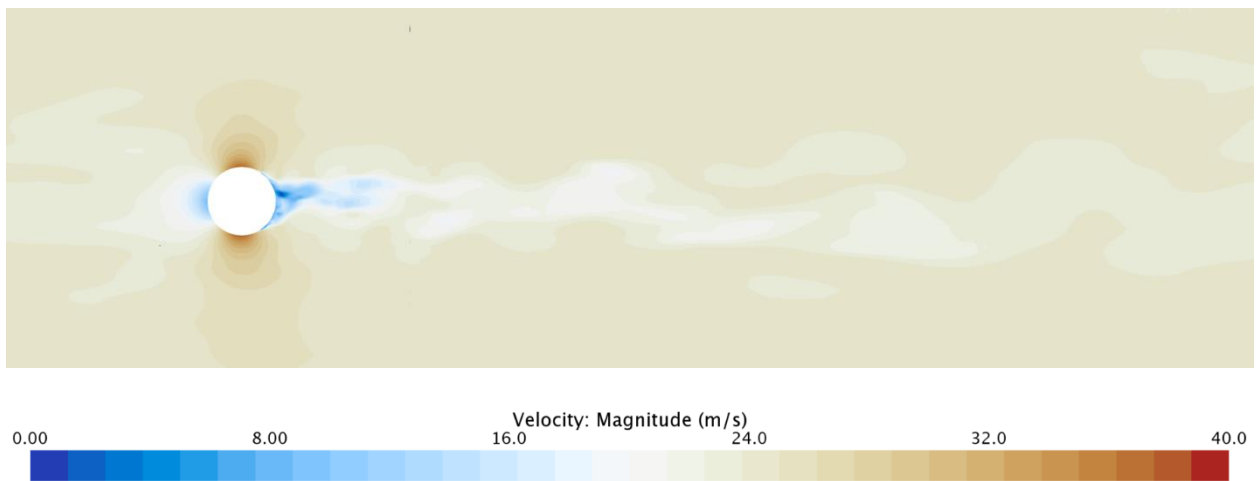
Figure 3.12: Top-down view of the CFD chimney model and wake.

The chimney is divided into ten sections along its height to obtain force coefficients at different elevations. Therefore, wind forces are acquired at the ten different levels and are applied onto the finite-element model as shown in the next chapter. Using the force coefficients, the wind force is computed using the following expression

$$F_x = \frac{1}{2}\rho C_{Fx} U_{100m}^2 h d \qquad (3.9)$$

where C_{Fx} is the force coefficient, F_x is the force in N, ρ is the air density in kg/m³, U_{100m}^2 is the reference wind speed at a height of 100 m, h is the height of the chimney in m, and d is the diameter of the chimney at mid-height in m. Equation (3.9) also applies to F_y which is the across-wind force, where the force coefficient would be C_{Fy}. After having multiplied each force coefficient equation, the wind forces are assembled into a time series which is applied onto the finite-element chimney model. Figure 3.13 shows the along-wind and across-wind force coefficients for both the WF and CFD simulations at $z = 100$ m.
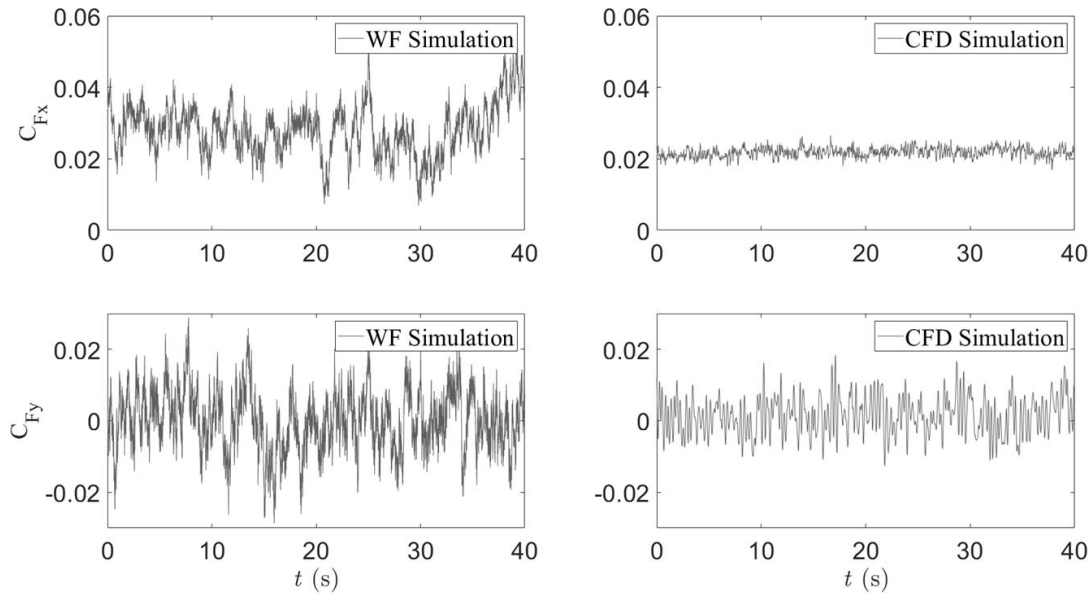
Figure 3.13: C_{Fx} **and** C_{Fy} **values for both WF and CFD simulations at z = 100 m.**

3.3 References

Aboshosa, H., Bitsuamlak, G., and El Damatty, A. (2015). "LES of ABL flow in the built-environment using roughness modeled by fractal surfaces". *Sustainable Cities and Society,* 19, 46-60.

Aboshosha, H., Elshaer, A., Bitsuamlak, G., and El Damatty, A. (2015). "Consistent inflow turbulence generator for LES evaluation of wind-induced responses for tall buildings". *Journal of Wind Engineering and Industrial Aerodynamics,* 142, 198-216.

Ashok, J., Charles, S., and Umarani, C. (2018). "Comparative study on the evaluation of wind load on buildings using computational fluid dynamics and IS: 875(Part-3)". *Asian Journal of Engineering and Applied Technology,* 7, 16-18.

Cheynet, E. (2020). Wind field simulation (the user-friendly version) (https://www.mathworks.com/matlabcentral/fileexchange/50041-wind-field-simulation-the-user-friendly-version), MATLAB Central File Exchange. Retrieved April 11, 2020.

Dagnew, A. and Bitsuamlak, G. (2013). "Computational evaluation of wind loads on buildings: a review". *Wind and Structures,* 16, 629-660.

Daniels, S, J., Castro, I. P., and Xie, Z.T. (2013). "Peak loading and surface pressure fluctuations of a tall model building". *Journal of Wind Engineering and Industrial Aerodynamics,* 120, 19-28.

Elshaer, A., Aboshosha, H., Bitsuamlak, G., and El Damatty, A. (2016). "LES evaluation of wind-induced responses for an isolated and a surrounded tall building". *Engineering Structures,* 115, 179-195.

Huang, S.H., Li, Q.S., and Wu, J.R. (2010). "A general inflow turbulence generator for large-eddy simulation". *Journal of Wind Engineering and Industrial Aerodynamics,* 98, 600-617.

Jiang, Y., Alexander, D., Jenkins, H., Arthur, R., and Chen, Q. (2003). "Natural ventilation in buildings: measurement in a wind tunnel and numerical simulation with large-eddy simulation". *Journal of Wind Engineering and Industrial Aerodynamics,* 91, 331-353.

Lim, H. C., Thomas, T. G., and Castro, I. P. (2009). "Flow around a cube in a turbulent boundary layer: LES and experiment". *Journal of Wind Engineering and Industrial Aerodynamics,* 97, 96-109.

Merrick, R.J. and Bitsuamlak, G. (2008). "Control of flow around a circular cylinder by the use of surface roughness: a computational and experimental approach". *www.semanticscholar.org*

Montazeri, H. and Blocken, B. (2013). "CFD simulation of wind-induced pressure coefficients on buildings with and without balconies: Validation and sensitivity analysis". *Building and Environment,* 60, 137-149.

National Research Council of Italy (2010). "Guide for the assessment of wind actions and effects on structures". *CNR – Advisory Committee on Technical Recommendations for Structures,* CNR-DT 207/2008.

Shinozuka, M. (1972). "Digital simulation of random processes and its applications". *Journal of Sound and Vibration,* 25, 111-128.

Simiu E, Scalan R. Wind Effects on Structures. John Wiley and Sons Inc., 1996.

Singer, I.A. (1960) "A study of the wind profile in the lowest 400 feet of the atmosphere". *Prog. Report No. 5,* Brookhaven National Laboratory.

Solari, G. and Piccardo, G. (2001) "Probabilistic 3-D turbulence modeling for gust buffeting of structures". *Probabilistic Engineering Mechanics,* 16, 73-86.

Tamura, T. (2008). "Towards practical use of LES in wind engineering". *Journal of Wind Engineering and Industrial Aerodynamics,* 96-1451-1471.

Toja-Silva, F., Kono, T., Peralta, C., Lopez-Garcia, O., and Chen, J. (2018). "A review of computational fluid dynamics (CFD) simulations of the wind flow around buildings for urban wind energy exploitation". *Journal of Wind Engineering and Industrial Aerodynamics,* 180, 66-87.

Tominaga, Y., Mochida, A., Yoshie, R., Kataoka, H., Nozu, T., Yoshikawa, M., and Shirasawa, T. (2008). "AIJ guidelines for practical applications of CFD to pedestrian wind environment around buildings". *Journal of Wind Engineering and Industrial Aerodynamics,* 96, 1749-1761.

Wieringa, J. (1992). "Updating the Davenport roughness classification", *Journal of Wind Engineering and Industrial Aerodynamics,* 41, 357-368.

4 Finite-element Modeling

A finite element (FE) model, developed in SAP2000 structural analysis software, is used to demonstrate the robustness of SOBI to estimate the aerodynamic damping. The model is designed as a slender structure (e.g., chimney) to ensure a sufficient number of modes are excited due to low-frequency wind excitation. Both WF and CFD simulated wind forces (obtained from Chapter 3) are applied to the FE model to determine any differences between the estimates of total damping of the model subjected to two different nature of wind simulation. The structural damping of the system is determined using simulated free vibration data. Finally, aerodynamic damping is estimated by taking the difference between the estimated total and structural damping of the FE model.

4.1 Properties of the FE Model

The structure considered is a reinforced concrete chimney that follows a similar design by Hernandez et al. (2012), using SAP2000 as shown in figure 4.1. The chimney has a height of 100 m, a thickness of 0.305 m, a bottom diameter of 5 m, and a top diameter of 2.5 m. The concrete has a compressive strength of 28 MPa, and Young's Modulus of 23.8 GPa, a Poisson's ratio of 0.15, and a unit weight of 2400 kg/m^3. The chimney is constructed around a radial grid, composed of 24 nodes, using bar elements that run the height of the structure; the base of the chimney is fixed in all directions. The model is divided into ten equal sections along the height, where each bar element is 10 m long. These bar elements are extruded into areas to form the circumference of the structure, which are then extruded into solids to reflect the desired thickness of the chimney. The model is meshed using an automatic solid meshing system in SAP2000, which divides each solid

element into three sections. Therefore, since there are 24 solid sections along the radius, and ten solid sections along the height, the mesh divides the chimney into 720 sections. The modal damping ratios are also set for the SAP2000 model, following Kareem and Gurley (1996), who indicate that damping is proportional to stiffness which increases in higher modes. The modal damping ratios are shown in Table 4.1.

Table 4.1: The first four modal damping ratios of the chimney model.

Mode #	Modal Damping Ratio (%)
1	2.0
2	5.0
3	8.5
4	15.0
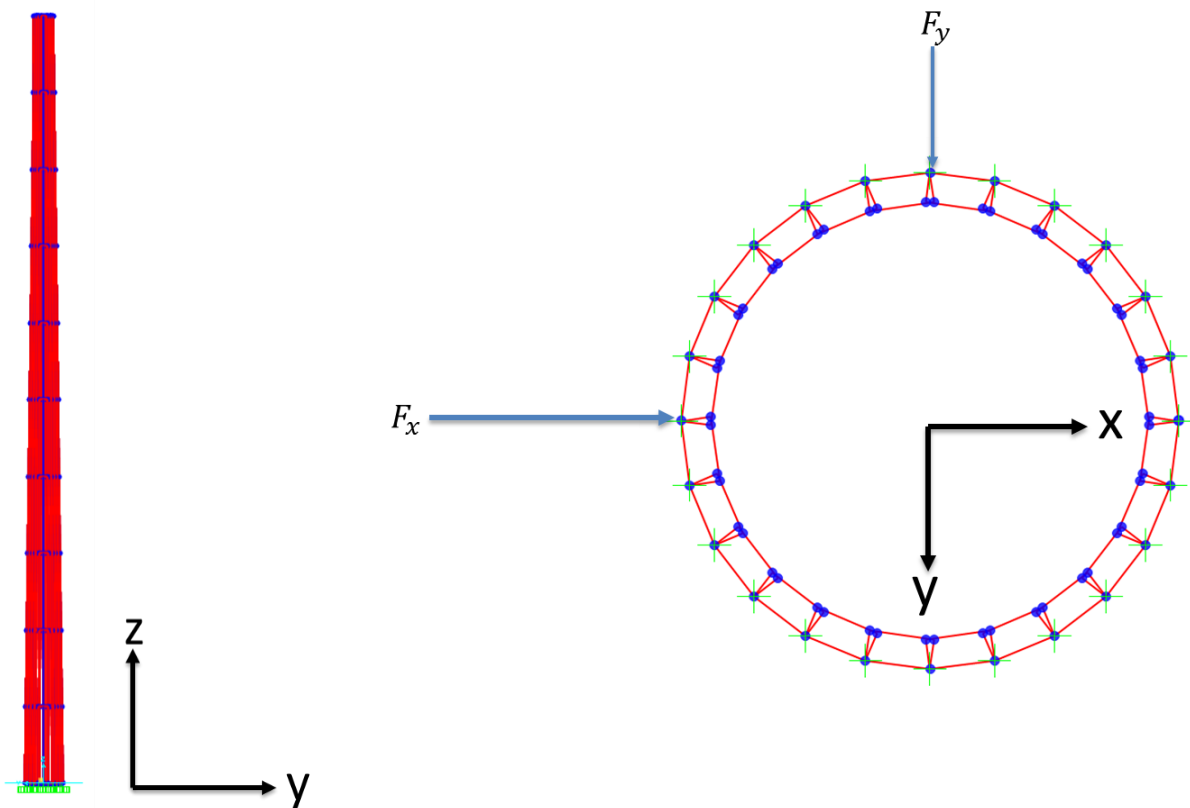
Figure 4.1 (a): FE model of the chimney.

Figure 4.1 (b): Top view of the FE model with along-wind and across-wind loading.

Modal analysis is performed to acquire the first four mode shapes and natural frequencies in both along-wind and across-wind directions, as shown in figures 4.2 and 4.3, respectively. The natural frequencies in the along-wind direction are nearly identical compared to the across-wind direction due to the symmetricity of the chimney.

Mode 1
f = 0.36 Hz

Mode 2
f = 1.64 Hz

Mode 3
f = 4.16 Hz

Mode 4
f = 7.76 Hz
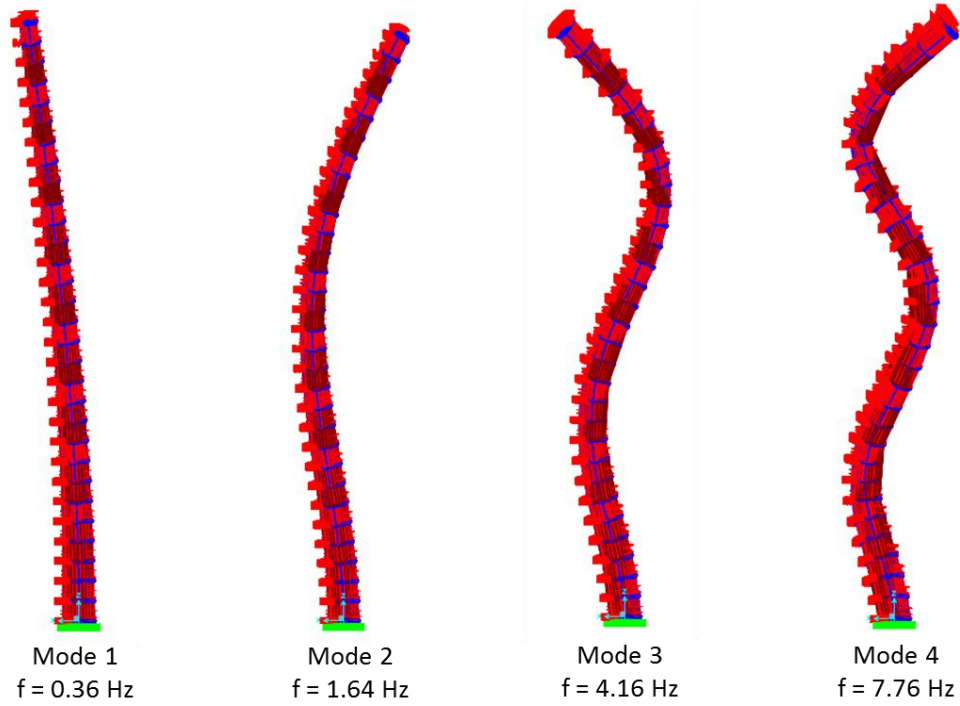
Figure 4.2: First four mode shapes and natural frequencies in along-wind direction.

Mode 1
f = 0.36 Hz

Mode 2
f = 1.67 Hz

Mode 3
f = 4.18 Hz

Mode 4
f = 7.78 Hz
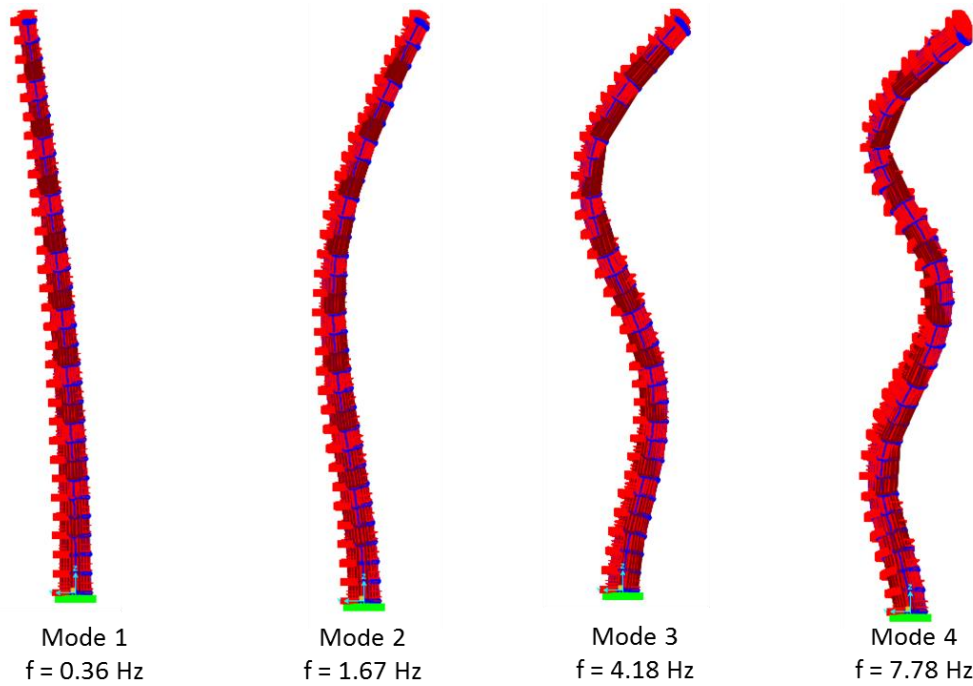
Figure 4.3: First four mode shapes and natural frequencies in across-wind direction.

4.2   Estimation of Structural Damping from the Free Vibration

To determine the structural damping ratio of the first four modes of the chimney, an impulse load is applied at the top of the model. A time-series with a load of 250 kN is applied at the top of the chimney for a small duration/ Once the free vibration is extracted from the chimney model, the acceleration responses are analyzed using SOBI to acquire the modal responses. The acceleration response and Fourier spectra of the free vibration are shown for the bottom, middle, and top floors in figure 4.4.
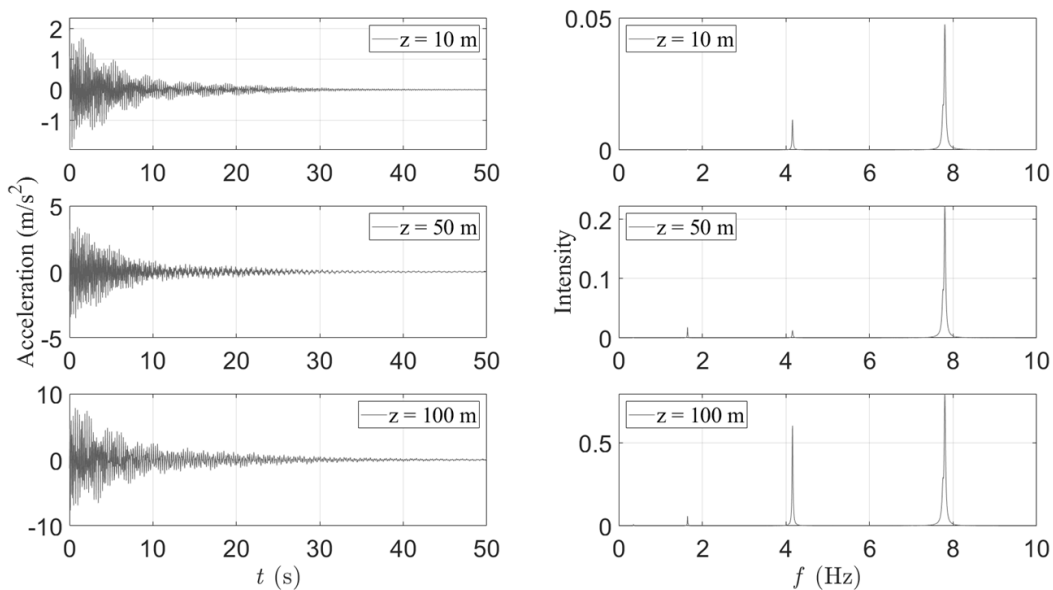
Figure 4.4:   Acceleration response and Fourier spectra of free vibration of chimney model at 10, 50, and 100 m.

The modal response of free vibration is shown in figure 4.5.
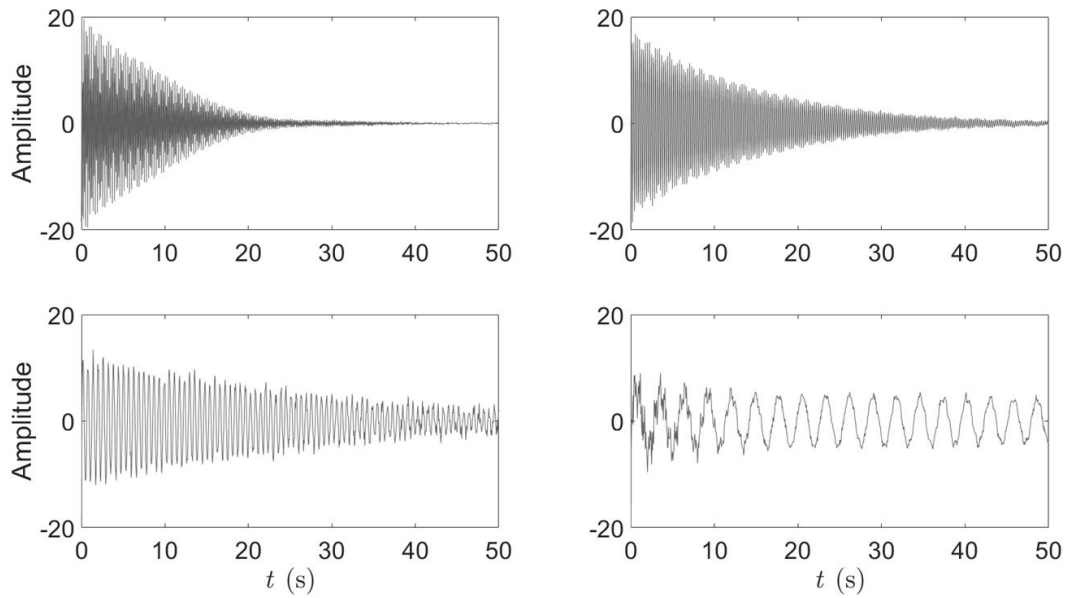
Figure 4.5: Modal response of the free vibration.

The Fourier spectra of the free vibration modal response are shown in figure 4.6.
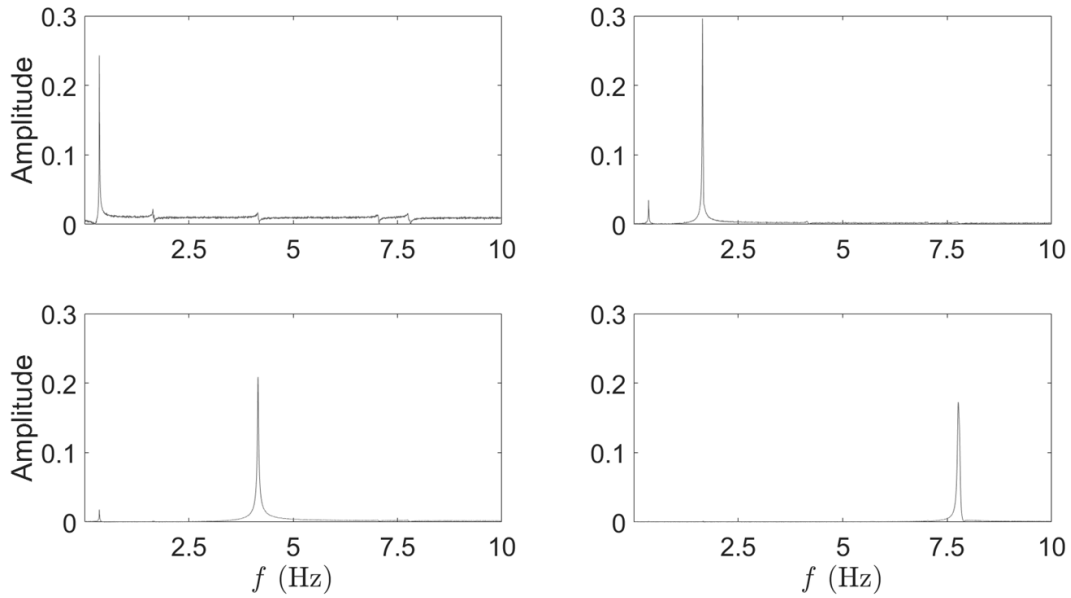
Figure 4.6: Fourier spectra of free vibration modal responses.

The autocorrelation function is applied to the modal responses, and the estimated structural damping ratios (ζ_S) are shown in Table 4.2.

Table 4.2: Structural damping ratios of the first four modes of the FE model.

Mode #	ζ_S (%)
1	2.3
2	3.7
3	8.2
4	15.0

4.3 Wind-induced Acceleration Response

The acceleration response of the chimney is acquired using forced vibration induced by the simulated wind forces, as seen in figures 3.5 and 3.6 in chapter 3. The wind force is applied in both along-wind and across-wind directions, shown in figure 4.1 (b), at ten different heights using the power-law profile and von Karman spectrum. The acceleration response from the WF and CFD simulations at z = 10, 50, and 100 m for a wind speed of $\overline{U}$ = 30 m/s are shown in figures 4.7 and 4.8.
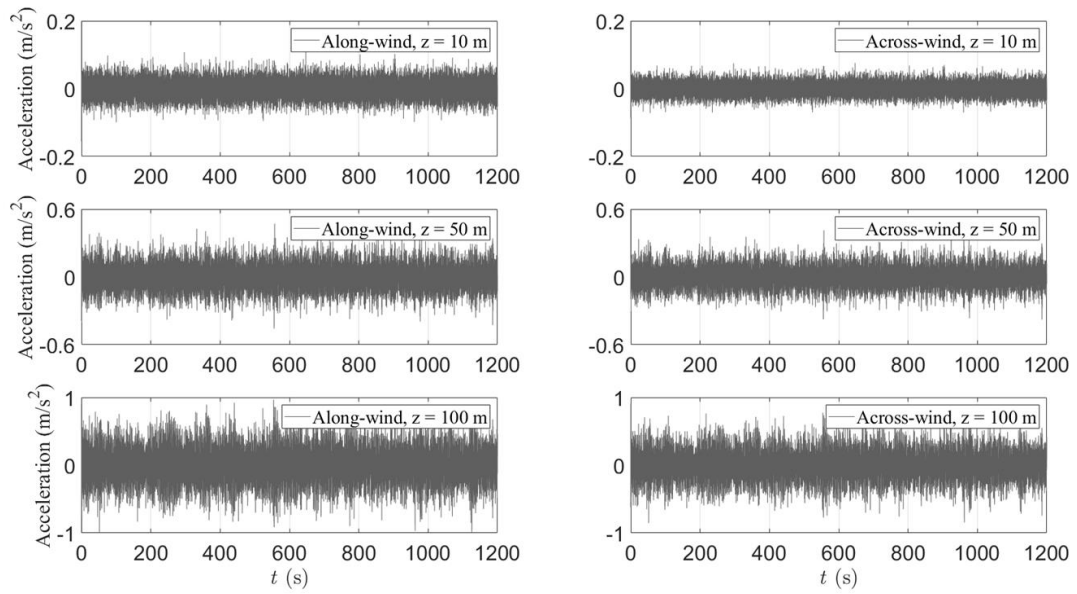
Figure 4.7: Acceleration response from the WF simulation at z = 10, 50, and 100 m for a wind speed of $\overline{U}$ = 30 m/s.
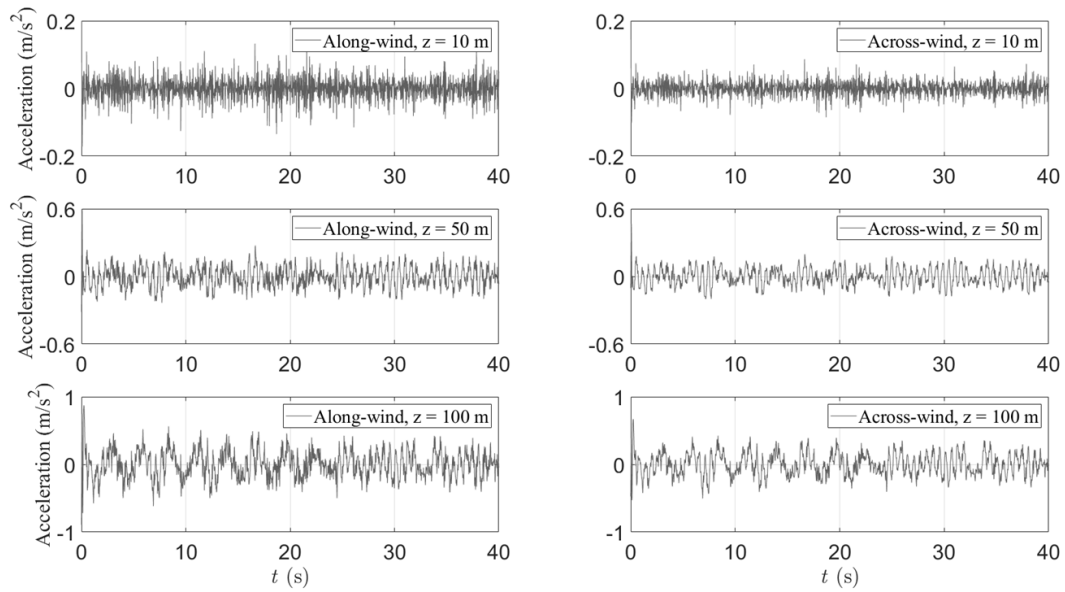
Figure 4.8: Acceleration response from the CFD simulation at z = 10, 50, and 100 m for a wind speed of $\overline{U}$ = 30 m/s.

The highest intensity of the acceleration response is expected in the first mode. The Fourier spectra of the response can be determined at any level of the chimney, although the primary area of concern is at the top. The Fourier spectra of the acceleration response in the along-wind and across-wind directions at the top of the chimney for the WF simulation are shown in figures 4.9 and 4.10, respectively. Figures 4.11 and 4.12 show the Fourier spectra of the acceleration response in the along-wind and across-wind directions at the top of the chimney for the CFD simulation.
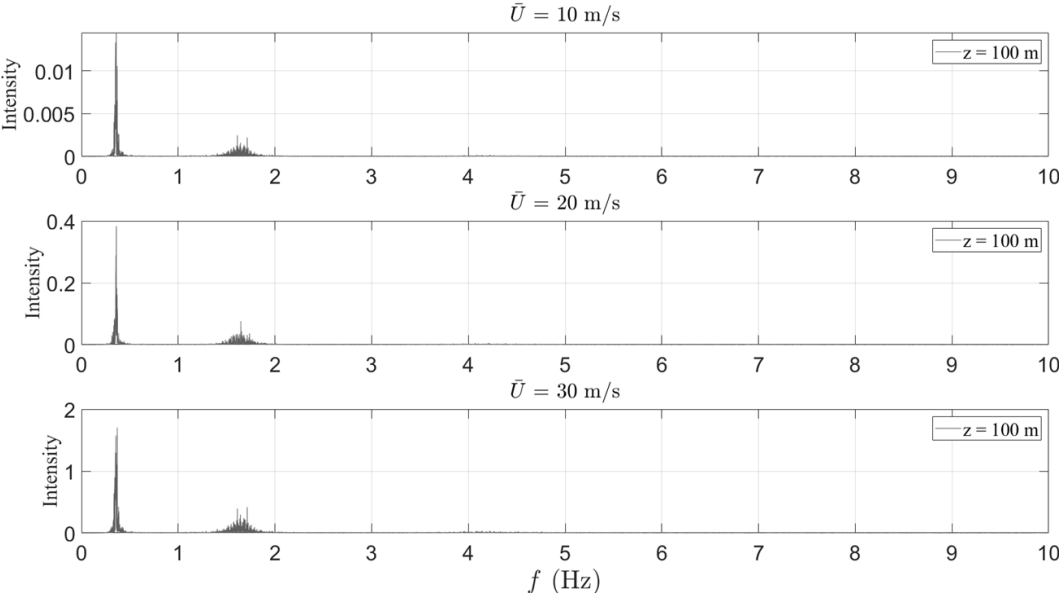
Figure 4.9: Fourier spectra of the acceleration response caused by the WF simulated excitation in along-wind direction under different wind velocities.
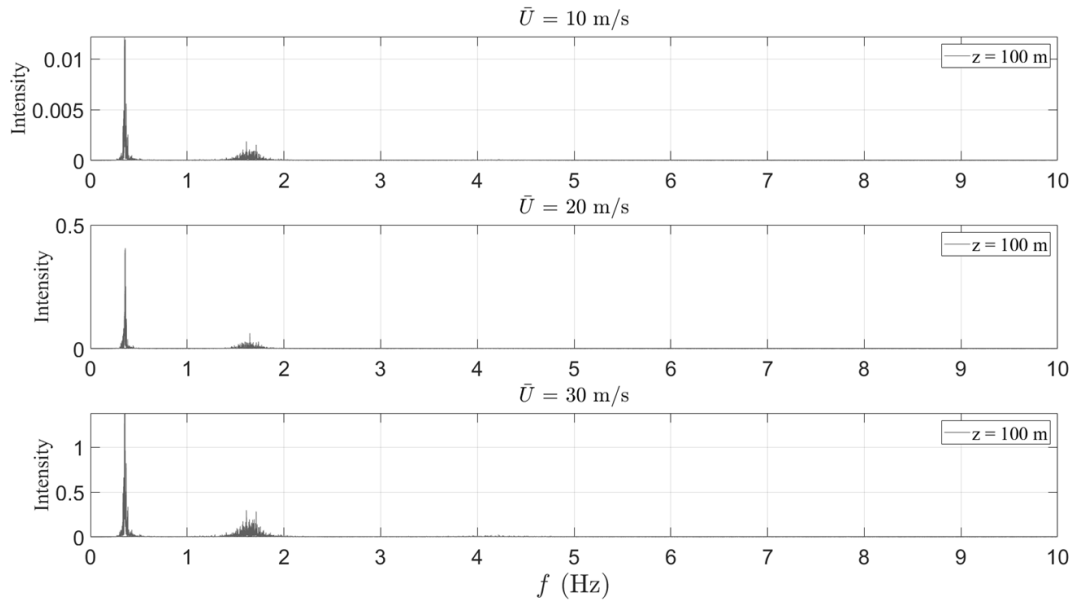
Figure 4.10: Fourier spectra of the acceleration response caused by WF simulated excitation in across-wind direction under different wind velocities.
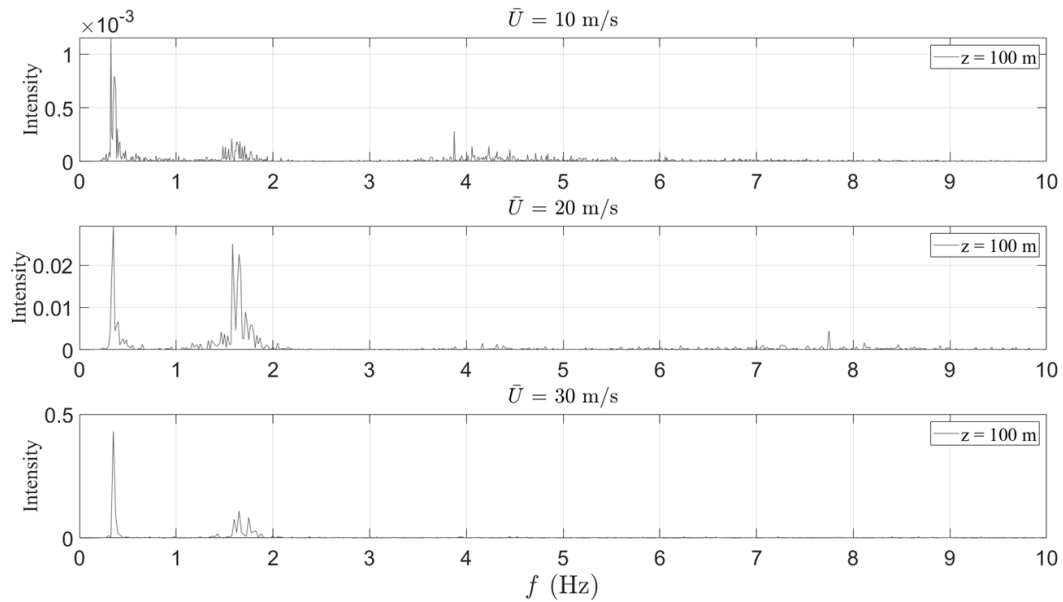
Figure 4.11: Fourier spectra of the acceleration response caused by CFD simulated excitation in along-wind direction under different wind velocities.
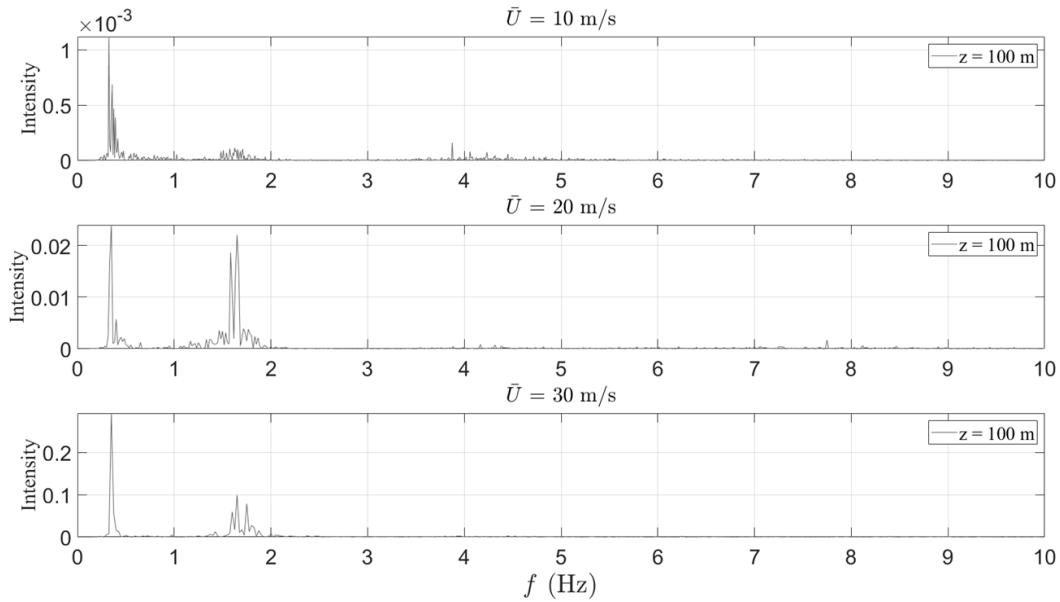
Figure 4.12: Fourier spectra of the acceleration response caused by CFD simulated excitation in across-wind direction under different wind velocities.

Each of the Fourier spectra figures of the acceleration response clearly shows the natural frequencies of the first four modes. Each of the Fourier spectra figures indicates that the first mode dominates in terms of intensity, with the second mode showing moderate intensity, and the third and fourth modes displaying minimal intensity. This agrees well with the modal damping parameters that are set within SAP2000, as the higher modes are heavily damped. These responses are then fed into the SOBI method to estimate the total and aerodynamic modal damping of the FE model, shown in the next chapter.

4.4 References

Hernandez E. M., Bernal D., and Caracoglia, L. (2012). "On-line monitoring of wind-induced stresses and fatigue damage in instrumented structures". *Structural Control and Health Monitoring*, 20, 1291-1302

78

Kareem, A. and Gurley, K. (1996) "Damping in structures: its evaluation and treatment of uncertainty". *Journal of Wind Engineering and Industrial Aerodynamics*, 59, 131-157

5 System Identification using SOBI

SOBI method is applied to the simulated acceleration response of the chimney from both WF and CFD simulations as shown in Chapter 4. First, SOBI calculates the modal responses and successfully separates them from any unwanted noise. Second, autocorrelation is applied to the modal responses to determine the total damping ratio. By subtracting the structural damping from the total damping, the aerodynamic damping ratio is estimated. It is observed that in all wind speeds and all modes, the aerodynamic damping in the across-wind direction is always less than its along-wind direction counterpart. Both along-wind and across-wind directions sometimes demonstrate negative aerodynamic damping.

5.1   System Identification of WF Simulated Response

Since the FE model of the chimney has ten degrees-of-freedom, there are ten acceleration response time histories from the forced vibration induced by the WF simulation shown in chapter 4. These raw time histories are then processed using the SOBI algorithm that produces ten modal responses. The same process is used for the acceleration responses acquired by using the CFD simulation, as shown in Section 5.2.

5.1.1   Along-wind Responses

The SOBI method is first applied to the WF simulated along-wind acceleration responses, followed by the autocorrelation of the resulting modal responses. The first four modes are shown in figure 5.1 using $\overline{U} = 10$ m/s, showing that the higher modes are heavily damped and have a low response. SOBI results are also shown for $\overline{U} = 20$ m/s and $\overline{U} = 30$ m/s in figures 5.2 and 5.3, respectively.
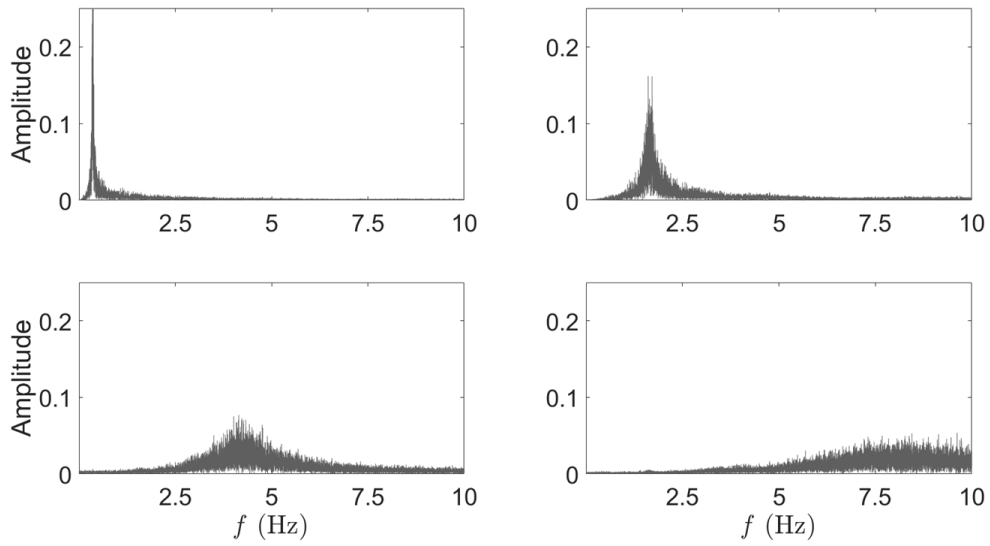
Figure 5.1: **The Fourier spectra of modal responses obtained from WF-simulated along-wind responses ($\overline{U}$ = 10 m/s).**
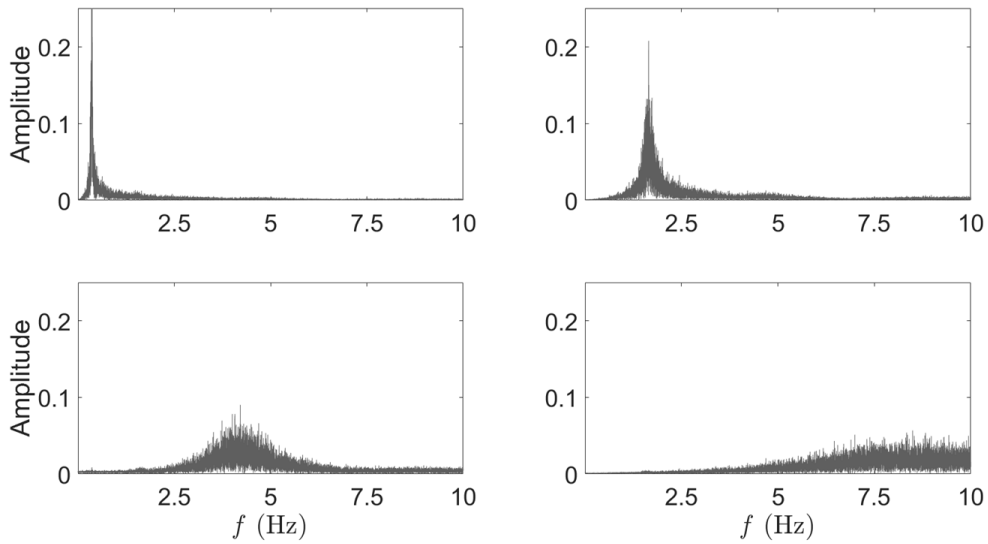
Figure 5.2: **The Fourier spectra of modal responses obtained from WF-simulated along-wind responses ($\overline{U}$ = 20 m/s).**
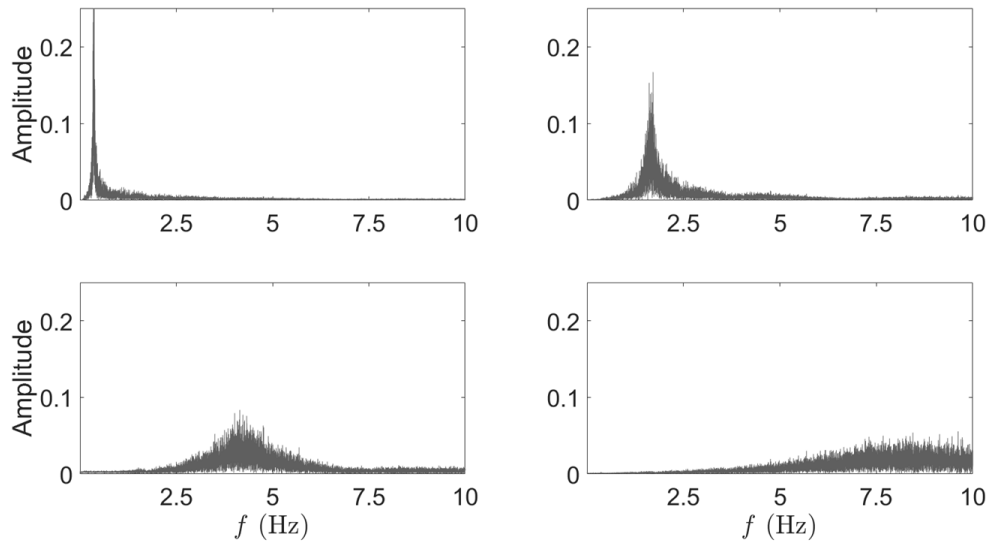
Figure 5.3: The Fourier spectra of modal responses obtained from WF-simulated along-wind responses ($\bar{U}$ = 30 m/s).

5.1.2 Across-wind Responses

In this section, all across-wind responses are analyzed using SOBI and the resulting Fourier spectra of the modal responses of the first four modes are shown in figures 5.4, 5.5 and 5.6 using different wind speeds, respectively.
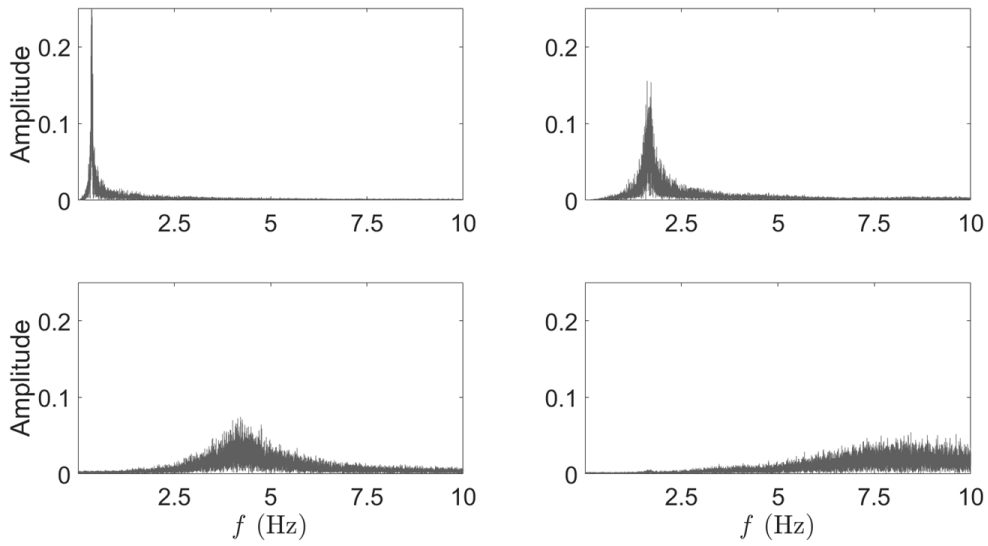
Figure 5.4: **The Fourier spectra of modal responses obtained from WF-simulated across-wind responses ($\overline{U} = 10$ m/s).**
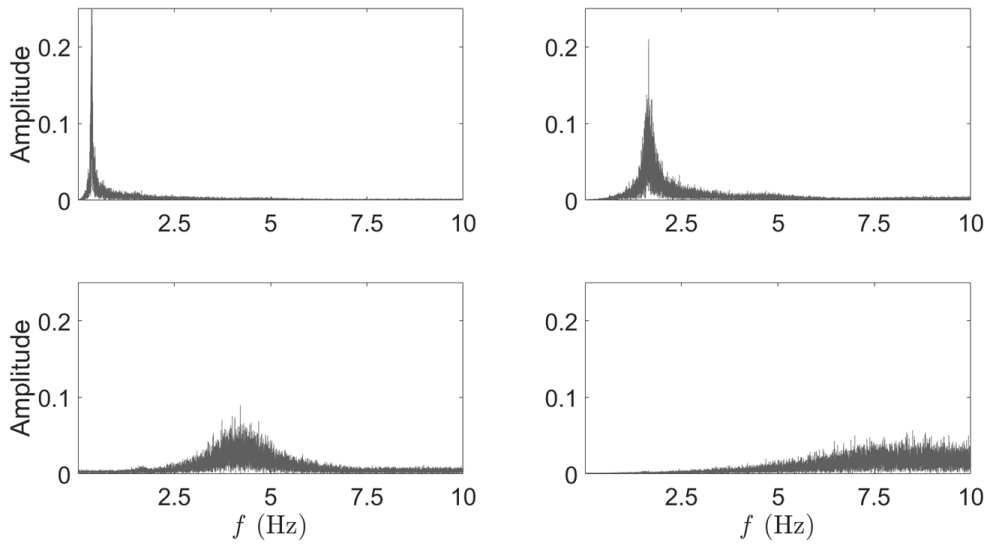
Figure 5.5: **The Fourier spectra of modal responses obtained from WF-simulated across-wind responses ($\overline{U} = 20$ m/s).**
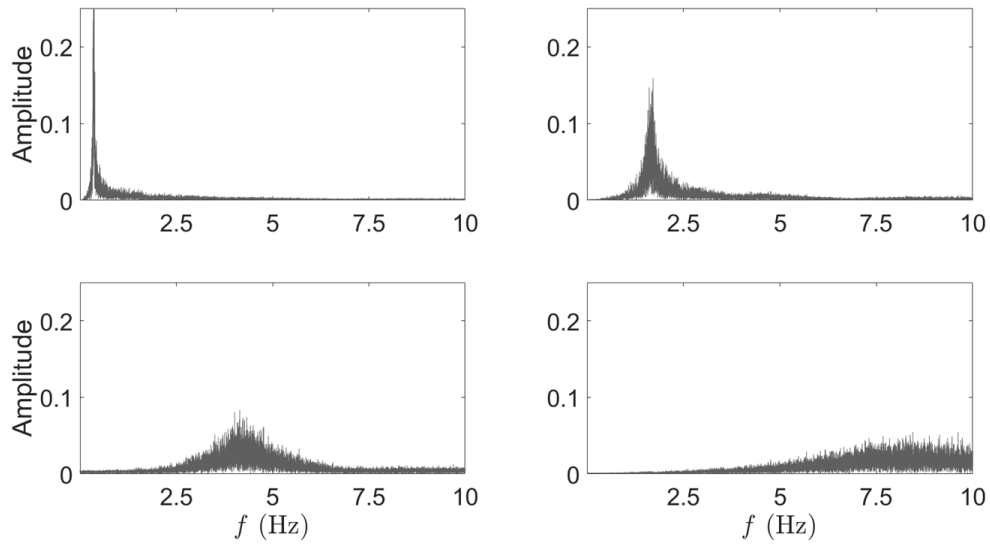
Figure 5.6: The Fourier spectra of modal responses obtained from WF-simulated across-wind responses ($\overline{U}$ = 30 m/s).

5.2   System Identification of CFD Simulated Responses

5.2.1   Along-wind Responses

The SOBI method is then applied to the CFD along-wind acceleration response. The response from the CFD simulation is much noisier compared to the wind field simulation; therefore, it is critical to use higher covariance matrices to ensure separation of the frequencies. The CFD along-wind SOBI results are shown in figures 5.7, 5.8, and 5.9.
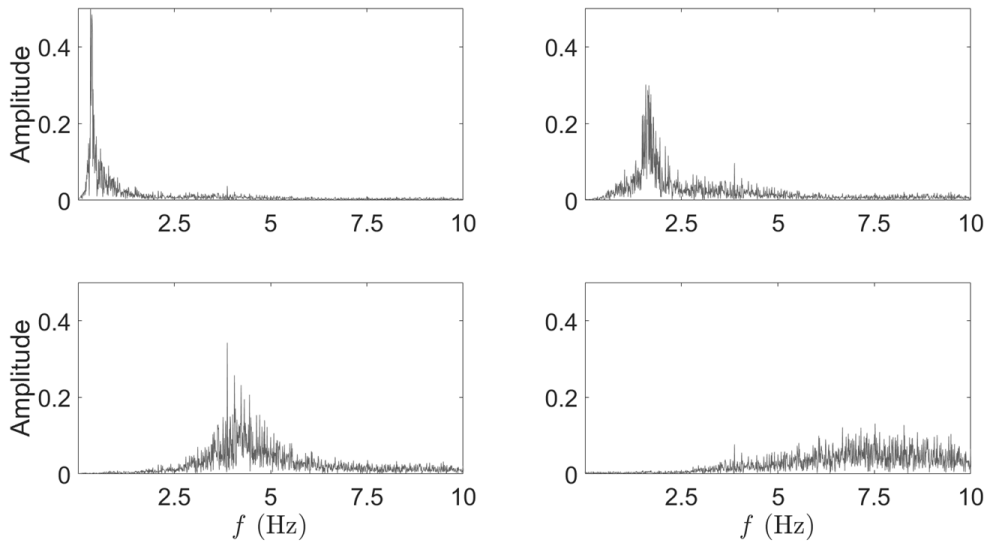
Figure 5.7: The Fourier spectra of modal responses obtained from CFD-simulated along-wind responses ($\bar{U}$ = 10 m/s).
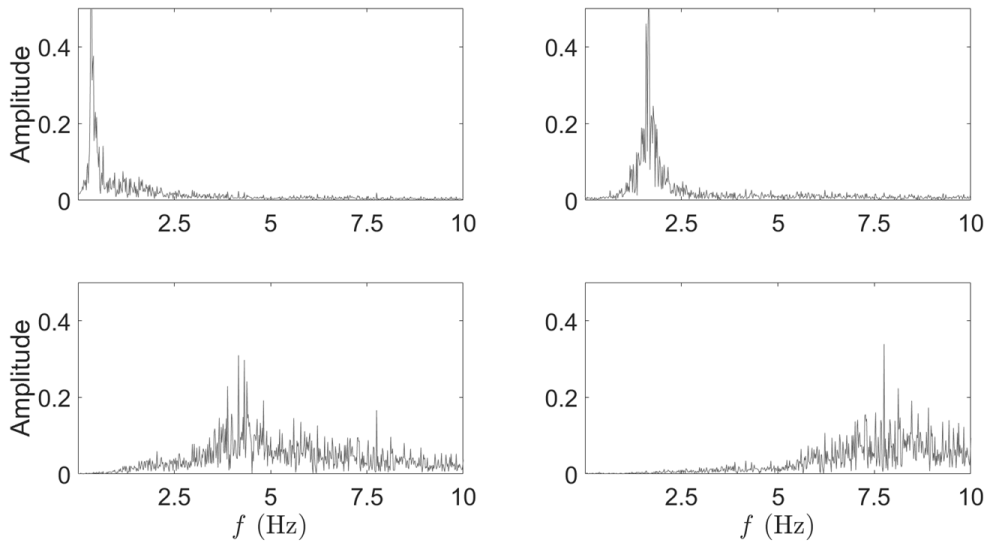
Figure 5.8: The Fourier spectra of modal responses obtained from CFD-simulated along-wind responses ($\bar{U}$ = 20 m/s).
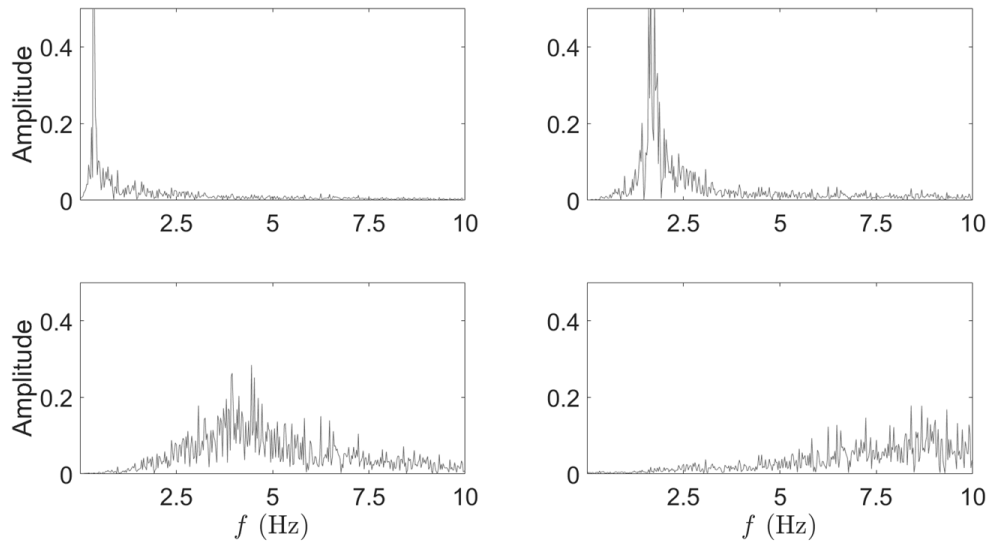
Figure 5.9: The Fourier spectra of modal responses obtained from CFD-simulated along-wind responses ($\bar{U}$ = 30 m/s).

5.2.2   Across-wind Responses

SOBI is now applied to the CFD across-wind acceleration response and the resulting modal responses are shown in figures 5.10, 5.11, and 5.12.
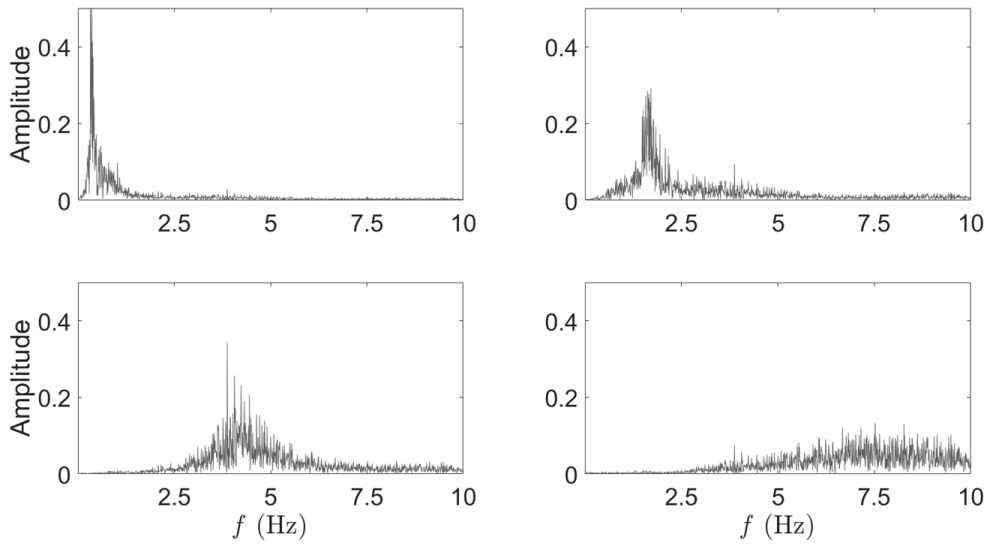
Figure 5.10: **The Fourier spectra of modal responses obtained from CFD-simulated across-wind responses ($\overline{U}$ = 10 m/s).**
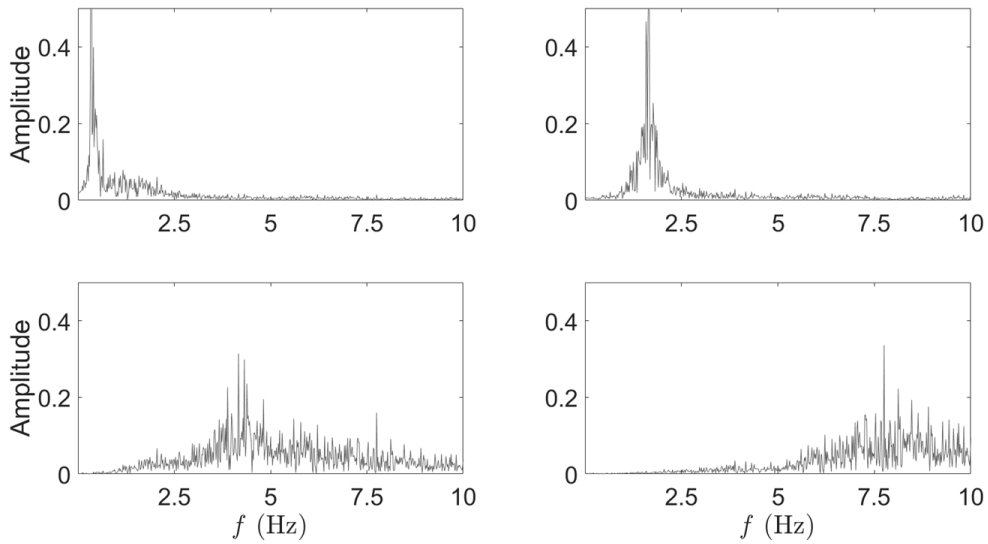
Figure 5.11: **The Fourier spectra of modal responses obtained from CFD-simulated across-wind responses ($\overline{U}$ = 20 m/s).**
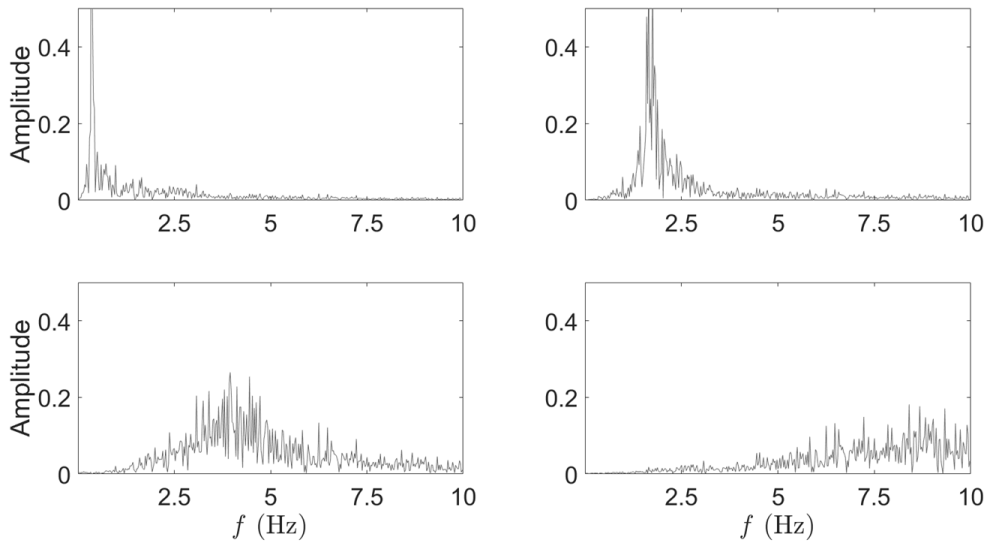
Figure 5.12: **The Fourier spectra of modal responses obtained from CFD-simulated across-wind responses ($\bar{U}$ = 30 m/s).**

5.3 Aerodynamic Damping Estimation

The modal responses are used to find the total damping ratio for the first four modes in both the along-wind and across-wind directions. Autocorrelation is used on the modal responses and a curve is fit onto the decaying function to estimate the damping. The fitted curve is in the form of the following function:

$$y(t) = Ae^{-\zeta_T \omega_d t} \tag{5.1}$$

Where A is the amplitude, ζ_T is the total damping ratio, ω_d is the damped natural frequency in rad/s, and t is time in seconds. Figures 5.13, 5.14, 5.15, and 5.16 show the autocorrelation of modal responses of the first four modes obtained using a mean wind speed of 20 m/s. Each subplot shows the fitted curve on the autocorrelation function.
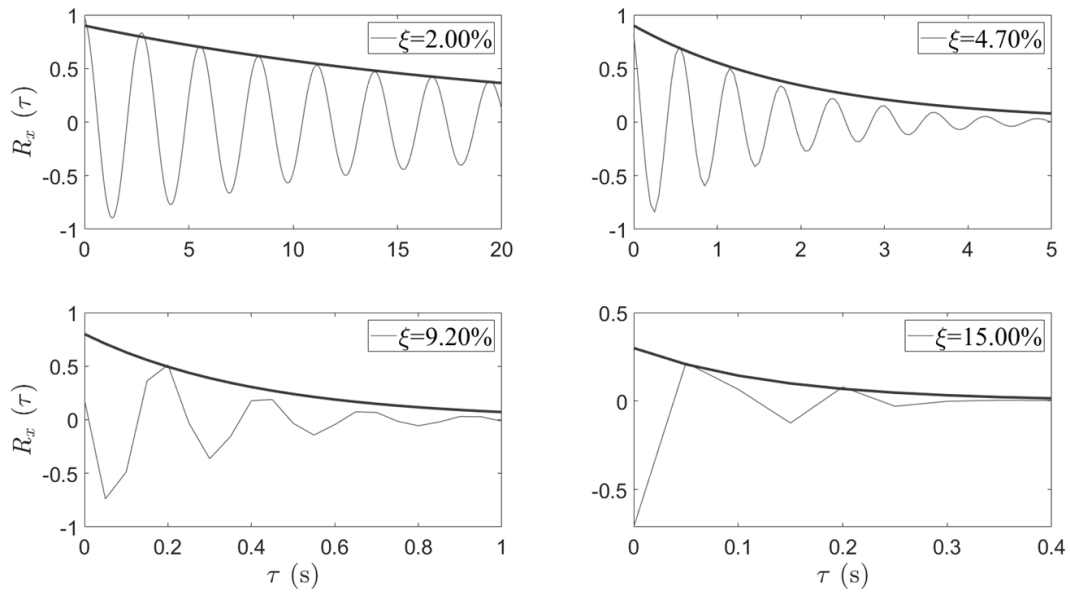
Figure 5.13: $R_x(\tau)$ of the modal responses obtained from WF-simulated along-wind response $(\bar{U} = 20$ m/s$)$.
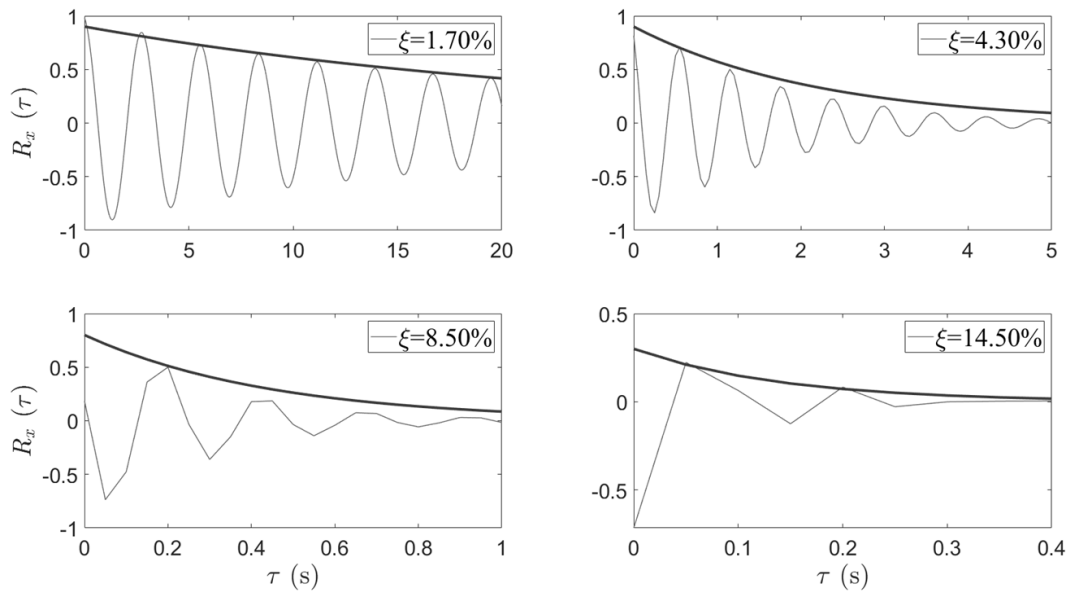
Figure 5.14: $R_x(\tau)$ of the modal responses obtained from WF-simulated across-wind response $(\bar{U} = 20$ m/s$)$.
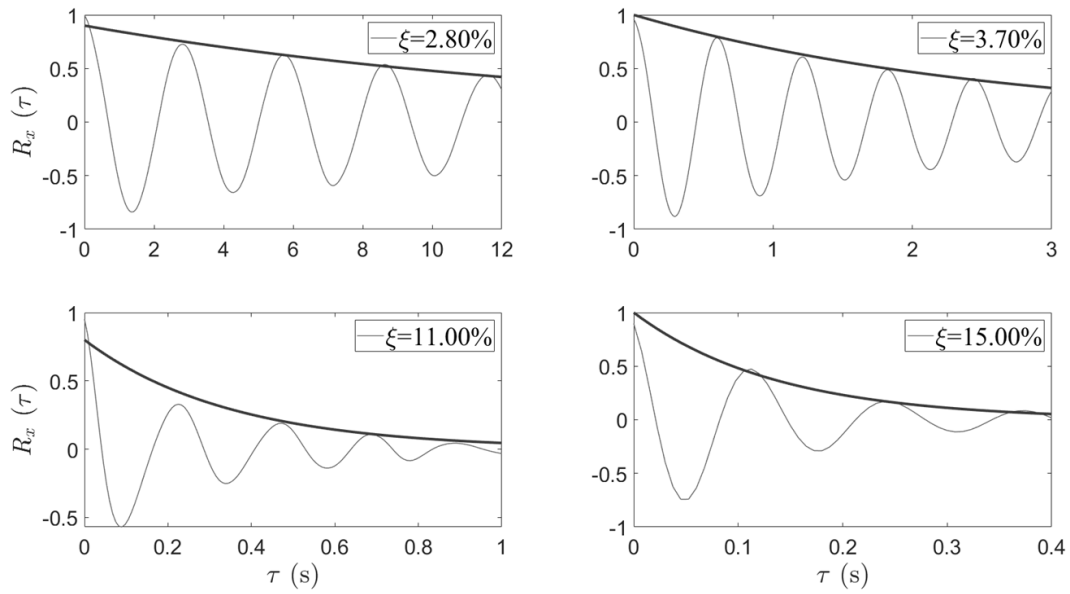
Figure 5.15: $R_x(\tau)$ of the modal responses obtained from CFD-simulated along-wind response ($\bar{U}$ = 20 m/s).
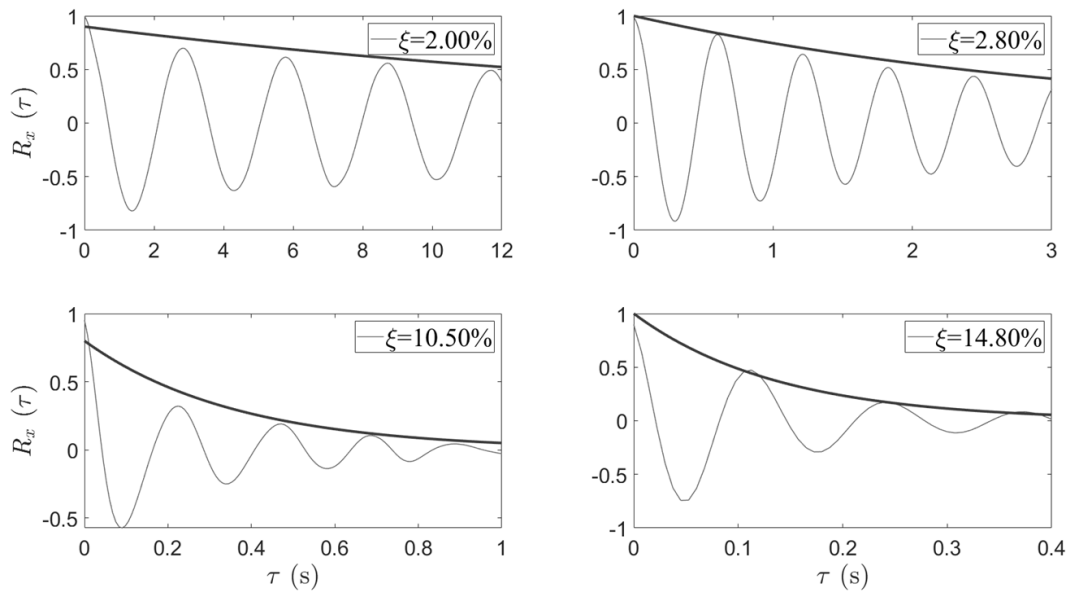
Figure 5.16: $R_x(\tau)$ of the modal responses obtained from CFD-simulated across-wind response ($\bar{U}$ = 20 m/s).

Using the total damping estimates, the structural damping ratios are subtracted from the total to estimate the aerodynamic damping ratio. Tables 5.1, 5.2, 5.3, and 5.4 show a list of all the estimated damping ratios, where ζ_T, ζ_S, and ζ_A are the total, structural, and aerodynamic damping ratios, respectively.

Table 5.1: Estimated damping ratios of the WF simulated response in the along-wind direction.

$\bar{U} = 10$ m/s				
Mode #	f (Hz)	ζ_T (%)	ζ_S (%)	ζ_A (%)
1	0.36	2.0	2.3	-0.3
2	1.64	4.5	3.7	0.8
3	4.16	8.6	8.2	0.4
4	7.76	15.1	15.0	0.1
$\bar{U} = 20$ m/s				
Mode #	f (Hz)	ζ_T (%)	ζ_S (%)	ζ_A (%)
1	0.36	2.0	2.3	-0.3
2	1.64	4.7	3.7	1.0
3	4.16	9.2	8.2	1.0
4	7.76	15.0	15.0	0

$\bar{U} = 30$ m/s				
Mode #	f (Hz)	ζ_T (%)	ζ_S (%)	ζ_A (%)
1	0.36	2.3	2.3	0
2	1.64	4.8	3.7	1.1
3	4.16	9.2	8.2	1.0
4	7.76	15.2	15.0	0.2

Table 5.2: Estimated damping ratios of the WF simulated response in across-wind direction.

$\bar{U} = 10$ m/s				
Mode #	f (Hz)	ζ_T (%)	ζ_S (%)	ζ_A (%)
1	0.36	1.7	2.3	-0.6
2	1.64	4.2	3.7	0.5
3	4.16	8.2	8.2	0
4	7.76	14.5	15.0	-0.5
$\bar{U} = 20$ m/s				

Mode	f (Hz)	ζ_T (%)	ζ_S (%)	ζ_A (%)
1	0.36	1.7	2.3	-0.6
2	1.64	4.3	3.7	0.6
3	4.16	8.3	8.2	0.1
4	7.76	14.5	15.0	-0.5
$\bar{U} = 30$ m/s				
Mode	f (Hz)	ζ_T (%)	ζ_S (%)	ζ_A (%)
1	0.36	1.8	2.3	-0.5
2	1.64	4.5	3.7	0.8
3	4.16	8.2	8.2	0
4	7.76	14.3	15.0	-0.7

Table 5.3: Estimated damping ratios of the CFD simulated response in the along-wind direction.

$\bar{U} = 10$ m/s				
Mode #	f (Hz)	ζ_T (%)	ζ_S (%)	ζ_A (%)

1	0.36	4.5	2.3	2.2
2	1.64	5.9	3.7	2.2
3	4.16	8.5	8.2	0.3
4	7.76	16.2	15.0	1.2

$$\bar{U} = 20 \text{ m/s}$$

Mode #	f (Hz)	ζ_T (%)	ζ_S (%)	ζ_A (%)
1	0.36	2.8	2.3	0.5
2	1.64	3.7	3.7	0
3	4.16	11.0	8.2	2.8
4	7.76	15.0	15.0	0

$$\bar{U} = 30 \text{ m/s}$$

Mode #	f (Hz)	ζ_T (%)	ζ_S (%)	ζ_A (%)
1	0.36	2.5	2.3	0.2
2	1.64	4.5	3.7	0.8
3	4.16	11.0	8.2	2.8
4	7.76	17.5	15.0	2.5

Table 5.4: Estimated damping ratios of the CFD simulated response in the across-wind direction.

		$\bar{U} = 10$ m/s		
Mode #	f (Hz)	ζ_T (%)	ζ_S (%)	ζ_A (%)
1	0.36	4.5	2.3	2.2
2	1.64	5.2	3.7	1.5
3	4.16	8.2	8.2	0
4	7.76	16.0	15.0	1.0
		$\bar{U} = 20$ m/s		
Mode #	f (Hz)	ζ_T (%)	ζ_S (%)	ζ_A (%)
1	0.36	2.0	2.3	-0.3
2	1.64	2.8	3.7	-0.9
3	4.16	10.5	8.2	2.3
4	7.76	14.5	15.0	-0.5
		$\bar{U} = 30$ m/s		
Mode #	f (Hz)	ζ_T (%)	ζ_S (%)	ζ_A (%)

1	0.36	2.5	2.3	0.2
2	1.64	4.4	3.7	0.7
3	4.16	10.5	8.2	2.3
4	7.76	17.0	15.0	2.0

The most noticeable observation from the damping estimates is that the across-wind aerodynamic damping is never larger than its along-wind counterpart, which agrees well with Kim *et al.* (2018), Giappino *et al.* (2015), Marukawa *et al.* (1996), and Huang *et al.* (2013). While the damping in the along-wind direction shows two negative values in the wind field simulation, negative aerodynamic damping in the across-wind direction seems to be negative more often. Another interesting observation is that the damping estimates for the CFD model are much higher, possibly due to the additional aerodynamic actions that a CFD simulation can capture. Figures 5.17 and 5.18 show the autocorrelation functions of the wind load using $\bar{U} = 30$ m/s at z = 100 m in the along-wind direction, for both the WF and CFD simulations, respectively.
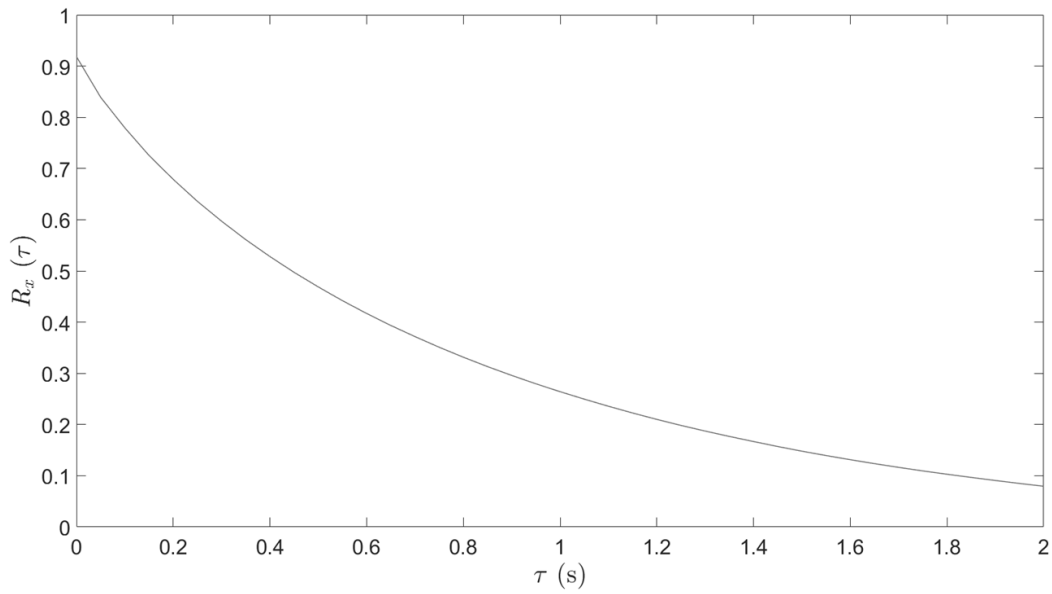
Figure 5.17: $R_x(\tau)$ of the along-wind load using $\bar{U}$ = 30 m/s at z = 100 m, WF simulation.
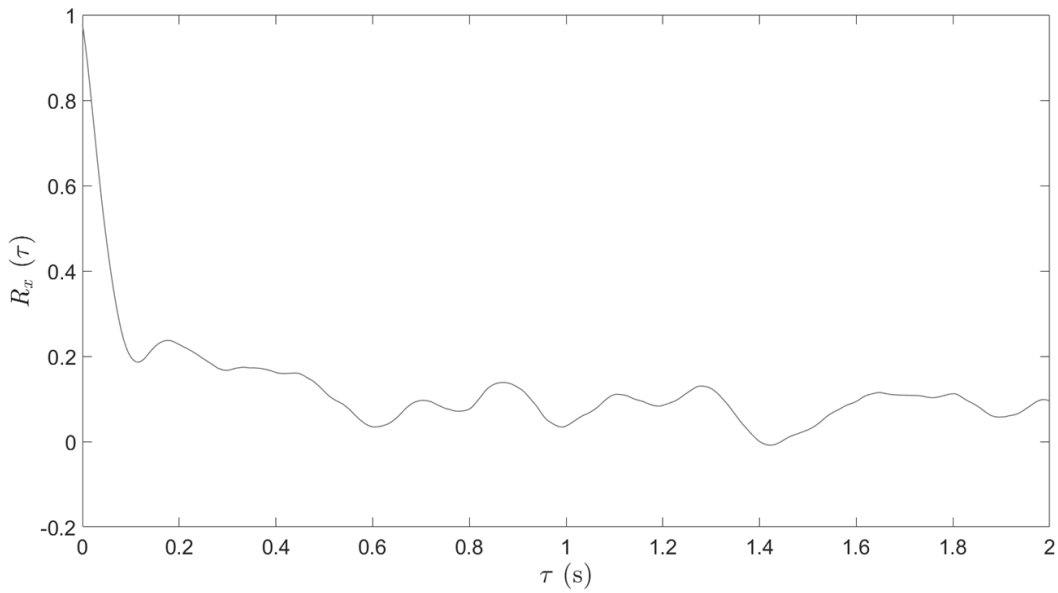
Figure 5.18: $R_x(\tau)$ of the along-wind load using $\bar{U}$ = 30 m/s at z = 100 m, CFD simulation.

The autocorrelation functions show that the wind load for the CFD simulation decays faster than that of the WF simulation. Therefore, this agrees well with the higher damping values that were

estimated for the CFD simulation case. In both WF and CFD simulation cases, the total damping estimates increase with the mode number, which agrees with the modal damping that was set for the FE model.

5.4 References

Giappino, S., Rosa, L., Tomasini, G., and Zasso, A. (2015). "An aerodynamic and aeroelastic experimental study on a sectional and three-dimensional rectangular building". *The Structural Design of Tall and Special Buildings*, 25, 139-157.

Huang, P., Quan, Y., and Gu, M. (2013) "Experimental study of aerodynamic damping of typical tall buildings". *Mathematical Problems in Engineering*, 731572, 1-9.

Kim, W., Yoshida, A., Tamura, Y., and Yi, J. (2018). "Experimental study of aerodynamic damping of a twisted supertall building". *Journal of Wind Engineering and Industrial Aerodynamics*, 176, 1-12.

Marukawa, H., Kato, N., Fujii, K., and Tamura, Y. (1996) "Experimental evaluation of aerodynamic damping of tall buildings. *Journal of Wind Engineering and Industrial Aerodynamics*, 59, 177-190.

Musafere, F., Sadhu, A., and Liu, K. (2015). "Towards damage detection using blind-source separation integrated with time-varying auto-regressive modeling". *Smart Materials and Structures*, 25, 015013.

Poncelet, F., Kerschen, G., Golinval, J. C. and Verhelst, D. (2007). "Output-only modal analysis using blind source separation techniques". *Mechanical Systems and Signal Processing,* 21, 2335-2358.

6. Conclusions and Summary

This chapter provides a summary of SOBI's ability to estimate aerodynamic damping and the key observations that were made during the research. The contributions towards the gap areas in the literature are also outlined, as are recommendations for future work related to SOBI combined with wind engineering.

6.1   Conclusions

This thesis proposes the use of the SOBI method to identify the aerodynamic damping of a FE model of a slender chimney subjected to the simulated wind forces. At first, the wind simulation uses the concepts of the power-law profile and von Karman spectrum, then uses pre-determine drag and lift coefficients to generate the wind force. The second wind simulation uses CFD modeling combined with LES to generate force coefficients along the height of the chimney which are converted into the wind force. SOBI successfully identifies the aerodynamic damping ratios using both simulations; the first four modes are considered for the damping estimates since higher modes are heavily damped and contain a very low amplitude of the response. Aerodynamic damping estimates are performed in both the along-wind and across-wind directions and the following conclusions are made:

- In either wind simulation case, the aerodynamic damping in the along-wind direction is always higher compared to the across-wind direction, which is consistent with the literature.

- Damping estimates in both directions show some negative values, although negative values are more frequent in the across-wind direction, which was also emphasized in the literature.

- Damping estimates are consistently higher when using the wind force from the CFD simulations. After autocorrelating the wind forces using pre-determined coefficients and CFD, it is found that the wind force using CFD decays faster. Therefore, it is expected that the damping estimates for the CFD are larger.

- Overall, SOBI was able to identify the aerodynamic damping in both along-wind and across-wind directions.

6.2 Contributions

In this thesis, the SOBI method is explored to estimate the aerodynamic damping of the slender structure, such as, a chimney. SOBI is selected due to its simplicity (i.e., free of stabilization diagram and model order selection) when compared to SSI, and its compatibility with MDOF systems which is an advantage over RDT. SOBI also proves to be robust when separating the modal responses and eliminating noise which is an improvement over both SSI and RDT. An important research interest was SOBI's ability to perform damping estimates on the response using CFD wind loading, which it handled adequately. The results obtained during this research indicate that SOBI shows great promise when used in conjunction with CFD modeling, as well as other wind simulation methods. Therefore, SOBI is a viable option to estimate aerodynamic parameters of dynamically sensitive structures.

6.3 Future Work

- While the acquired results are encouraging, this research is composed entirely of simulations, including both the wind fields and the chimney model. Further research will include the use of SOBI on the response of aero-elastic wind tunnel models at the Boundary Layer laboratory at Western.

- It is also anticipated to validate the aerodynamic damping estimates obtained from the wind-induced response of a real-life chimney to compare the damping estimates with the finite-element model.

- Future research should also include the implementation of SOBI with different kinds of structures. While the study of chimneys is important for industrial purposes, SOBI should be considered for wind-loaded high-rise buildings due to the vast amount being designed and monitored. Other slender structures to perform aerodynamic damping estimates include long-span bridges, antenna masts, and light poles. Damping estimates using CFD modeling and full-scale testing of these different kinds of structures should be performed.

Curriculum Vitae

Name: Shea Laventure

Post-secondary   Saskatchewan Polytechnic
Education and   Moose Jaw, Saskatchewan, Canada
Degrees: 2010-2012 Diploma – Civil Engineering Technology

Lakehead University
Thunder Bay, Ontario, Canada
2015-2017 Bachelor of Engineering – Civil

The University of Western Ontario
London, Ontario, Canada
2018-2020 Master of Engineering Science - Structural

Related Work   Teaching Assistant
Experience   Lakehead University
2017-2018

Teaching Assistant
The University of Western Ontario
2018-2019

Publications:

Sony, S., Laventure, S., and Sadhu, A. (2019). "A literature review of next-generation smart sensing technology in structural health monitoring". *Structural Control and Health Monitoring,* 26, 2321

Laventure, S., Sadhu, A., and Bitsuamlak, G. (2020). "Blind identification of aerodynamic damping using wind-induced response of slender structures". (*Under Preparation*).